1-1-2003

Prediction of sea ice concentration using artificial neural networks

Mohammed Kandil El-Emam El-Diasty
Ryerson University

Prediction of Sea Ice Concentration Using Artificial Neural Networks

By

Mohammed Kandil El-Emam El-Diasty

B.Sc.(Eng.) - Civil Engineering, Mansoura University, Egypt (1997)

A THESIS
SUBMITTED TO RYERSON UNIVERSITY
SCHOOL OF GRADUATE STUDIES
IN PARTIAL FULFILMENT OF THE REQUIREMENTS FOR
THE DEGREE OF MASTER OF APPLIED SCIENCE
IN THE PROGRAM OF
CIVIL ENGINEERING

DEPARTMENT OF CIVIL ENGINEERING,
RYERSON UNIVERSITY, TORONTO, ONTARIO.

RYERSON UNIVERSITY

September, 2003

Your file Votre référence
ISBN: 0-612-85315-2
Our file Notre référence
ISBN: 0-612-85315-2

DECLARATION

I hereby declare that I am the sole author of the thesis. I authorize Ryerson University to lend this thesis to other institutions or individuals for the purpose of scholarly research. I further authorize Ryerson University to reproduce this thesis by photocopying or by other means, in total or part, at the request of other institutions or individuals for the purpose of scholarly research.

Mohammed El-Diasty

APPROVAL

Ryerson University

School of Graduate Studies

The undersigned certify that they have read, and recommend to the School of Graduate Studies for acceptance, a thesis entitled "***Prediction of Sea Ice Concentration Using Artificial Neural Networks***" submitted by Mohammed Kandil El-Emam El-Diasty in partial fulfillment of the requirements for the degree of Master of Applied Science.

APPROVED:

Dr. Mohamed Lachemi, Committee Chair

Department of Civil Engineering

Dr. Ahmed El-Rabbany, Supervisor

Department of Civil Engineering

Dr. Said Easa, Chairman

Department of Civil Engineering

Dr. Songnian Li

Department of Civil Engineering

ABSTRACT

Prediction of Sea Ice Concentration Using Artificial Neural Networks

Mohammed Kandil E. El-Diasty
B.Sc. (Eng.) - Civil Engineering, Mansoura University, Egypt (1997)
Master of Applied Science
In the Program of Civil Engineering
Ryerson University (2003)

Artificial neural networks are computational models capable of solving complex problems through learning, or training, and then generalizing the network solution for other inputs. This thesis examines the performance of two neural network-based models, which were developed for predicting the ice concentration in the Gulf of St. Lawrence in Eastern Canada. The first is a batch model which uses time to predict future ice concentration, while the second model predicts the ice concentration sequentially. It is shown that the performance of the two models is almost identical, as long as no abrupt changes occur in the ice conditions. If, however, the ice condition changes suddenly, only the sequential model is proved to be capable of predicting the ice condition without noticeable accuracy degradation. A performance comparison is made between the developed neural network model and coupled ice-ocean model for ice concentration prediction to further validate the model.

DEDICATION

This thesis is affectionately dedicated

To my dearest MOTHER, and ALL I LOVE.

ACKNOWLEDGEMENTS

Above all, I am in debt to ALLAH who has given me the health, strength and patience to complete my work during this critical stage of my life.

First, I am greatly indebted to my advisor and chair of this project, Dr. Ahmed El-Rabbany, without him I would never have completed this work for his guidance, encouragement, and support throughout the research. I also want to thank the other committee members, Dr. Said Easa, Dr. Songnian Li, and Dr. Mohamed Lachemi, for their time in reviewing the thesis and their invaluable suggestions.

This research is supported by the Centre for Research in Earth and Space Technology (CRESTech), an Ontario Centre of Excellence. I would also like to express my appreciation to Mr. Bruce Ramsay, Mr. John Falkingham, Mr. Dean Flett, Mr. Richard Chagnon, Mr. Dan Fequent, Mr. Luc Desjardins, and Mrs. Maria MacLeod at the Canadian Ice Service in Ottawa for providing us with the ice charts used in this research.

It is a pleasure also to thank a number of very special persons, Dr. Ali Emam, Mahmoud Abd El-Gelil, Essam El-Dabbour, and Walid Hassan for their kind help both in studying and in everyday life. I would also like to thank Mr. Peter McSweeney for proofreading the thesis.

There are many who have contributed their heartfelt sympathy to my efforts. I would like to personally express my deep thanks to my mother, my sisters and my brothers for their encouragement and support in my life. Moreover, I would also like to give my special

gratitude to my wife for her devotion and support. I greatly appreciate their unconditional love and support all the time, especially during this period in my life.

Table of Contents

List of Figures

List of Tables

Abbreviations

AMI	Active Microwave Instrument
ANN	Artificial Neural Network
ASAR	Advanced Synthetic Aperture Radar
AVHRR	Advanced Very High Resolution Radiometer
CCG	Canadian Coast Guard
CCRS	Canada Centre for Remote Sensing
CDPF	Canadian Data Processing Facility
CHS	Canadian Hydrographic Service
CIS	Canadian Ice Service
CIDAS	Climatological Ice Data Archive System
CMC	Canadian Meteorological Centre
CORR	Correlation Coefficient
CSA	Canadian Space Agency
DMSP	Defence Meteorological Satellite Program
ECDIS	Electronic Chart Display and Information System
EDBD	Extended-Delta-Bar-Delta rule
ENVISAT	ENVIronmental SATellite

ERS	European Remote Sensing
ESRI	Environment Systems Research Institute
FFNN	Feedforward Neural Network
GEM/NWP	Global Environmental Multi-scale/Numerical Weather Prediction
GIS	Geographic Information System
IHO	International Hydrographic Organization
ISIS	Ice Service Integrated System
ITN	Image Transfer Network
MAST	Marine Analysis System
MLP	Multi-Layer Perceptron
MNN	Modular Neural Network
NAD 27	North American Datum 1927
NAIL	North American Ice Link
NIC	National Ice Centre
NOAA	National Oceanic and Atmospheric Administration
PIC	Particle-In-Cell
PNN	Probabilistic Neural Network

RADAR	Radio Detection And Ranging
RADARSAT	RADAR SATellite
RBF	Radial Basis Function
RMS	Root Mean Square
SAR	Synthetic Aperture Radars
SLAR	Side Looking Airborne Radar
SOM	Self-Organizing Map
SSM/I	Special Sensor Microwave Imager
WMO	World Meteorological Organization

1 INTRODUCTION

1.1 Motivation

Electronic Chart Display and Information System (ECDIS) was introduced over a decade ago to provide the mariners with the required information for efficient and safe marine navigation. Unfortunately, however, in ice-infested waters, the use of ECDIS as a standalone information system would not provide sufficient information for safe navigation. Shipborne radar may be used to detect the navigation hazards, e.g. icebergs, which could be superimposed on the ECDIS display (Randell et al., 1998). Although this process may improve the safety of navigation in open waters, it is of limited use in ice-infested waters as the coverage of the shipborne radar is limited to the radar horizon.

Safe and efficient marine navigation require that comprehensive and timely information on the ice conditions be available over a region extending well beyond the shipborne radar horizon (El-Rabbany, 2000). Validation experiments have shown that radar remote sensing, particularly RADARSAT, has the capability of providing such comprehensive information. The ScanSAR modes of RADARSAT are recommended for comprehensive monitoring of the sea ice conditions. The Canadian Ice Service (CIS) is primarily using these modes, along with other sources of information such as airborne and other satellite remote sensing, for extracting the sea ice information in the form of daily ice charts (Ramsay et al., 1998; Canadian Ice Service, 2002). The ice charts contain information such as the ice concentration and type, ice edge location, icebergs, and open leads. The

total concentration of the sea ice is the most important element of the ice information required to support vessels with no ice capability (Haykin et al., 1994). Unfortunately, although the ice charts are highly useful in providing comprehensive ice information, they may not fulfil the requirements for safe and efficient marine navigation, even if they are used side-by-side with ECDIS. For example, a route may be identified as an ice-free or a least hazardous through an ice chart, while it may not necessarily be a suitable route for marine navigation due to, e.g. shallow water depth.

El-Rabbany (2000) is carrying out a multidisciplinary, multi-university research project to enhance safety of marine navigation in ice-infested waters. The research project develops an integrated navigational chart system, which combines the sea ice information and ECDIS (Figure 1.1). It has three distinct, albeit linked, objectives: (1) to develop a neural network-based model for reliable prediction of the sea ice conditions; (2) to integrate sea ice information into ECDIS through the development of International Hydrographic Organization (IHO)-compliant ECDIS standards for the ice information (i.e., extension of S-57 and S-52 standards); and (3) to develop an integrated navigational chart system, which automatically recommends optimal navigation routes based on informed decision. Integrating the ice information into the ECDIS system has not only safety and economic impacts, but also environmental impacts, for example, through the reduction of fuel consumption. The purpose of this research is to develop the first component of the project, namely, a neural network-based model for predicting the sea ice concentration over time.

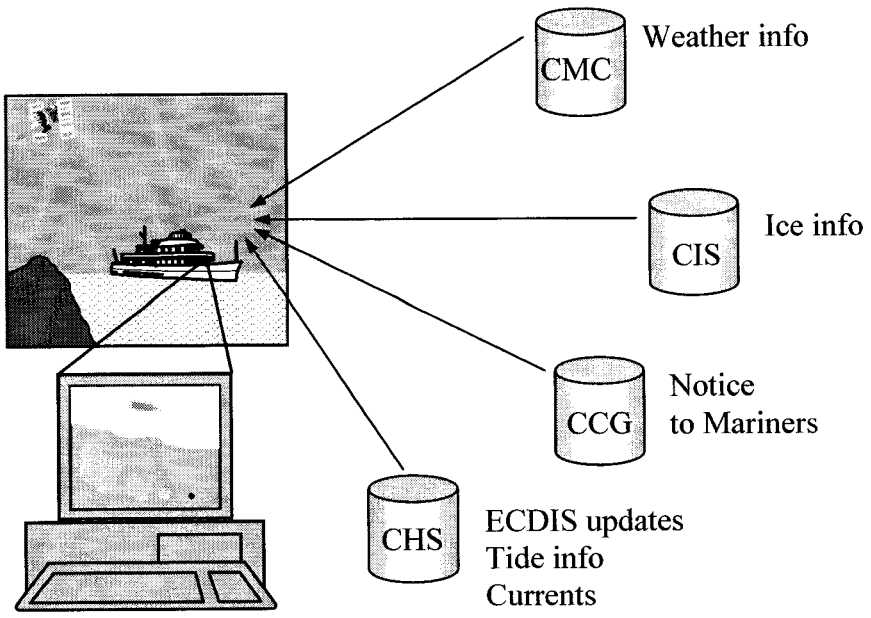

Figure 1.1 Components of Integrated Navigational Chart System (From El-Rabbany, 2000).

Unfortunately, due to the time difference between the production and the use of the ice charts, the ice information is always out of date, which jeopardizes the safety of marine operations (Canadian Ice Service, 2002). To overcome this problem, Saucier et al. (2000) developed a coupled ice-ocean prediction method, which allows the prediction of ice concentration by coupling a Flato's multi-category Particle-In-Cell ice model with a developed Backhaus's ocean model (Saucier et al., 2000). The model was developed at the Institute Maurice Lamontagne where it is also used for climate studies. However, this model is still being investigated and implemented at Canadian Ice Services.

To overcome the above limitations efficiently, an Artificial Neural Network (ANN)-based model was developed for predicting the sea ice co

nditions (concentrations) over time. Two neural network-based models were developed for predicting the ice concentration in the Gulf of St. Lawrence, using the CIS's weekly ice charts. The first is a batch model that uses past ice information to predict future ice conditions, and the second model predicts the ice conditions sequentially. The motivation behind the selection of ANNs lies in their robustness in modeling and their ability to model highly non-linear functions and achieve mapping through supervised learning by example (El-Rabbany et al., 2002). Moreover, ANN does not need such specific complex equations as are embedded in the coupled ice-ocean model; instead, it needs sufficient input-output data. Also, it can continuously re-train the new data; therefore, it can conveniently adapt to new data.

1.2 Previous Studies

Progress has been made in the evolution of completely coupled ice-ocean numerical models. At first, decoupled models were the general rule. There are many more modeling studies that have explicitly modeled ice and described oceanic parameters. Maykut and Understrein (1971) developed a one-dimensional thermodynamic ice model which was simplified by Semtner (1976a) and shown to perform well even if the ice was presented by a low-resolution vertical grid. Parkinson and Washington (1979) used Semtner's model and the simplified ice dynamic model to simulate the yearly ice cycle. Hibler (1979) developed a horizontal two-dimensional transport model which exhibited realistic

properties, based on the viscous-plastic rheology. Moreover, he used ice growth rates, which were prescribed as a function of ice thickness and time of year; such a formulation is, of course, limited to specific geography and excludes processes such as oceanic feedback.

Hibler and Bryan (1984) and Semtner (1987) presented the next step in model evolution with their coupled ice-ocean models, using seasonal forcing. Hibler and Bryan (1984) coupled a fully dynamic-thermodynamic ice model with the Bryan-Cox 14 level ocean model. Semtner's model was similarly a multi-level ocean model coupled to an ice model, with a few important differences. The model simplified the ice dynamics by using bulk viscosity as the only internal sink for ice energy, a three-level thermodynamic model of snow-covered ice (Semtner 1976b), a long-term monthly mean, atmospheric forcing fields, and most important, removed the relaxation of oceanic temperature and salinity values to climatology.

Hakinnen and Mellor (1992) adapted the Princeton Ocean Model (POM) to the Arctic and North Atlantic Oceans in the form of a 20 sigma level, an approximately 8/10 degree resolution model. Recent use of their sigma coordinate model is reported by Mauritzen and Hakinnen (1997), where they present a reasonably realistic representation of large-scale features. Yao et al. (2000) coupled a multi-category, variable thickness sea ice model to a 16-sigma level, $1/6^{o}$ version of POM for their study of sea ice in the Labrador Sea, currently used in Canadian Ice Service for East Coast Zone.

Gulf of St. Lawrence sea ice has been the subject of a number of studies with numerical models by Institute Maurice Lamontagne (IML). Recently, Saucier et al. (2000) coupled Flato's McPIC (multi-category particle-in-ice-cell model) ice model with a derivative of Backhaus's ocean model. However, these models require a realistic description of the initial ice and ocean conditions in order to achieve acceptable accuracy. Such traditional prediction models have been developed with a fixed equation form based on limited number of data and parameters. If new data is much different from original data, then the model should update not only its coefficients but also its equation form.

Later, neural networks were first applied to predict the ice conditions by using the weekly ice charts data of the Gulf of St. Lawrence (El-Rabbany et al., 2002). However, their model, which is feedforward neural network in the batch mode, is applicable only for predicting one point, and without abrupt changes within the data over the time. In fact, abrupt changes are more likely to occur in the field data. Thus, a more advanced ANN model for modeling ice conditions is needed.

1.3 Methodology

As mentioned above, two neural network-based models were developed for predicting the ice concentration in the Gulf of St. Lawrence using the CIS's ice charts. The first is a batch model which uses past ice information to predict future ice conditions, and the second model predicts the ice conditions sequentially.

Initially, in batch model, the time, which consists of two inputs (i.e., week and year numbers), was used as the only input to the network, the process usually followed in the

literature (see, for example, El-Rabbany et al., 2002). Then, another approach was followed, proposed by El-Diasty et al. (2002), and El-Rabbany and El-Diasty (2003). In this approach, the immediate and past values of the ice concentration were used as input to the network, while future values of the ice concentration were used as the desired (i.e., actual) output. In the subsequent epochs, the training patterns were shifted ahead by one value.

One method of determining the modeling power of the developed artificial neural networks is to compare the prediction capabilities of ANN with some other established prediction tool. Since Canadian Ice Service uses coupled ice-ocean model in predicting the ice conditions, this research compares the prediction abilities of the developed ANN with the operational coupled ice-ocean model. This comparison involves three steps. First, appropriate datasets are obtained. Second, two neural network models are built using a commercially available software product, NeuralWorks Proffissional II/Plus, and the best model is selected. Third, the results of the best neural network model are compared with that of the coupled ice-ocean model.

1.4 Outline of the Thesis

The research was performed according to the main objectives and methodology described in the first chapter. The second chapter begins with a brief description of ice charts. Data reconnaissance from Spaceborne, Airborne, and In-situ observations are presented. Data analysis in Canadian Ice Service is then explained. An importance of these products for the clients is also given. The traditional ice condition prediction method is described in

the third chapter, extracting the main benefits and limitations of the coupled ice-ocean model application on ice conditions modeling of the Gulf of St. Lawrence are employed in this chapter. The fourth chapter provides a description of the fundamentals of ANN methodology used in the predictions research, including two ANN algorithms, namely feedforward and modular neural networks, and discusses the advanced optimizing techniques conducted in order to establish the best structure and parameters of ANNs. The fifth chapter describes the data and modeling strategy used in our experiments, discusses the results of two different ANN architectures in relation to two proposed models (i.e., batch and sequential model), and compares the results of ANN tests with the results of coupled ice-ocean model. The sixth chapter presents the conclusions and suggests guidelines for future investigations. Finally, all references and appendixes are supplemented at the end of the thesis.

1.5 Contributions of the Research

The contributions of the research can be summarized as follows:

- The research developed a novel artificial neural network-based model to predict the total ice concentrations in the Gulf of St. Lawrence in Eastern Canada;
- The research thoroughly investigated the effect of changing the neural network structure on the performance of the model;
- The research developed a methodology to find the optimal number of points for regional modeling and predicting of sea ice concentration;

- The research significantly improved the accuracy of predicting the total ice concentrations compared with previous work.

2 PRODUCTION AND FORMAT OF THE ICE CHARTS

Canada has the largest ice areas in the world, which requires an extensive national ice service (Haykin et al., 1994). Operational ice monitoring is performed in ten regions by the Canadian Ice Service (CIS). The Canadian Ice Service is responsible for collecting and analysing data on ice conditions in all regions of the country where sea ice is present. In summer, CIS focuses on ice conditions in the Arctic and the Hudson Bay region. In winter and spring, attention shifts to the Labrador coast and East Newfoundland waters, the Gulf of St. Lawrence, the St. Lawrence SeaWay, and the Great Lakes (Haykin et al., 1994).

2.1 What is an Ice Chart?

The Canadian Ice Service is responsible for providing the ice information in the Canadian waters, mainly through its daily ice charts (Figure 2.1). To do this, the CIS uses various space-borne and airborne remote sensors, shore station observations, and shipboard ice observations (Canadian Ice Service, 2002). The charts use the North American Datum 1927 (NAD 27) and the Lambert conical projection. The World Meteorological Organization (WMO) symbolization for ice information, frequently referred to as the "Egg Code," is used to describe the ice conditions (see Figure 2.2). Boundaries are drawn around the ice areas with different concentrations; each is represented by an egg code (Canadian Ice Service, 2002).

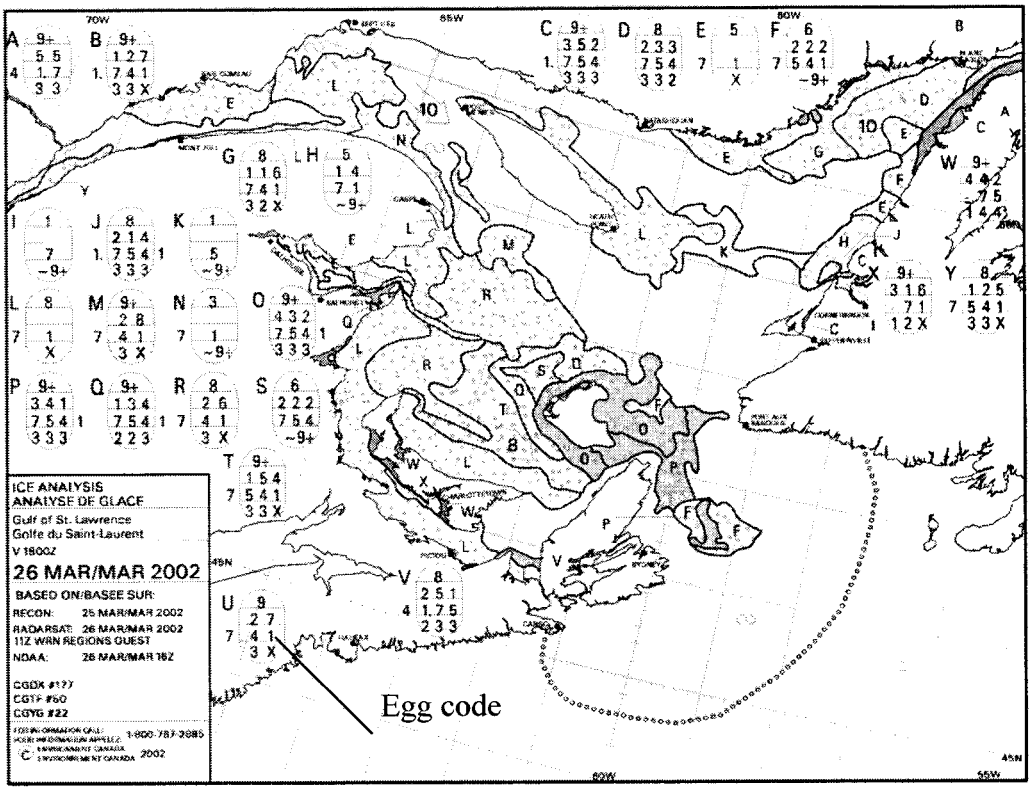

Figure 2.1 An example of the CIS ice chart for the Gulf of St. Lawrence (Courtesy of CIS).

An egg code is an oval shaped symbol, which contains three parts that describe the concentration of the ice, the stage of development (age) of the ice concentration, and the predominant form of ice (floe size). These are expressed by up to 12 numerical values. The concentration of the ice represents the ratio between the area of the water surface covered by ice and the total area, and is expressed in tenths. The value of the ice concentration varies from 10/10 for consolidated ice to 1/10 for open water. The single uppermost parameter in the egg code represents the total concentration, which includes

all stages of development. The second row in the egg code matrix contains the partial concentration for the thickest (left), the second thickest (middle), and the third thickest (right) ice types (see Figure 2.2). The partial concentration field may contain two numbers if only two ice types are present in the area. If there is one ice type only, the partial concentration field will be left blank, as the concentration will be presented by the total concentration (see Figure 2.2).

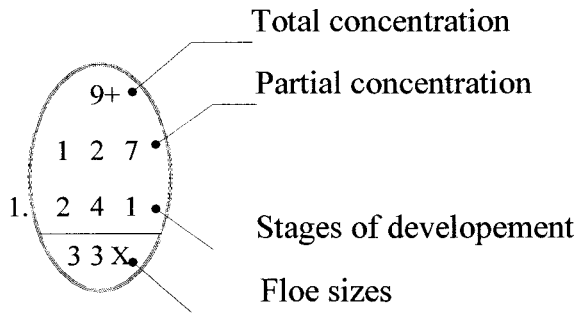

Figure 2.2 An example of the WMO egg code.

The third field in the ice code contains the stages of development (age) for the ice types reported in the partial concentration field. Thicker ice refers to older ice, and vice versa. Various codes are used, depending on the stage of development. For example, a code of "1" is assigned to the *new ice* (less than 10 cm in thickness), while a code of "9" is assigned to the *second stage thin first-year ice* (50-70 cm in thickness). Medium/thick first-year ice, as well as old ice, are assigned a dot (·) as part of their code.

The last field in the code represents the predominant forms of the sea ice (floe sizes) corresponding to the stages of development identified in the previous field. Various codes

are given to various floe sizes, which vary from "0" for the *pancake ice* to "7" for the *giant floe* (width greater than 10 km). Fast ice and icebergs are given the codes of "8" and "9" respectively. Undetermined ice forms, unknown forms, or no forms are assigned the code of "X" (see Canadian Ice Service, 2002 for more details).

2.2 Data Reconnaissance

Until recently the sea ice charting was mainly based on reconnaissance flights using a combination of visual interpretation of the ice conditions and radar identification of the ice edge (Haykin et al., 1994). Presently, the ice charts are based mainly on three sources, as shown in Figure 2.3: (1) space-borne sources (e.g., NOAA AVHRR, DMSP SSM/I, RADARSAT-1 SAR, ERS-2 SAR and ENVISAT ASAR); (2) airborne sources (e.g., Aircraft SLAR and SAR, visual observations of ice type and concentration, and ice thickness measurements from helicopter reconnaissance flights); and (3) in-situ sources (e.g., visual observations of ice type and thickness from ships, visual observations, and ice thickness measurements from shore station) (Canadian Ice Service, 2002).

2.3 Space-borne Data Reconnaissance.

Satellite data have been used as part of the data sources in ice monitoring for many years. During the last decade, sea ice charting based on satellite imagery has become gradually more important. Since 1990, visible and infrared data from NOAA-AVHRR, and passive microwave data from DMSP-SSM/I have been used as an important complement to Aircraft-based radar reconnaissance. However, these data have limitations due to cloud

cover and coarse resolution, and they are therefore not optimal for regional ice mapping, which requires detailed and regular data (Haykin et al., 1994).

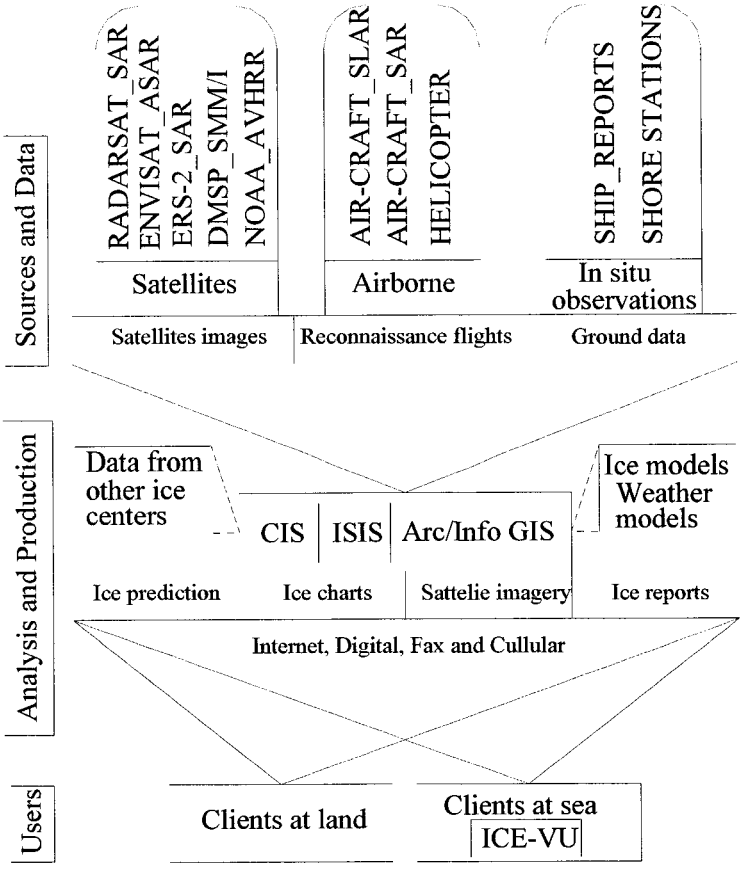

Figure 2.3 Data sources and analysis.

In 1991, ERS-1 SAR data represented an improvement of ice monitoring quality. With space-borne SAR data, which combines high spatial resolution with independence of cloud cover and light conditions, it is possible to observe sea ice with much better accuracy than when using visible and passive microwave methods (Haykin et al., 1994). The satellite SAR technology is being improved, and SAR systems offered by the

Canadian RADARSAT and the European ENVISAT satellites have wide-swath, multimode, and dual polarization.

A number of satellite data are used to provide the best available data set for analysis of the ice conditions. The most important satellites and sensors used in operational ice monitoring are shown in Figure 2.3. Predominately, satellite imagery from RADARSAT ScanSAR, as well as from NOAA-AVHRR, DMSP-SSM/I, ERS-2 and ENVISAT-ASAR, are used (Canadian Ice Service, 2002).

2.3.1 Visible and Infrared Satellite Data

National Oceanic and Atmospheric Administration (NOAA) satellites provide imagery from sensors operating in the visible and infrared band of the electromagnetic spectrum. The most common satellite instrument used for measuring visible and infrared bands is the NOAA's Advanced Very High Resolution Radiometer (AVHRR) which provides images in different frequency channels (Haykin et al., 1994). The first operational NOAA satellite (NOAA-6) was launched in 1979. This was followed by a series of additional NOAA satellites, with the latest launch being NOAA-17 in June 2002. NOAA's 12, 14, 15, 16, and 17 are currently remaining operational (see Figure 2.4) (Bertoia and Manore, 2001; NOAA Satellites and Information, 2003a). The latest AVHRR sensor is a six-channel scanner that senses the visible, near-infrared, and thermal infrared portions of the electromagnetic spectrum. The latest AVHRR/3 is used to produce images with a spatial resolution of 0.5 km for visible or 1.0 km for infrared and swath width of 2940 km (see

Table 2.1) (Canadian Centre for Remote Sensing, 2003; NOAA Satellites and Information, 2003a). As shown in Figure 2.5, the AVHRR resolution and swath is good for general ice mapping (Haykin et al., 1994). The processed NOAA AVHRR data are received at the CIS by means of a data communication from Edmonton, Alberta (Ramsay, 2000; Bertoia and Manore, 2001).

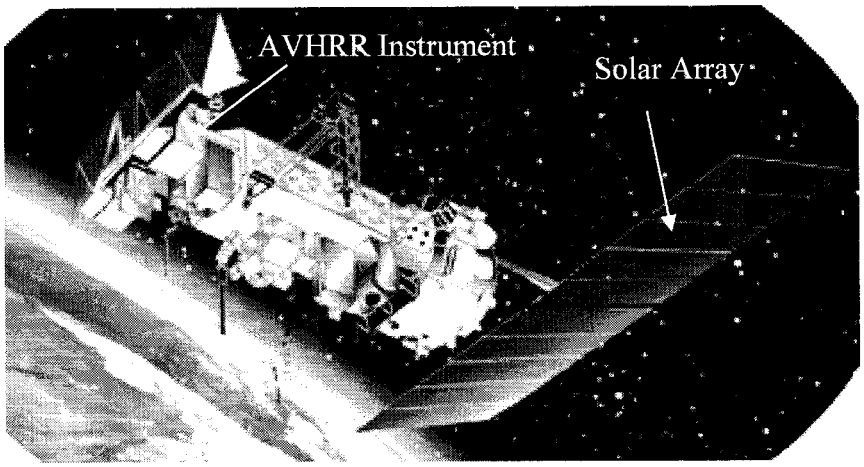

Figure 2.4 Conceptual view of NOAA Satellite. (Courtesy of NASA's Goddard Space Flight Center, 2003)

Figure 2.5 An example of a part from NOAA AVHRR image. (Courtesy of CIS)

Table 2.1 Advanced Very High Resolution Radiometer (AVHRR).

Band #	NOAA-6,8,10 AVHRR	NOAA-7,9,11,12,14 AVHRR/2	NOAA-15,16,17 AVHRR/3	Spectral region
1	0.58 - 0.68 μm	0.58 - 0.68 μm	0.58 - 0.68 μm	visible
2	0.725 - 1.10 μm	0.725 - 1.10 μm	0.72 - 1.00 μm	near - IR
3A (day)	---	---	1.58 - 1.64 μm	thermal - IR
3B (night)	3.44 - 3.93 μm	3.44 - 3.93 μm	3.55 - 3.93 μm	thermal - IR
4	10.30 - 11.30 μm	10.30 - 11.30 μm	10.30 - 11.30 μm	thermal - IR
5	11.50 - 12.5 μm	11.50 - 12.4 μm	11.50 - 12.5 μm	thermal - IR
Swath	2940 km	2600 km	2940 km	----
Resolution	visible: 1.10 km infrared: 1.10 km	visible: 0.50 km infrared: 1.00 km	visible: 0.50 km infrared: 1.00 km	----
Notes	1.) NOAA-13 failed 2.) Channels 3A and 3B are time shared			

2.3.2 Passive Microwave Satellite data

Passive microwave remote sensors are radiometers that measure the thermal emission from the ground at microwave wavelengths. The first and most common satellite instrument used for providing passive microwave imagery is Special Sensor Microwave Imager (SSM/I). SSM/I on board U.S. Defence Meteorological Satellite Program (DMSP) satellites has provided data since 1987. The first SSM/I instrument was launched in June 1987; aboard the DMSP 5D2-F8. This was followed by a series of additional DMSP satellites, the latest launch being DMSP 5D3-F15 in December 1999 (see Figure

2.6). Since the SSM/I satellites are subject to limited operational lifespans, only three SSM/I satellites, namely F13, F14, and F15, currently remain operational (Global Hydrology Research Center, 2003; NOAA Satellites and Information, 2003b).

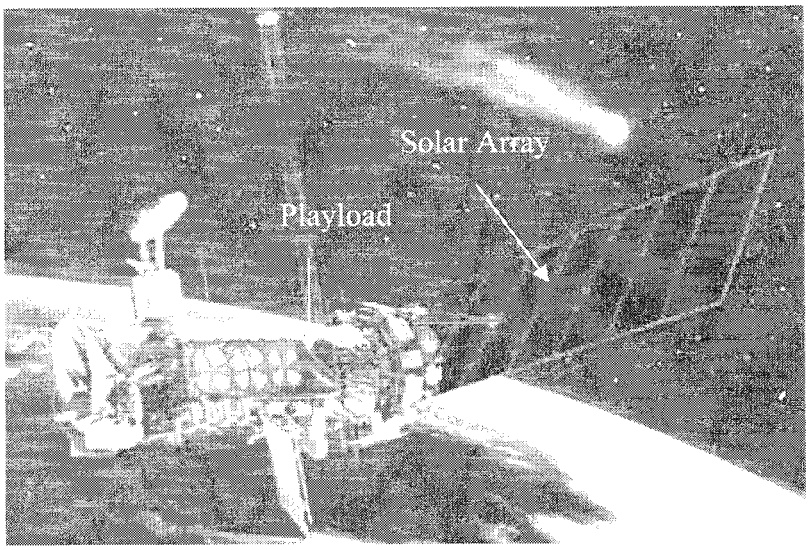

Figure 2.6 Conceptual view of DMSP 5D3-F15 Satellite (Courtesy of Gunter's Space Page, 2003).

The DMSP 5D3-F15 SSM/I is a seven-channel, four-frequency, linearly polarized, passive microwave radiometer, which measures radiation emitted from the earth at 19.35, 22.235, 37.0, and 85.5 GHz. The SSM/I radiometer simultaneously measures the microwave emission originating from the earth's surface and the intervening atmosphere. The SSM/I receives both horizontally and vertically linearly polarized radiation at 19, 37, and 85 GHz. The 22 GHz frequency receives only vertically polarized radiation. The SSM/I ground resolution varies in the range 10 to 50 km, depending on the wavelength, and Swath width is 1400 km (Global Hydrology Research Center, 2003). The SSM/I is

the only satellite system that provides regular and girded data sets that are useful in sea ice forecasting models (Haykin et al., 1994). The U.S. National Ice Centre (NIC) provides the DMSP SSM/I data to the CIS over the North American Ice Link (NAIL) (Bertoia and Manore, 2001).

2.3.3 Active Microwave Satellite data

Active microwave remote sensors are known as radars, from the acronym for Radio Detection And Ranging. A typical radar sensor consists of a transmitter and an antenna. The transmitter produces pulses of electromagnetic energy at microwave wavelengths, which are timed by a synchroniser and standardised to a known power by a modulator. The spatial resolution of radar data is controlled by the pulse length and the antenna beam width, which is governed by the length of the antenna. Thus, by increasing the length of the antenna, radar data with a finer resolution may be obtained (Haykin et al., 1994).

Active microwave observations can be obtained by several types of instruments. The most common are Synthetic Aperture Radars (SAR), Side-Looking Radars (SLR), and Scatterometers. The SAR instruments provide high resolution images, with pixel size down to about 10 m, while the SLR provides medium resolution images with resolution of 1 - 2 km. Scatterometer data have coarser resolution, varying from 10 km to about 50 km. The most common wavelengths for active microwave instruments are 2.3 cm (X-band), 5.6 cm (C-band), and 23 cm (L-band) (Haykin et al., 1994).

SAR data are ideal for regional and local ice monitoring because of the high resolution (about 100 m), which gives detailed images of the ice cover (Table 2.2). SAR data are much more challenging to use in operational ice monitoring because raw SAR data from the satellite needs to be transformed to SAR images, which is a computer demanding process, and delivery of SAR data in near real-time is provided by only a few receiving and processing stations (Haykin et al., 1994). Routinely available active microwave satellite data consist of imagery from RADARSAT, ERS-2, and ENVISAT satellites, as reviewed in Table 2.2.

Table 2.2 Satellite active microwave-based data sets used by Canadian Ice Service.

Mission	Country or Agency	Frequancy (GHz)	Band	Polarization	Swath (km)	Spatial resolution (m)
RADARSAT-1 SAR	Canada	5.300	C-band active microwave	HH	35-500	10-100
ERS-2 SAR	ESA	5.300	C-band active microwave	VV	100	100
ENVISAT ASAR	ESA	5.300	C-band active microwave	HH, VV HH/VV HH/HV VV/VH	100- 400	30-1000

Electromagnetic waves may be either horizontally (H) or vertically (V) polarised, with H polarised waves having an electric field parallel to the target and V polarised waves having an electric field perpendicular to the target. Radars are capable of measuring the backscattering response for various polarisation configurations. A polarimetric radar is capable of measuring the radar response for VV, HH, HV, and VH, where the first letter

denotes the polarisation of the transmit antenna and the second letter denotes the polarisation of the receive antenna (Haykin et al., 1994).

2.3.3.1 RADARSAT

The first Canadian RADAR SATellite (RADARSAT-1) was developed by the Canadian Space Agency (CSA) and was launched in November 1995, containing a C-band (5.3 GHz) HH polarisation SAR instrument (Figure 2.7). It was the most advanced SAR yet to go into permanent orbit (Flett et al., 2001). The RADARSAT SAR has the unique ability to shape and direct its radar beam to image swaths from 35 km to 500 km, with resolutions of from 10 m to 100 m, respectively. Incidence angles can be varied from less than 20° to more than 50°. RADARSAT is in a sun-synchronous polar orbit at an altitude of approximately 798 km, with a repeat cycle every 6 days using the 500 km swath, and every 24 days using the standard 100 km swath mode (Nazarenko et a., 1995; Parashar, 1994).

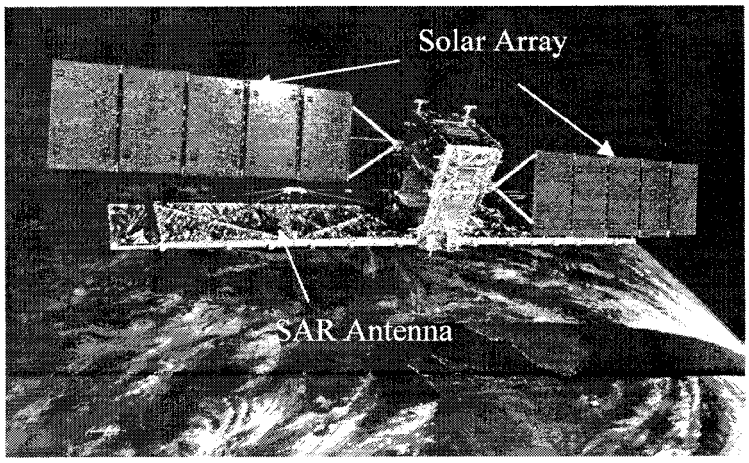

Figure 2.7 Conceptual view of RADARSAT-1 satellite. (Courtesy of CIS)

The RADARSAT SAR is very flexible and is capable of acquiring data at seven different beam modes, which have different resolutions and areas of coverage on the earth's surface. The CIS makes frequent use of the ScanSAR of RADARSAT which provide nominal swaths, ScanSAR wide mode of 500 km at 100 m resolution, or ScanSAR narrow mode of 300 km at 50 m resolution. These modes are preferred because of the excellent geographic coverage and revisit capabilities at sufficient resolution for interpretation of significant ice features, as shown in Figure 2.8 (Ramsay et al., 1998; 2001).

Canadian data reception from the RADARSAT is provided by two Canada Centre for Remote Sensing (CCRS) facilities at Gainteau, Quebec and at Prince Albert, Saskatchewan. All data are processed into image products at the Canadian Data Processing Facility (CDPF), Gatineau, Quebec. An Anik satellite link is used to move signal data from the Prince Albert site to Gatineau prior to processing (Ramsay et al., 1998; 2001). The processed data are received at the CIS in Ottawa by means of a dedicated T1 connection, the Image Transfer Network (ITN), within 2-3 hours of image acquisition (Ramsay et al., 1998; Flett, 2002).

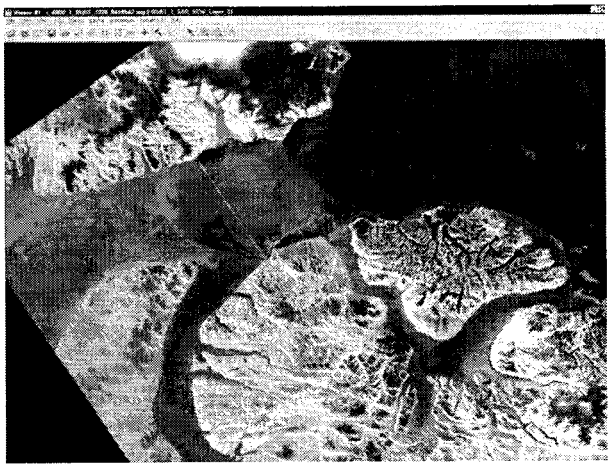

Figure 2.8 An example of a part from RADARSAT SAR image. (Courtesy of CIS)

2.3.3.2 ERS-2

The European Remote Sensing (ERS-2) satellite was developed by the European Space Agency (ESA). It was launched in April 1995 and carried on board various advanced instruments for earth observation (Figure 2.9). Of interest to ice applications is the Active Microwave Instrument (AMI), which comprises two separate radars: a SAR and a wind scatterometer. The AMI-SAR instrument operates in the C-band at 5.3 GHz with a VV polarisation. The synthetic aperture radar on board ERS-2 is used to produce images with a spatial resolution of 50 m and swath width of 100 km (Attema et al., 1998). The ERS satellite has a sun-synchronous orbit of approximately 785 km with a repeat cycle of 35 days (Canadian Centre for Remote Sensing, 2003). The processed ERS-2 data are received at the CIS by means of a dedicated T1 connection, the ITN from Gatineau, Quebec (Ramsay, 2000; Bertoia and Manore, 2001).

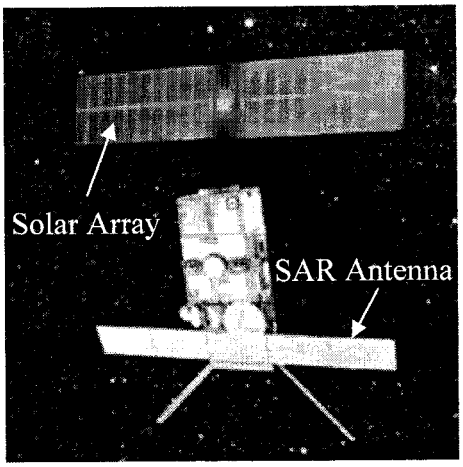

Figure 2.9 Conceptual view of ERS satellite. (Courtesy of CIS)

2.3.3.3 ENVISAT

The European Space Agency launched another advanced SAR satellite in April 2002, the earth and atmospheric ENVIronmental SATellite (ENVISAT). It carries on board various advanced instruments for earth observation (Figure 2.10). A C-band Advanced Synthetic Aperture Radar (ASAR) is a major instrument on ENVISAT. The flexible swath width (100-400 km), spatial resolution (30-1000 m), incidence angle (10°-60°), and polarization diversity provide users with many data options suited to a variety of applications (Canadian Centre for Remote Sensing, 2003). ASAR exploits its intrinsic design flexibility through five operational modes. The Alternating polarization mode provides images with high spatial resolution data products of 30 m in HH and VV, HH and HV or VV and VH (Densos et al., 2000; Mancini et al., 1996). The Alternating polarisation mode can help better identify the boundaries between sea ice and open water.

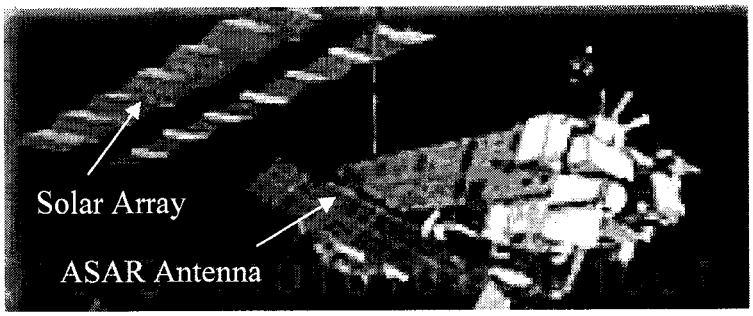

Figure 2.10 Conceptual view of ENVISAT. (Courtesy of CIS)

ENVISAT operates in a sun-synchronous polar orbit at an altitude of approximately 800 km, and the ground track of the satellite is repeated every 35 days. The processed ENVISAT data is received at the CIS by means of a dedicated T1 connection, the Image Transfer Network (ITN), from Gatineau, Quebec (Ramsay, 2000; Bertoia and Manore, 2001).

2.4 Airborne Data Reconnaissance

Aerial reconnaissance data generally provides reliable high quality information about ice conditions over portions of regional areas such as the Gulf of St. Lawrence. Using aircraft as platforms from which to conduct ice reconnaissance, a nearly synoptic description of ice conditions can be obtained. Aerial imaging radars can be classified into two types as shown in Table 2.3, where Aircraft-SLAR and SAR are active microwave sensors using X band, HH polarised. The first type is the Side Looking Airborne Radar (SLAR), in which a radar pulse is transmitted by an antenna fixed below a Canadian Ice Center's Dash 7 aircraft to image large ground areas adjacent to the flight line. The echoes are processed to produce an amplitude/time video signal which is then recorded as an image

line, with brighter pixels indicating higher energy returns. With SLAR, imagery may be acquired as the total swath coverage varies from 50 to 200 km, and the resolution from 25 to 400 m. (Canadian Ice Service, 2002; Haykin et al., 1994).

The second type of airborne imaging radar is the Synthetic Aperture Radar. This radar forms an image by a different process; it uses a relatively short antenna to produce a wide beam. The image is built up by successive scans, but the radar also makes use of the Doppler history of the surface being scanned as the aircraft moves forward. The Canadian Ice Service uses, under contract, the aircraft SAR system, namely, the Sea Ice and Terrain Assessment system. The aircraft SAR operates in the X-band at 3.2 cm with HH polarization. The total swath coverage is 200 km with a resolution of 25 m (Canadian Ice Service, 2002; Haykin et al., 1994).

Table 2.3 Airborne data sets used by Canadian Ice Service.

Source/Sensor	Country or Agency	Frequancy (GHz)	Band	Polarization	Swath (km)	Spatial resolution (m)
Aircraft SLAR	CIS	9.600	X-band active microwave	HH	200	25-400
Aircraft SAR	Intermap Technologies	9.600	X-band active microwave	HH	200	25

Reports about the ice cover taken from helicopters have the advantage of a much better viewing angle. In addition the platform's flying speed allows much more of the sea ice to be reported. The ice observers are trained to recognize the various stages of development

of sea ice, to estimate its amount, and to record its deformation and the snow-cover or stage of decay. All these data are provided by visual estimates, and both training and experience are required to make the information reliable (Canadian Ice Service, 2002).

2.5 In-Situ Observations

Although the broad knowledge of the extent of sea ice cover has been revolutionized by satellite imagery, observations from shore stations and ships are still of great importance in establishing the "ground truth" of satellite observations.

Reports about the ice cover taken from the ships provide very detailed ice observations, as well as information on the characteristics of the ice not acquired by aerial reconnaissance methods – such as snow depth, ice thickness, and ice behaviour. On a ship station, it is obvious that a better view of the ice is obtained if the observation is made from a point as far above the sea as possible. These detailed observations of the ice are used to make more accurate interpretations of aerial charts and for climatological studies. Therefore, shipboard ice observers should always record ice conditions to the maximum detail possible (Canadian Ice Service, 2002).

Ice observations from shore stations are similar to those from ships since the area being observed is limited. The exception exists for ground level stations that are placed high above the area being observed, where the perspective becomes more like a low-level aerial view. The observer should follow the guidelines previously described for identifying ice types and ice boundaries and for estimating ice concentrations (Canadian Ice Service, 2002).

2.6 Data Processing (Integration and Analysis)

When satellite data arrive at the ice centres, a number of data processing steps must be performed to develop the final product. Normally, the ice centres produce ice charts – interpreted images or special ice reports which are sent out to the end users. The main processing steps include: (1) geolocation and transformation of the image to a map projection (for example a Lambert Conic Conformal map projection); (2) integration of satellite data with other ice data (aircraft observation, ship observation, etc.), meteorological data, and oceanographical data, which is usually done in a Geographic Information System (GIS); (3) image interpretation; and (4) production of ice charts (Haykin et al., 1994).

The Geographic Information System (GIS) capabilities of the display system are used to produce the final "ice chart" as well as a variety of other image and map products. The Canadian Ice Service uses a software package developed by the Environment Systems Research Institute (ESRI) – called Ice Service Integrated System (ISIS) – for data handling, interpretation, and analysis. The charts use the North American Datum 1927 (NAD 27) and the Lambert conical projection. Once the data sets have been geo-referenced, ISIS can display them as images (Figure 2.11) (Ramsay et al., 1998). Then, ice image analysts perform integration of the data sets in ISIS environment. The image interpretation is still done visually by experienced ice analysts, as shown in Figure 2.12. Finally, ice chart analysis is performed, and the World Meteorological Organization (WMO) symbolization for ice information, frequently referred to as the "Egg Code," is

used to describe the ice conditions (Figure 2.13) (Ramsay et al., 1998; Canadian Ice Service, 2002).

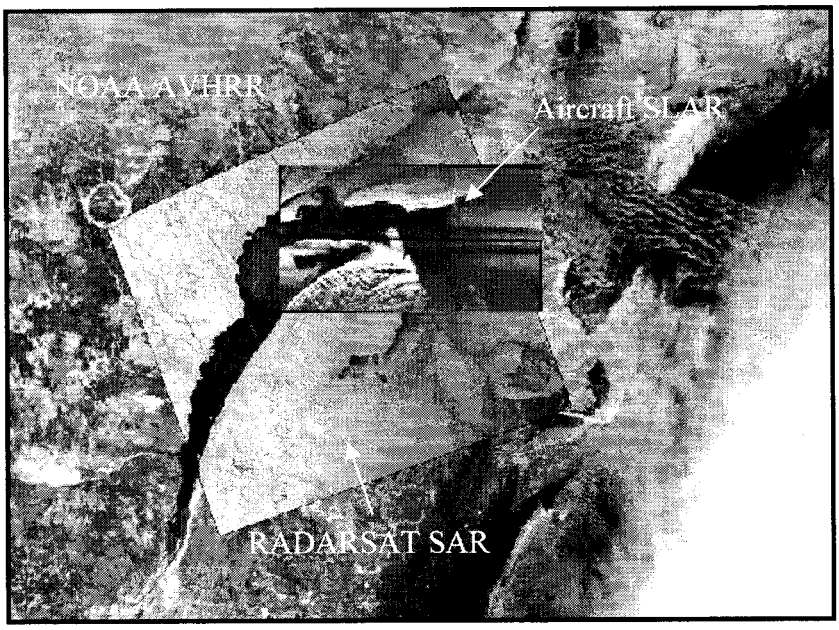

Figure 2.11 Example of ISIS composite image of the Gulf of St. Lawrence. (Courtesy of CIS)

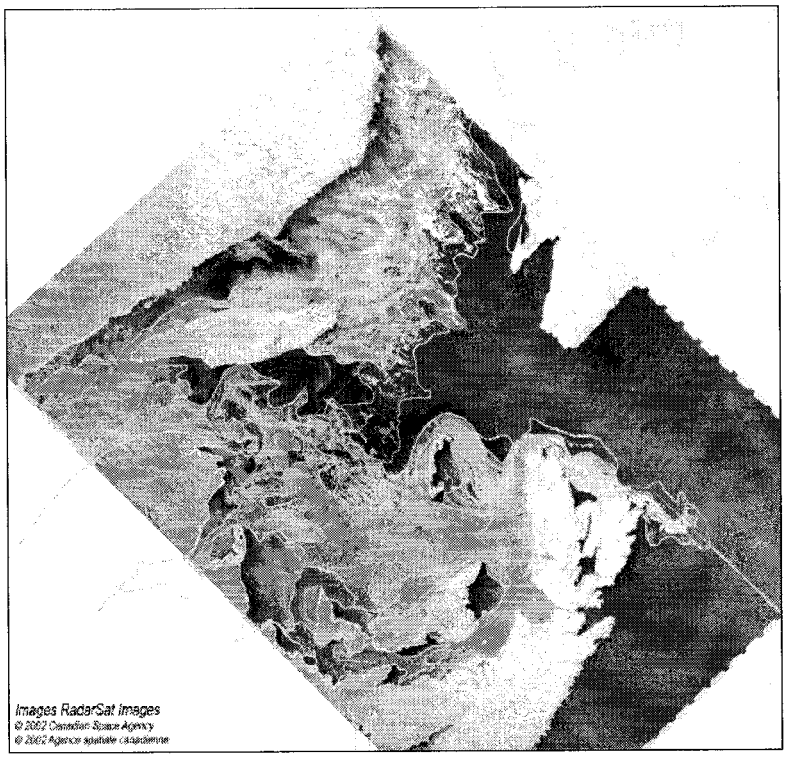

Figure 2.12 Example of image interpretation. (Courtesy of CIS, 2002)

Due to the large volumes of SAR data now available, developing algorithms for automated information extraction, such as ice classification and ice-motion measurement, is urgently needed to assist the ice analyst in fully exploiting these complex data sources. Therefore, the CIS, through the contract with Noetix Research, has developed an ice tracking algorithm and an ice/no-ice classifier, which is presently operational. These algorithms, along with a NOAA AVHRR Sea Surface Temperature (SST) extraction algorithm and an SSM/I Passive Microwave ice concentration algorithms, have been integrated into a Marine Analysis System (MAST) package that is still being investigated and implemented at Canadian Ice Services (Ramsay et al., 1998; 2001).

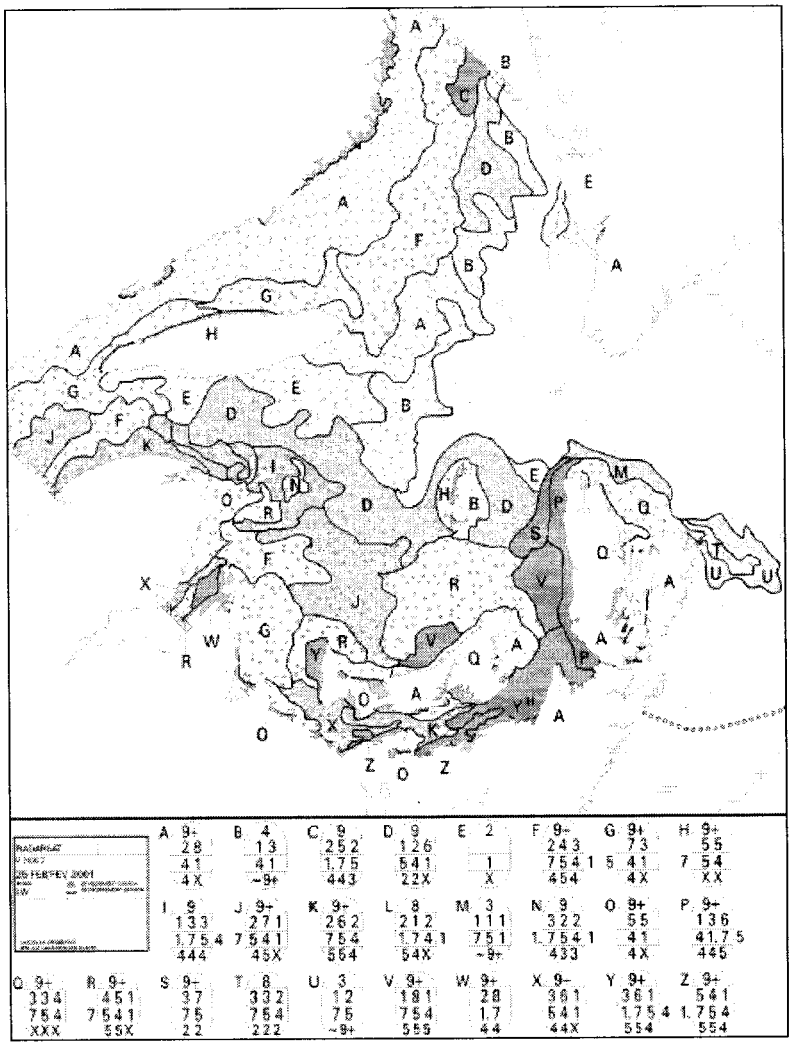

Figure 2.13 Example of an ice chart (Courtesy of CIS, 2002).

The CIS uses the Climatological Ice Data Archive System (CIDAS) to archive all the relevant ice information it acquired as well as all products produced. These include all image products sent to the Canadian Coast Guard and other clients; these are stored on-line and are available to clients in a variety of common formats. All chart products are also stored as Arc/Info format within CIDAS, and are available to clients in this and other data formats (Ramsay et al., 1998; 2001).

2.7 Products and Users

Charts available from the Canadian Ice Service include Regional Weekly Ice Charts, Daily Iceberg Analysis Charts; Daily Ice Analysis Charts, Ice Reconnaissance Charts, and Radarsat Image Analysis Charts. In addition, raw images are also available to users, depending on their ability to receive image data: SLAR images from Ice Reconnaissance Aircraft; Visual/Infrared Satellite Imagery; and SAR images from RADARSAT. Moreover, bulletins provide advice on both present and forecast ice and iceberg conditions in simple text format (Canadian Ice Service, 2002).

The CIS's products are relayed to marine customers by satellite, cellular phone, and land line links. The major user of ice information issued by CIS is the Canadian Coast Guard (CCG). All major CCG icebreakers and the Ice Operation Offices are equipped with a communication and display system application (Ice-VU) developed by CIS, designed to capture and display RADARSAT, airborne SLAR, and other data. The data are received within hours of capture, allowing Ice Operations Officers to more effectively deploy their ships to areas where ice poses a hazard. Experienced users like the CCG demand a broader range and more detailed and accurate products. Other users have almost no requirements as they simply follow ice routing guidance with icebreaker support (Canadian Ice Service, 2002; Asmus et al., 1996).

3 TRADITIONAL ICE CONDITION PREDICTION METHOD

The Canadian Ice Service has several ice models currently in operation at its center, and several new ice models are under development. The model described here is the coupled ice-ocean model of the Gulf of St. Lawrence. In this chapter, I present the ice model and the method used to couple the thermodynamic and dynamic ice model to the ocean model, which was developed by Saucier et al. (2000). The dynamic ice model is a multi-category Particle-In-Cell model used by Flato and Hibler (1992) and Flato (1994). The thermodynamic model was developed based on the work of a zero-layer Semtner (1976a) thermodynamic sea ice model. Backhaus (1983, 1985) and Stronach et al. (1993) baroclinic ocean model reproduces the ocean properties (Saucier et al., 2000).

3.1 Ice Model

The multi-category Particle-In-Cell method presented by Flato and Hibler (1992), and Flato (1994) built the ice dynamic. The momentum equation for the ice field driven by wind and water drag forces, Coriolis forces and ice interactions, as expressed in Figure 3.1, is given by (Hibler, 1979):

$$m\frac{\partial U_I}{\partial t} = \tau_{AI} + \tau_{IO} - m\hat{f}k \times U_I - mg\nabla H + \nabla \cdot \sigma \tag{3.1}$$

where m is mass per unit area, $\hat{f}$ is the carioles parameter, k is a unit vector normal to the ice surface, U_I is the ice velocity vector, g is the gravitational acceleration, ∇ is the

substantial derivative, H is the sea surface elevation, τ_{AI} and τ_{IO} are the wind and the water drag stresses and σ is the horizontal component of the internal stress tensor.

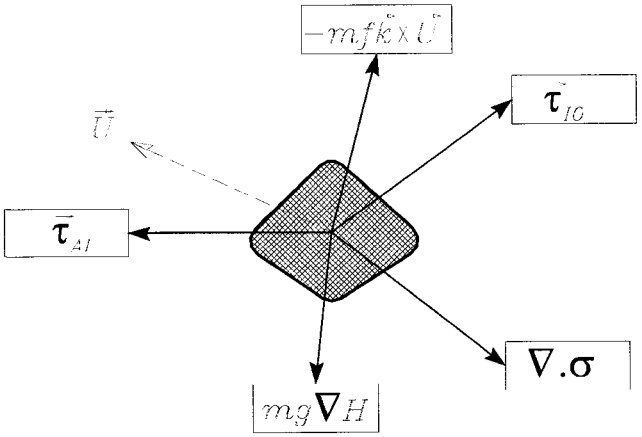

Figure 3.1 A schematic view of the force balance on a sea ice cover. (After Zhang, 2000)

τ_{AI} and τ_{IO} are assumed to be quadratic functions of the wind and ice velocities and are expressed respectively as:

$$\tau_{AI} = \rho_A C_{DAI} |U_A| (U_A) \tag{3.2}$$

$$\tau_{IO} = \rho_I C_{DIO} |U_I - U_O| (U_I - U_O) \tag{3.3}$$

where U_A is the wind velocity, U_O is the ocean surface layer velocity, ρ_A and ρ_I are the air and the ice density respectively, C_{DAI} and C_{DIO} are the respective wind and water

drag coefficients. The numerical values of the parameters for the ice, air, water, and Coriolis force are given in Appendix I.

The internal ice stress σ is derived from the Mohr-Coulomb rheology in which the shear strength is proportional to the pressure from an internal friction. This rheology is implemented in Flato and Hibler (1992). The Mohr-Coulomb failure criterion is a linear relationship between pressure and shear strength and plots as two lines in principal stress space, as shown in Figure 3.2.

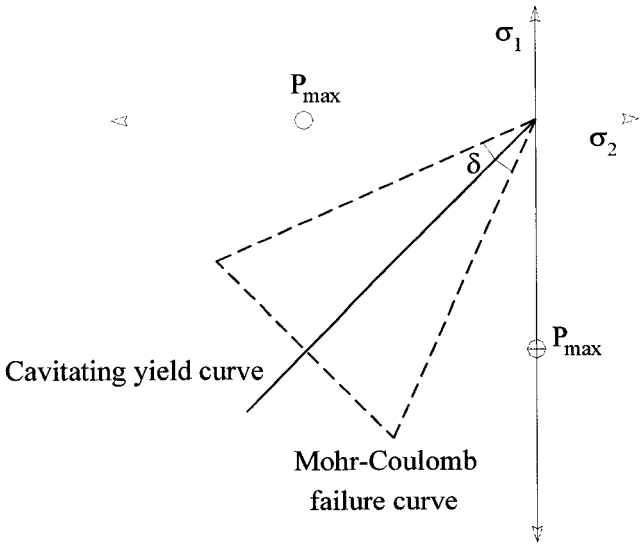

Figure 3.2 The Mohr-Coulomb failure curve. (After Flato and Hibler, 1992.)

The angle between the two failure lines δ is related to the more common "angle of shearing resistance" φ by the following definition (Flato, 1993):

$$sin\varphi = tan\left(\frac{\delta}{2}\right) \tag{3.4}$$

The maximum pressure, P_{max}, beyond which compressive failure occurs is parameterized in terms of empirical constants $p^* = 2.5 \times 104\ \mathrm{N\ m^{-2}}$ and $C = 20$, the mean ice thickness h, and ice concentration A, as (Hibler, 1979):

$$P_{max} = P^* h exp(-C(1-A)) \tag{3.5}$$

As mentioned above, the thermodynamic model of a zero-layer Semtner (1976a, 1987) is used in this model. In any thermodynamic ice model, two quantities are calculated: ice concentration, A, and ice thickness, h. Hence, the two continuity equations can be presented as (Haapala, 2002):

$$\frac{\partial A_i}{\partial t} = \nabla.(U_I A_i) + \psi_{iA} + \vartheta_{iA} \tag{3.6}$$

$$\frac{\partial h_i}{\partial t} = \nabla.(U_I h_i) + \psi_{ih} + \vartheta_{ih} \tag{3.7}$$

where A_i is the ice concentration at particular category i, h_i is the thickness for the same category, ψ_{iA} and ψ_{ih} are the thermodynamic growth rate source terms of ice concentration and thickness. ϑ_{ih} and ϑ_{ih} are the redistribution terms of ice concentration and thickness.

3.2 Ocean Model

The Backhaus (1983, 1985) and Stronach et al. (1993) baroclinic ocean model was considered. The ocean model is layered in the vertical, with a uniform resolution of 5 m down to 300 m depth, and 10 m below 300 m, except that the surface and bottom layers adjust to the local water level and depth respectively (Saucier et al., 2000). The ocean variables, which are of great important for ice-ocean coupling, are salinity, S, temperature, T, velocities, $U_O = (u,v,w)$, and the vertical turbulent mixing coefficients for momentum K_{VM}, and for density $K_{V\sigma}$. The respective equations for the conservation of mass, momentum, heat, and salt are:

$$\nabla.(u,v,w) = 0 \tag{3.8}$$

$$\frac{\partial U_O}{\partial t} + U_O.\nabla u - fU_O + \frac{1}{\rho}\frac{\partial P}{\partial x} - \frac{\partial}{\partial x}(A_H \frac{\partial u}{\partial x}) - \frac{\partial}{\partial y}(A_H \frac{\partial U_O}{\partial y}) - \frac{\partial}{\partial z}(K_{VM} \frac{\partial U_O}{\partial z}) = 0$$

(3.9)

$$\frac{\partial T}{\partial t} + u.\nabla T - \frac{\partial}{\partial x}(A_H \frac{\partial T}{\partial x}) - \frac{\partial}{\partial y}(A_H \frac{\partial T}{\partial y}) - \frac{\partial}{\partial z}(K_{V\sigma} \frac{\partial T}{\partial z}) = 0 \tag{3.10}$$

$$\frac{\partial S}{\partial t} + u.\nabla S - \frac{\partial}{\partial x}(A_H \frac{\partial S}{\partial x}) - \frac{\partial}{\partial y}(A_H \frac{\partial S}{\partial y}) - \frac{\partial}{\partial z}(K_{V\sigma} \frac{\partial S}{\partial z}) = 0 \tag{3.11}$$

where A_H is the horizontal turbulent mixing coefficient for momentum and density, $\frac{\partial P}{\partial z} = -\rho g$, P is the pressure, and ρ is the density. The vertical turbulent mixing coefficients for momentum K_{VM}, and for density $K_{V\sigma}$ are respectively:

$$K_{VM} = K_{VM0} + lqS_M \tag{3.12}$$

$$K_{V\sigma} = K_{V\sigma 0} + lqS_\sigma \tag{3.13}$$

where l is the turbulent length scale, q is twice the turbulent kinetic energy, S_M and S_σ are stability factors, and K_{VM0} and $K_{V\sigma 0}$ are background diffusivities. The stability factors, S_M and S_σ, are dependent upon the flux Richardson number (Saucier et al., 2000). The turbulent kinetic energy is determined from the super equilibrium approximation, that is, an instantaneous and local balance between turbulent energy production and dissipation. A convective diffusive adjustment is applied to statically unstable water columns (Saucier et al., 2000). Then, the horizontal eddy viscosity and diffusivity coefficient for momentum and density is described by (Saucier et al., 2000):

$$A_H = \gamma(\Delta x)^2 \left[\left(\frac{\partial u}{\partial x} \right)^2 + \left(\frac{\partial v}{\partial y} \right)^2 + 0.5 \left(\frac{\partial u}{\partial y} + \frac{\partial v}{\partial x} \right)^2 \right]^{0.5} \tag{3.14}$$

where $\gamma = 0.10$ and $\Delta x = 5 \times 10^3\ m$.

3.3 Coupling of Ice and Ocean Models

The coupling between the ocean and ice is accomplished through the consistent boundary conditions, and source terms in the salt, and heat equations accounting for frazil ice formulation in the water column (Saucier et al., 2000). The respective surface boundary conditions on temperature, salinity, and momentum are:

$$K_{V\sigma}\frac{\partial T}{\partial z} = -\left[\frac{1}{\rho_0 C_{PO}}\left[(1-A)Q_{AO} + AQ_{IO}\right]\right] \tag{3.15}$$

$$K_{V\sigma}\frac{\partial S}{\partial z} = -\left[(1-A)\left(f_{AI}(S_I - S_O) + (P-E)S_O\right) + Af_{IO}(S_{IO} - S_O)\right] \tag{3.16}$$

$$K_{VM}\frac{\partial U_O}{\partial z} = \frac{1}{\rho_0}\left[(1-A)\tau_{AO} + A\tau_{IO}\right] \tag{3.18}$$

where f_{AI} is the ice growth rate (melt) over open ocean areas, f_{IO} is the ice growth over ice covered areas, A is the ice concentration, P is the observed precipitation, $E = Q_{LAO}/L_V$ is the evaporation, Q_{LAO} is the latent heat flux, L_V is the latent heat of evaporation, S_O is the sea surface salinity, S_I is the ice salinity, and S_{IO} is the salinity at an ice-ocean interface.

The exchanges of heat and salt fluxes follow the Parkinson and Washington (1979). At the atmosphere-ice boundary, the net heat fluxes Q_{AI} is expressed as:

$$Q_{AI} = Q_{SAI} + Q_{LAI} - Q_{SW\,AI} - Q_{LW\downarrow AI} + Q_{LW\uparrow AI} \tag{3.19}$$

where Q_{LAI} and Q_{SAI} are the latent and sensible heat fluxes at the atmosphere-ocean boundary, $Q_{SW\,AI}$ and $Q_{LW\downarrow AI}$ are the short-wave and long-wave download incident fluxes, and $Q_{LW\uparrow AI}$ is the outgoing long-wave radiation. These terms are expressed as:

$$Q_{LAI} = \rho_A L_S C_{LAI} |U_A| (q_I - q_A) \tag{3.20}$$

$$Q_{SAI} = \rho_A C_{PA} C_{SAI} |U_A| (T_I - T_A) \tag{3.21}$$

$$Q_{SW} = (1 - \alpha_I) SW \tag{3.22}$$

$$Q_{LW\downarrow} = \varepsilon_I \sigma_{SB} T_A^{\,4} \left(0.68 + 0.0036 e_A^{1/2}\right)\left(1 + 0.18 C_I^{\,2}\right) \tag{3.23}$$

$$Q_{LW\uparrow} = \varepsilon_I \sigma_{SB} T_I^{\,4} \tag{3.24}$$

where SW is the short-wave radiation, α_I is the ice/snow albedo, U_A is the atmospheric current, T_A is the surface air temperature, ε_I the ice emissivity, and σ_{SB} is the Stefan Boltzmann's constant (Saucier et al., 2000). The specific humidity at temperature T_I is q_I while it is q_A at temperature T_A. The specific heat of air is C_{PA} and L_S is the latent heat of ocean ice sublimation. The thermal coupling coefficients C_{LAI} and C_{SAI} are considered constants, and are included in Appendix I.

At the atmosphere-ocean boundary, the net heat fluxes Q_{AO} is expressed as:

$$Q_{AO} = Q_{SAO} + Q_{LAO} - Q_{SW\,AO} - Q_{LW\downarrow AO} + Q_{LW\uparrow AO} \tag{3.25}$$

where Q_{SAO} and Q_{LAO} are the latent and sensible fluxes at the atmosphere-ocean boundary, $Q_{SW\,AO}$ and $Q_{LW\downarrow AO}$ are the short-wave and long-wave download incident fluxes, and $Q_{LW\uparrow AO}$ is the outgoing long-wave radiation. These terms are expressed as:

$$Q_{SAO} = \rho_A C_{PA} C_{SAO} |U_A| (T_O - T_A) \tag{3.26}$$

$$Q_{LAO} = \rho_A L_V C_{LAO} |U_A| (q_O - q_A) \tag{3.27}$$

$$Q_{SW} = (1 - \alpha_O) SW \tag{3.28}$$

$$Q_{LW\downarrow} = \varepsilon_O \sigma_{SB} T_A^{\,4} \left(0.68 + 0.0036 e_A^{1/2}\right)\left(1 + 0.18 C_1^{\,2}\right) \tag{3.29}$$

$$Q_{LW\uparrow} = \varepsilon_O \sigma_{SB} T_O^{\,4} \tag{3.30}$$

in which α_O is the ocean Albedo, ε_O is the ocean emissivity, and L_V is the latent heat of vaporization.

At the ice-ocean interface, the heat flux from ice Q_{IO} is expressed as:

$$Q_{IO} = \rho_O C_{PO} C_{SIO} |U_I - U_O| (T_O - T_f) \tag{3.31}$$

where T_f is the fusion temperature for ocean water and is expressed as (Saucier et al., 2000):

$$T_f = \left(-0.0575S + 1.710523 \times 10^{-3} S^{3/2} - 2.154996 \times 10^{-4} S^2 \right) {}^{o}C \tag{3.32}$$

Finally, within the ice cover, the conductive heat flux through the ice $Q_I(T_I)$ is expressed as:

$$Q_I(T_I) = k_I h^{-1}(T_I - T_{IO}) \tag{3.33}$$

where k_I is the ice thermal conductivity (computed below), T_{IO} is the temperature at the base of the ice, and h is the ice thickness.

The atmosphere-ice heat flux is assumed to balance the conductive heat flux through the ice, Q_I. The atmosphere at the surface of the ice, T_I, is then obtained at every time step for each thickness category from the implicit solution to $Q_{AI}(T_I) - Q_I(T_I) = 0$.

3.4 Numerical Solution

The ice model in the Gulf of St. Lawrence (GSL) study is solved numerically following Flato (1993). The ice velocity field is obtained by solving the momentum equations by the Eulerian finite difference method on underlying fixed Eulerian grid. Then, the ice concentration A and ice thickness h are calculated by solving the continuity equations

by the Particle-In-Cell method (PIC). The PIC method converts the ice volume into individual particles whose motions are integrated in a quasi-Lagrangian mode. Each particle is associated with a constant ice volume in modeling. The particle velocities are then evaluated by interpolating the velocities at the nodes onto the particle positions. The ice concentration and thickness are associated with the local particle distribution within a region (Flato, 1993).

The ocean model in the GSL study is solved numerically following Stronach et al. (1993). The solution technique for ocean model is based on the model developed by Backhaus (1985). The finite difference method is used to solve the ocean model and has the same grid size as the corresponding ice model. It should be noted that in the coupled model run, when integrating the ice model the variables in the ocean model remain unchanged, and vise versa, as shown in Figure 3.3.

In fact, atmospheric forcing – from reliable weather models – of coupled ice-ocean model is very important to couple the weather model with the coupled ice-ocean model. At the Canadian Ice Service, the operational coupled ice-ocean model of the Gulf of St. Lawrence operates during the wintertime. The atmospheric forcing comes from Canadian Meteorological Centre (CMC) through the regional Canadian operational weather forecast model developed by Cote et al. (1997a, 1997b), namely, Global Environmental Multi-scale/Numerical Weather Prediction (GEM/NWP) model. The model has been operational in CMC since September 15, 1998 (Canadian Meteorological Centre, 2003).

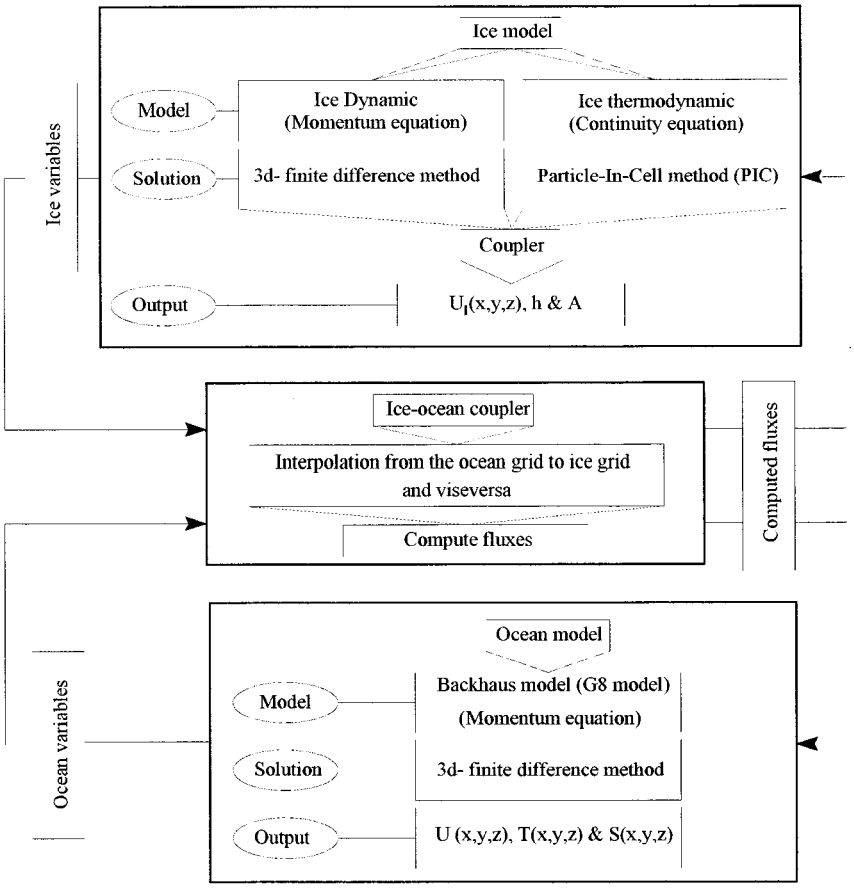

Figure 3.3 Solution strategy of GSL's coupled ice-ocean model.

3.5 Results of Coupled Ice-Ocean Model

In the ice-ocean model of the Gulf of St. Lawrence, which was developed by Saucier et al. (2000), the depth coordinate baroclinic ocean model developed from Backhaus (1985) and Stronach et al. (1993), coupled to zero-layer Semtner (1976a) thermodynamic sea ice model with cavitating fluid, pack ice dynamics using Mohr-Coulomb rheology developed by Flato and Hibler (1992). The ocean is layered in the vertical with a uniform resolution of 5 m down to 300 m depth, and 10 m below 300 m, except that the surface and bottom

layers adjust to the local water level and depth respectively. The model was applied over a period starting in December 1996 and ending in March 1998, and then compared with available observations. The atmospheric forcing was provided by the Canadian operational weather forecast model. Prior to February 24, 1997, the model was the regional finite element model developed by Mailhot et al. (1997), and thereafter it was the hydrostatic primitive equations GEM developed by Cote et al. (1997a, 1997b). The result showed that the mean concentration is well reproduced. It is undervalued by 10 to 15% during winter, and 10 to 50% during the spring. In other words, the average prediction accuracy is undervalued by 20% on average (Saucier et al., 2000).

4 ARTIFICIAL NEURAL NETWORK MODELING

In this chapter, the theory of Artificial Neural Networks (ANNs) is described and their main elements are demonstrated. Then two kinds of networks are reviewed in detail: the feedforward neural network and the modular neural network trained by backpropagation of error. Model architectures, training methods, and learning processes are also discussed. Finally, two techniques to measure the success of prediction models are discussed.

4.1 What is a Neural Network?

Artificial neural networks (ANN) are artificial intelligence (AI) methods structured according to the human brain. ANNs are computational models that imitate the human brain in performing a particular task (Haykin, 1999). From the time they were introduced to the scientific field, ANNs have been investigated according to two different scientific approaches. First, the biological aspect explores ANNs as simplified simulations of the human brain and uses them to test the hypotheses on human brain functioning. The second approach treats ANNs as technological systems for complex information processing (Haykin, 1999). This work focuses on the second approach in which ANNs are evaluated according to their efficiency in dealing with complex problems, especially in the area of prediction.

The reason why ANNs often outperform traditional methods lies in their ability to analyse incomplete, noisy data, to deal with problems that have no clear-cut solution, and to learn from historical data. Because of those advantages, ANNs have successfully

predicted ice conditions data series that have a high degree of volatility and fluctuation. The disadvantages of ANNs include the lack of tests of statistical significance of the ANNs model and estimated parameters (Haykin, 1999). Furthermore, there are no established paradigms for deciding which architecture is the best for certain problems and data types – the main subject of this work. Despite those disadvantages, many research results show that neural networks can solve almost all problems more efficiently than traditional modeling. It has been mathematically proven that three-layer neural networks having arbitrarily activating function are capable of approximating any nonlinear function (Haykin, 1999).

4.2 Processing Elements (Artificial Neurons)

ANN consists of processing elements, or neurons, that are massively interconnected. Each of the connecting links is characterized by its own weight, or strength. Figure 4.1 represents a block diagram of a simple model of a neuron, showing the weights of the various links. An activation function $\varphi(v_k(n))$, such as a sigmoid function or a hyperbolic target function, is applied to limit the amplitude of the neuron (Haykin, 1999). Finally, an external bias, b_k, is applied to increase or lower the net input of the activation function. The neural network is trained to find the optimal values for weights and biases.

The above structure for a neuron k can be represented mathematically as:

$$\upsilon_k = \sum_{j=1}^{m} w_{kj} x_j + b_k = \sum_{j=0}^{m} w_{kj} x_j \tag{4.1}$$

$$y_k = \varphi(v_k) \tag{4.2}$$

where $x_0, x_1, x_2, \cdots, x_m$ are the input signals; v_k is the activation potential of neuron k; y_k is the output signal, and $w_{k0}, w_{k1}, w_{k2}, \cdots, w_{km}$ are the weights of the neuron k. It should be noted in equation 4.1 that the values of $x_0 = +1$ and $w_{k0} = b_k$, respectively.

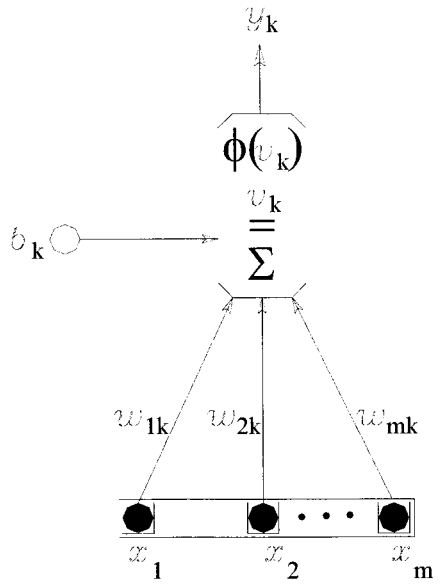

Figure 4.1 Simple neuron model.

4.3 Activation Functions

There are many possible activation functions. The most frequently used activation functions are a step, a signum, a linear, a threshold linear, a sigmoid, and a hyperbolic tangent.

The step function produces only two values (0 or 1). If I is the predefined threshold value, the output in the step function is computed according to the formula (Bishop, 1995):

$$y_k = \begin{cases} 0 & if \quad v_k \le I \\ 1 & if \quad v_k > I \end{cases} \tag{4.3}$$

A signum function is a special form of the step function, when the threshold $I = 0$ (Bishop, 1995):

$$y_k = \begin{cases} -1 & if \quad v_k \le 0 \\ 1 & if \quad v_k > 0 \end{cases} \tag{4.4}$$

The signum function was used in the first neural network-Perceptron. Step and signum functions are rarely used at the present time since they cannot approximate the majority of real-world continuous functions.

A linear, and linear threshold functions have the following forms respectively (Bishop, 1995):

$$y_k = \alpha v_k \tag{4.5}$$

$$y_k = \begin{cases} 0 & if \quad v_k \le 0 \\ v_k - I & if \quad v_k > 0 \end{cases} \tag{4.6}$$

It should be noted that the linear threshold is a special form of the linear function, and according to this function, a neuron has a non-zero output only when its input reaches the threshold *I*.

A sigmoid (or logistic) function is one of the most used activation functions in ANN modeling. It is shown in Figure 4.2(a), and its formula is described by (Haykin, 1999; Kamruzzaman and Aziz, 2002):

$$y_k = \frac{1}{1 + exp(-\alpha v_k)} \tag{4.7}$$

where the parameter α represents the slope of the sigmoid function. The function results in continuous value in [0,1] interval. It is used, for example, in feedforward and modular networks and is, together with hyperbolic tangent, one of the most frequently used functions in ANN modeling.

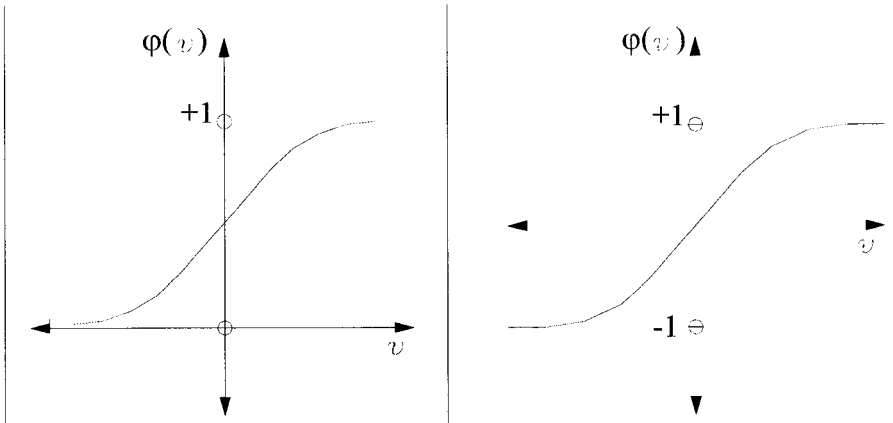

a. Sigmoid function

b. Hyperbolic tangent

Figure 4.2 Activation functions - sigmoid and hyperbolic tangent function.

A special form of a sigmoid function is the hyperbolic tangent function. It is shown in figure Figure 4.2(b) and is described by (NeuralWare, 2001a; Kamruzzaman and Aziz, 2002):

$$y_k = \frac{exp(\alpha v_k) - exp(-\alpha v_k)}{exp(\alpha v_k) + exp(-\alpha v_k)} \tag{4.8}$$

The graph of the hyperbolic tangent function is similar to the graph of the sigmoid function, except the value of interval is here [-1,1]. Because of its ability to map values into positive as negative regions, this function was used in all our experiments.

Finally, the most recently used activation functions are the Logarithmic and Arctangent functions, and their respective formulas can be defined as (Kamruzzaman and Aziz, 2002):

$$y_k = \begin{cases} ln(v_k + 1) & v_k \geq 0 \\ -ln(-v_k + 1) & v_k < 0 \end{cases} \tag{4.9}$$

$$y_k = arctan(v_k) \tag{4.10}$$

4.4 Architecture of Neural Networks

The natural neurons, when connected, form the neural nerves. In ANN modeling, the artificial neurons are connected in many different ways, forming architectural characteristics. The learning algorithms and the architectures are closely related. It is important to clearly understand how the artificial neurons are interconnected to form the

specific architectures, because this aspect defines how the computer implements the architectures. Artificial neural networks can be designed in various ways depending on how the neurons are structured and the learning algorithms, or rules, used. Network architectures may be classified as single-layer feedforward, multi-layer feedforward, and recurrent networks (Haykin, 1999)

4.4.1 Single-Layer Feedforward Networks

In this simple network, a layer of input neurons is connected to a layer of output neurons. The single-layer designation refers to the output layer. The layer of input neurons is not considered because it does not process computation over the input values (Haykin, 1999). Figure 4.3 shows a single-layer network of 3 inputs and 2 output nodes.

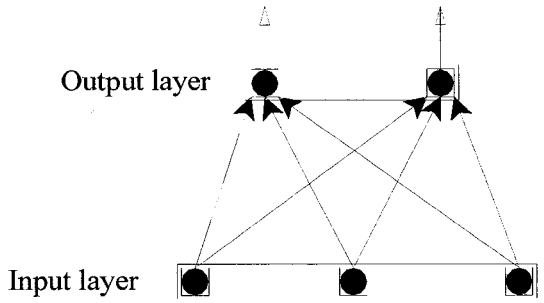

Figure 4.3 Single layer network [3-2].

4.4.2 Multi-layer Feedforward Networks

In this architecture, one or more hidden layers of neurons are present. Those networks are able to deal with higher-order problems because of the extra set of connections and the

extra dimension of neural iterations (Haykin, 1999). Figure 4.4(a) shows a multi-layer 3-3-2 network; that means a network formed by an input layer with 3 neurons, one hidden layer with 3 neurons and an output layer with 2 neurons. The network is fully connected because each neuron in one layer is connected to all neurons in the next layer. It may also happen that not all the neurons of one layer are connected to all neurons of the subsequent layer (Haykin, 1999); this may occur when the user has a certain previous knowledge about the pattern being classified. Figure 4.4(b) shows a semi connected multi-layer [3-3-2] network.

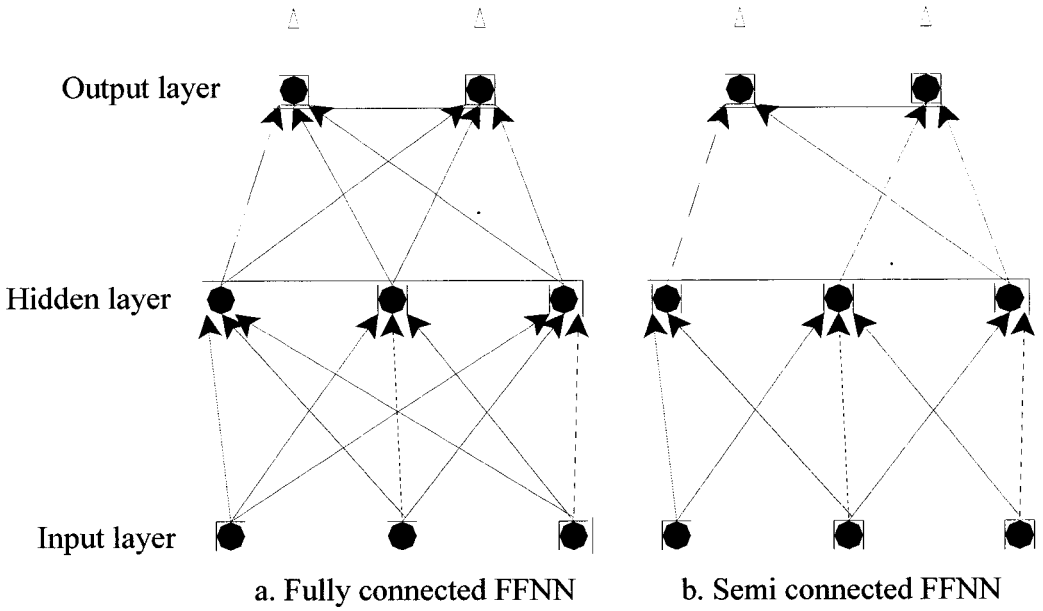

Figure 4.4 Multilayer FFNN [3-3-2] – Fully and semi connected networks.

4.4.3 Recurrent Neural Network

This network model has at least one feedback loop. It may have the same architecture as a layered network, but the feedback is needed. The feedback can occur from the output of one neuron back to the input of another neuron, among neurons of the same layer or neurons of different layers. The feedback may also happen as a self-feedback when the output of the neuron is returned to its own input. The feedback greatly influences the network learning capability performance (Haykin, 1999). Figure 4.5 shows a single-layer recurrent network where the output signals of the neurons are fed into the input of the other neurons in the same layer.

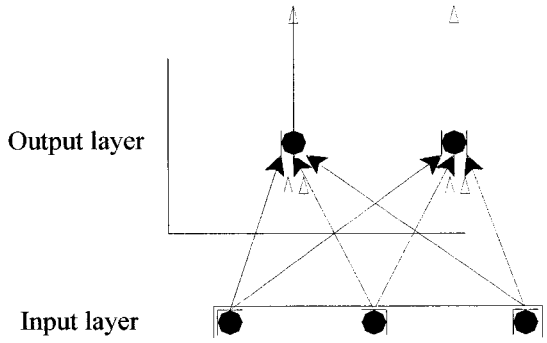

Figure 4.5 Recurrent network [3-2].

4.5 ANN Learning Algorithms

Learning is the process of calculating the weights among neurons in a network. Weights are an important factor; they determine the value of a neuron input and indirectly affect a

neuron output. There are two main types of learning in network: supervised and unsupervised (Haykin, 1999).

The difference between those two types of learning lies in the availability of known output in the training sample. In supervised learning, the set of training data consists of previous cases with known input and output values. The neural network system receives the actual output, computes the error, and adjusts the weights according to the error (Haykin, 1999).

On the other hand, the actual outputs are not known in unsupervised learning. Inputs are available to the network, and the weights cannot be adjusted based on the actual output. This type of learning is commonly used for pattern recognition problems and clustering. Kohonen's self-organizing network is based on unsupervised learning (Haykin, 1999).

Every ANN goes through three phases (NeuralWare, 2001a): (1) learning (training) phase, in which network learns on the training sample and the weights are being adjusted in order to minimize the objective function (e.g., root mean square error (RMS)); (2) testing phase, in which network is tested on the testing sample while the weights are fixed; and (3) validation (recall) phase, in which network is applied to the new cases with unknown results and in which weights are also fixed.

A learning rule represents the formula used within ANN to adjust the connection weights among neurons. Among various learning rules developed so far, three of them are commonly used in supervised ANNs (NeuralWare, 2001a): (1) Delta rule; (2) Generalized Delta rule; and (3) Delta-Bar-Delta and Extended Delta-Bar-Delta rules.

4.5.1 Delta rule

Widrow and Hoff developed a Delta rule in 1960 (Bishop, 1995). Delta rule is well known as the rule of least mean squares, because it aims to minimize the objective function by determining the weights values. The aim of Delta rule is to minimize the sum of error squares, while error is defined as the difference between the computed and desired output of a neuron, for the given input data (Haykin, 1999). Delta rule form can be defined as:

$$\Delta w_{ji} = \eta e_i y_j \tag{4.11}$$

where Δw_{ji} is the weight correction from neuron j to neuron i, η is the learning coefficient, y_j is the output value computed in the neuron j, and e_i is the raw error computed by :

$$e_i = d_i - y_i \tag{4.12}$$

where d_i is the desired output. The raw error is very rarely backpropagated; more often, the other error forms (e.g., global error E) are used. In classical FFNN, the global error, E, is backpropagated through the network using the gradient descent algorithm described in section 4.7 below.

Since Delta rule is commonly used in supervised networks, it is necessary to mention the main problem that can occur in backpropagating the error, i.e. the local minima. The local minima problem occurs when the minimum error of the function is found only for the

local area and learning is stopped without reaching a global minimum (Figure 4.6). Since the problem is mainly connected to the backpropagation algorithm, it will be discussed in details later in section 4.7.

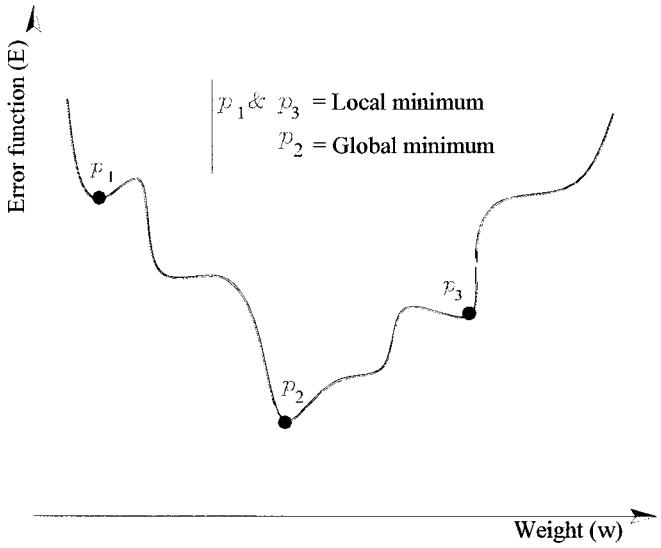

Figure 4.6 Error function plot.

4.5.2 Generalized Delta rule

A generalized form of the delta rule, developed by Rumelhart et al. (1986), is needed for networks with hidden layers. Generalized delta rule is obtained by adding a derivation of input neurons into a Delta rule equation such that weight adjustment is computed according to the formula (NeuralWare, 2001a):

$$\Delta w_{ji} = \eta e_i y_j \varphi'(v_i) \tag{4.13}$$

where v_i is the input into neuron *i*. This rule is appropriate for non-linear activation functions.

4.5.3 Delta-Bar-Delta and Extended Delta-Bar-Delta rules

As can be seen from the previous section, learning coefficient η is an important parameter for the speed and efficiency of ANNs learning, and is typically determined as single learning rate for all connections in the network. Delta-Bar-Delta learning rule was developed in 1988 by Jacobs to improve the convergence speed of the classical Delta rule. It localizes the learning rate η in a way that allows each connection in the network to have its own learning rate, changing those rates continuously as the learning progresses (NeuralWare, 2001a; Sidani and Sidani, 1994). Thus, Delta rule equation 4.11 is modified so that the learning rate is different for each connection:

$$\Delta w_{ji}(r) = \eta(r) e_i y_j \tag{4.14}$$

Despite its advantages over the classical Delta rule, Delta-Bar-Delta has some limitations; for example, it does not include momentum term in the learning equations, and some large jumps can occur in training, skipping important regions of the error surface.

To overcome these shortcomings, Extended-Delta-Bar-Delta rule (EDBD), proposed by Minai and Williams (1990), introduces a momentum term μ which also varies with time. The momentum term is used to prevent the network weights from saturation, and the EDBD rule enables local adjustment of this parameter such that the learning equation becomes (NeuralWare, 2001a):

$$\Delta w'_{ji}(r) = \eta(r) e_i y_j + \mu(r) \Delta w'^{-1}_{ji}(r) \tag{4.15}$$

where $\mu(r)$ is the momentum of the connection r in the network, and t is the time point when the weights of the connection t are adjusted.

The above learning rules use the desired output to compute the error, thus they learn in the supervised manner. If the desired output is not known, one of the unsupervised learning rules should be used, such as the Kohonen's rule.

4.6 Feedforward Neural Network Structure and Training

A three-layer feedforward neural network trained using the backpropagation algorithm is used for various areas of applications. Originally developed by Paul Werbos in 1974, and extended by Rumbelhart et al. in 1986, this was the first network with more than one hidden layer. Its role was imposed primarily by the Precepton network. The suggested learning of the network was to localize the error by computing it at the output layer and backpropagating the error to each hidden layer such that weights of connections were being adjusted until the input layer reached (Haykin, 1999).

Multi-layer feedforward networks consist of the input layer, output layer, and at least one hidden layer with feedforward connection. The hidden layers help the network in extracting higher order statistics (Haykin, 1999). Figure 4.7 shows an example of fully connected three-layer feedforward network, referred to as m-s-c (m source neurons, s hidden neurons, and c output neuron).

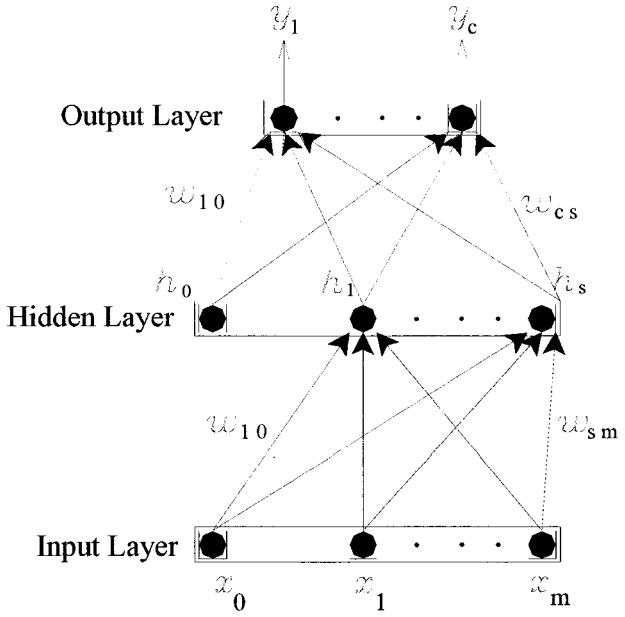

Figure 4.7 Three-Layer Feedforward Neural Network with Structure [m-s-c].

With this architecture, the source neurons in the input layer (i.e., first layer) provide the input vector to the hidden layer (i.e., second layer). The output vector of the hidden layer is then used as input to the third layer (i.e., output layer), which outputs the overall network solution. Recurrent neural networks are similar to the feedforward networks, except that the former have at least one feedback loop. According to Schuch et al. (2002), feedforward networks have better prediction capabilities than recurrent networks. In our prediction model, the feedforward neural network was used. In this case, the output signal at a neuron j (either a hidden neuron or an output node) can be written as:

$$y_j(n) = \varphi(v_j(n)) \tag{4.16}$$

where $v_j(n)$ is the activation potential of neuron j, which is defined by:

$$v_j(n) = \sum_{i=0}^{m} w_{ji}(n) y_i(n) \tag{4.17}$$

where m is the total number of inputs (without the bias) applied to neuron j; $w_{ji}(n)$ represents the weight connecting the output of neuron i to the input of neuron j at iteration n (n^{th} training example); and $y_i(n)$ is the output signal of neuron i (i.e., the input signal of neuron j). It should be clear that if neuron j is in the first hidden layer, $y_i(n) = x_i(n)$, the i^{th} element is in the input vector.

4.7 The learning Process (backpropagation algorithm) of FFNN

As stated above, neural networks solve complex problems through learning (i.e., training), and then generalizing the network outputs for other inputs. Training the neural network is accomplished through iterative adjustments of the free parameters, i.e., the weights and bias, of the network until the optimal values are obtained. There exist various learning algorithms, which are fundamental to the design of neural networks. Of these, the backpropagation-learning algorithm is the most widely used for feedforward neural networks (Schuch et al., 2002), which is discussed here.

As can be seen in Figure 4.8, the backpropagation learning algorithm allows the output signal of a neuron j, $y_j(n)$, to be compared with a desired (target) output, $d_j(n)$. The error signal at the output of neuron j, $e_j(n)$, is defined as:

$$e_j(n) = d_j(n) - y_j(n) \tag{4.18}$$

where n represents n^{th} training example (i.e., n^{th} pattern). The objective of the iterative adjustments is to make $y_i(n)$ as close as possible to $d_i(n)$, which can be achieved by minimizing a cost function (total instantaneous error energy over all neurons in the output layer) defined as:

$$\mathrm{E}(n) = \frac{1}{2}\sum_{j \in C} e_j^2(n) \tag{4.19}$$

where C represents all neurons in the output layer. The weight correction $\Delta w_{ij}(n)$ can be defined according to the Delta rule as (Haykin, 1999):

$$\Delta w_{ji}(n) = -\eta \frac{\partial \mathrm{E}(n)}{\partial w_{ji}(n)} = \eta \delta_j(n) y_i(n) \tag{4.20}$$

where η is the learning rate parameter, and $\delta_j(n)$ is the local gradient defined by:

$$\delta_j(n) = -\eta \frac{\partial \mathrm{E}(n)}{\partial \mathrm{v}_j(n)} = e_j(n)\varphi_j'\left(\mathrm{v}_j(n)\right) \tag{4.21}$$

where $\varphi_j'(\mathrm{v}_j(n)$ is the derivative of the associated activation function. This means that for $\delta_j(n)$ to exist, the activation function must be continuous, which is satisfied by both the sigmoid and hyperbolic tangent functions presented in section 4.3 above.

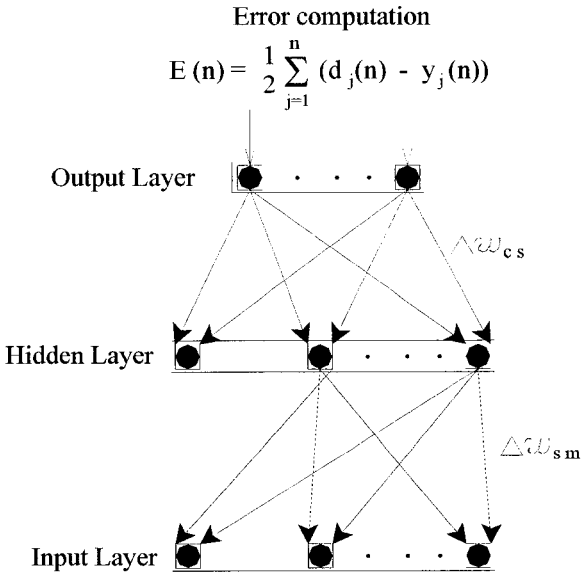

Figure 4.8 Backpropagation of error.

The selection of learning rate parameters η affects the rate of learning of the neural network. The smaller the value of η is, the smaller the changes to the weights and network rate of learning. Smaller η values result in smaller changes to weight in the network, and consequently slower rate of learning. If, on the other hand, the η values are too large, the network may become unstable (i.e., oscillatory) and the algorithm diverges. To overcome this problem, the Extended Dalta-Bar-Delta rule is used, which introduces an additional term to equation (4.20), known as the momentum term (NeuralWare, 2001a; Haykin, 1999), so that the current adjustment becomes:

$$\Delta w_{ji}^{t}(n) = \eta \delta_j(n) y_i(n) + \mu \Delta w_{ji}^{t-1}(n) \tag{4.22}$$

where μ is the momentum term, making learning faster when the learning coefficient is low. Because of its advantages in the local adjustment of learning rates as well as momentum, the EDBD rule was used in our experiments.

Another problem that can occur in backpropagation algorithm is that some processing elements may stop to learn whether their incoming weights are large. In such a case, the summation values become large and the weights become saturated (e.g., value 0 or 1), leading the derivation to 0 and the scaled error to 0. Such saturation can be prevented by adding a small "F'offset" value to the derivative of the activation function. It has been experimentally proved that the value 0.10 is adequate for the sigmoid function and 0.30 for the hyperbolic tangent function (NeuralWare, 2001a).

The weights will be adjusted iteratively by presenting new epochs of training examples to the neural network. Unfortunately, there is no clear-cut criterion for deciding when to stop the training, i.e., to consider whether the backpropagation algorithm has converged (Haykin, 1999). If the training is not stopped at the right point, an over-fitting of the training data (i.e., model does not interpolate well between points) might occur. One approach to this problem is to create a test data set that tests the neural network for its generalization performance (NeuralWare, 2001a).

4.8 Modular Neural Network Structure and Training

Under certain circumstances – for example, when encountering a prediction problem, it may be better to use the modular neural networks. A modular neural network (MNN) was

presented by Jacobs et al. (1991). This network has the capability of dividing a problem into sub-problems and resolving each sub-problem well. It consists of a group of FFNNs, sometimes referred to as "local experts," each having the same architecture. This group of networks competes to learn the various aspects of the problem, which is then controlled by a "gating network". The number of local experts is determined by the number of output neurons of the gating network (NeuralWare, 2001a). Figure 4.9 shows an example of a modular neural network, referred to as m-s-q-1 (m source neurons, s hidden neurons for both local experts and the gating network, q "gating" output neurons, and one network output neuron).

Figure 4.9 represents the architecture of a MNN. Learning is conducted as follows:

1) The input vector is distributed from the input layer to each local expert and the gating network. Each expert is a FFNN. Output of the local experts depends on the feedforward architecture incorporated in the expert.

2) The gating network sends output to an intermediate layer (called gate) where the probabilities sent by the gating network are used to correct the local expert outputs.

3) The final output is that of the local expert with the highest probability; the error is computed according to the formulas in the next section and backpropagated to the local experts and the gating network.

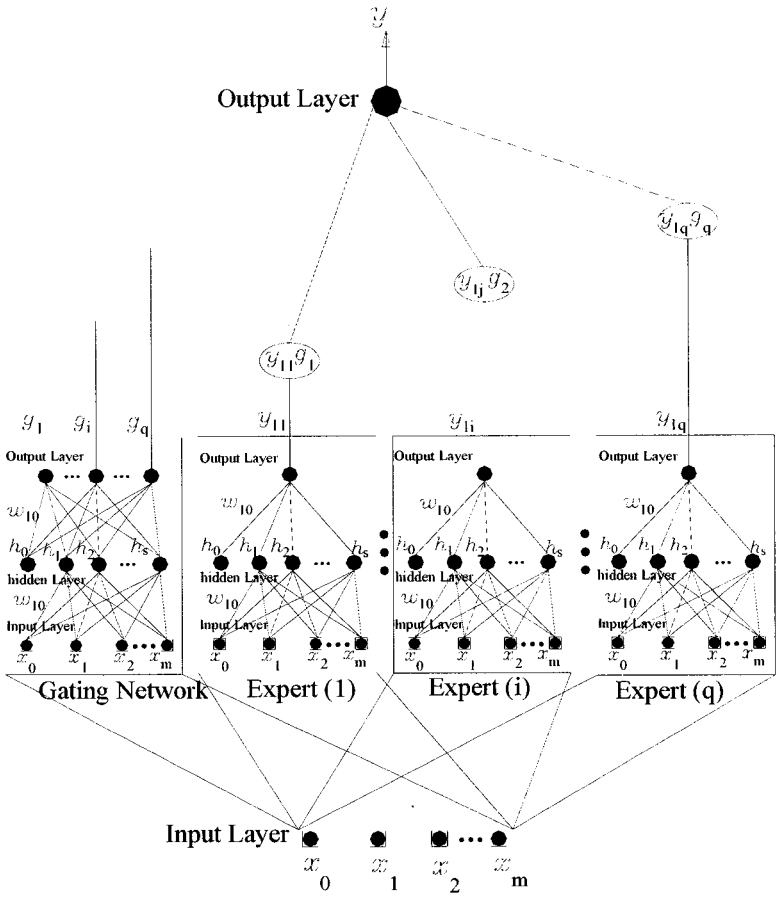

Figure 4.9 A modular neural network with the structure [m-s-q-1].

4.9 Modular Neural Network Computations

As stated above, the network consists of several networks, called "local experts," connected by a gating network that allocates each case into one of the local experts. The output of that local expert is compared with the actual output, and weights are changed locally only for that expert and the gating network. In that way, the gating network "encourages" a particular local expert to specialize in similar cases. The weights of other experts specialize in other cases. The decision of the gating network is made stochastically.

Jacobs et al. (1991) use a stochastic selector, and they compute the error according to the formula:

$$E = \sum_{i \in q} g_i \left\| d - y_i \right\|^2 \tag{4.23}$$

where y_i is the output vector of expert *i*, g_i is the proportional contribution of expert *i* on the combined output vector, and d is the desired output vector. In such a process, each local expert produces the whole output and the aim of one local expert is not directly affected by weights of the other local experts. Although some indirect coupling can occur if the gating network alters the responsibilities from one local expert to another, the sign of the local expert error is still not influenced.

The number of local experts in the network is determined in advance based on the assumed number of subsets or local regions in the input spaces of the sample. Each local expert is a FFNN, and all experts have the same number of input and output units. Local experts, as well as the gating network, receive the same input. Of course, their outputs differ. Output of the gating network is the probability (Jacobs et al., 1991):

$$g_j = \frac{exp(z_j)}{\sum_{i \in q} exp(z_i)} \tag{4.24}$$

where z_j is the total weighted input received by output j of the gating network, and g_j is the probability that the switch selects the output from local experts *j*. This output is

normalized to equal 1. The output of local expert y_i is then corrected by the probability above, and the final output of the network is:

$$y = \sum_{i \in q} y_i g_i \tag{4.25}$$

Unlike FFNN, where the objective function is to minimize a global error function E, MNN tries to maximize the following objective function J:

$$J = ln\left(\sum_{i \in q} g_i \, exp\left(\frac{(d - y_i)^T (d - y_i)}{2} \right) \right) \tag{4.26}$$

Then, the error that is backpropagated for the i^{th} local expert is $\frac{\partial J}{\partial v_i}$, while it is $\frac{\partial J}{\partial z_i}$ for the gating network; where v_i is the input to the i^{th} local expert output node and z_i is the input to the gating network output node.

According to the learning process just described, if an expert gives less error than the weighted average of the error of all experts, its responsibility for that case will be increased, and vise versa. In our experiments, the error is backpropagated and the weights are updated according to EDBD rule.

4.10 Measures of Accuracy

In a range involving a huge number of neural networks, it is extremely difficult to find which types of neural networks are suitable for predicting ice conditions. To evaluate the performance of different types of networks, two statistical indicators were used: Common Mean Correlation Coefficient (CORR), and Normalized Root Mean Square (NRMS) Error (NeuralWare, 2001a).

Each of the performance measures represents a precise method of measuring how well a model performs. No one measure can tell how well one model fares against another; instead, all of these two numbers should generally be considered together. The Common Mean Correlation Coefficient in equation 4.27 shows how well trends, i.e., bumps and valleys, were picked up (NeuralWare, 2001a). The Correlation Coefficient is a number ranging from -1 to 1.

$$CORR = \frac{\sum_{i=1}^{N}(d_i - \bar{d})(y_i - \bar{y})}{\sqrt{\sum_{i=1}^{N}(d_i - \bar{d})^2 \sum_{i=1}^{N}(y_i - \bar{d})^2}} \tag{4.27}$$

where $\bar{d}$ and $\bar{y}$ are the means of the actual and predicted values, respectively. These values can be represented as:

$$\bar{d} = \frac{1}{N}\sum_{i=1}^{N} d_i \tag{4.28}$$

$$\bar{y} = \frac{1}{N}\sum_{i=1}^{N} y_i \tag{4.29}$$

If the model predicts bumps and valleys perfectly, then the corresponding Correlation Coefficient will be 1.

The Normalized Root Mean Square (NRMS) Error in equation 4.30 is a method to compare the mean of a series with the predicted values. If the NRMS is greater than 1, then the predictions are worse than the series mean; if the NRMS is less than 1, then the forecasts are better than the series mean (NeuralWare, 2001a). The NRMS is a measure widely used in many research studies to evaluate how well a neural network performs.

$$NRMS = \sqrt{\frac{\sum_{i=1}^{N}(y_i - d_i)^2}{\sum_{i=1}^{N}(d_i - \bar{d})^2}} \tag{4.30}$$

Finally, It should be noted that NRMS and CORR measures provide useable statistics to verify model predictions, and they are applicable to a large number of analyses, prediction elements, and model types.

4.11 Performance Measure

The performance of the network can be measured based on the percentage of correct prediction – the ratio of the correct network output values and the actual values at the various points in the test area.

The prediction is considered as correct if:

$$-0.50 < (d_i - y_i) < 0.50 \tag{4-31}$$

The prediction is considered as false if:

$$-0.50 \geq (d_i - y_i) \quad \text{or} \quad 0.50 \leq (d_i - y_i) \tag{4-32}$$

5 RESULTS AND DISCUSSION

This chapter describes how to apply neural networks to the prediction of total ice concentration. First, a brief description of the used package is provided, and then I describe the study area of interest in the Gulf of St. Lawrence. Next I demonstrate the use of two different artificial neural network models in identifying the major independent variables to optimize the model performance. In addition, the developed neural network-based model is compared with the traditional model – the coupled ice-ocean model.

5.1 Software Review

The structure of the neural network model used in this investigation was built using the *NeuralWorks Professional/II plus* (NeuralWare, 2001b). *NeuralWorks Professional/II* (hereafter NeuralWorks) is based on the artificial neural network algorithms described in the previous chapter. NeuralWorks is a comprehensive development package incorporating many types of neural networks. It provides the capability to train and test a network, monitor progress, debug, customize standard neural network models, and save and implement trained networks.

NeuralWorks contains 22 different architectures or learning algorithms, including Multi-Layer Perceptron (MLP), Self-Organizing Map (SOM), Radial Basis Function (RBF), Modular Neural Network (MNN), Probabilistic Neural Network (PNN), Fuzzy ARTmap, genetic reinforcement, generalized regression, recurrent, and reinforcement networks. The package also includes networks of historical importance such as the Perceptron,

ADALINE, and bi-directional associative memory. There are two add-on packages: User-Defined Neuro-Dynamics that lets the user change any aspect of network architecture or learning algorithm, and Designer Pack that allows the user to create source code of the untrained network so that it can be trained as part of a custom application.

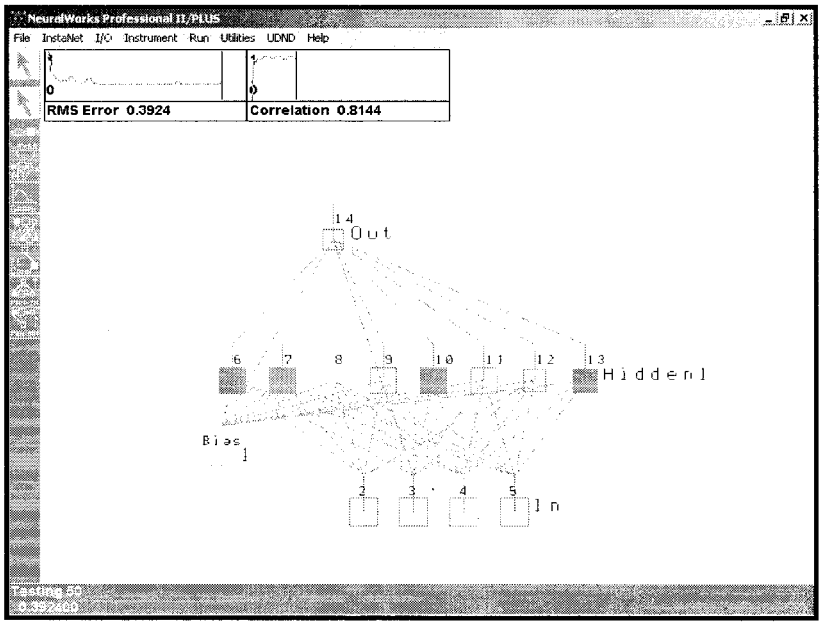

Figure 5.1 The user interface in NeuralWorks Professional II/Plus package.

The interface in NeuralWorks (Figure 5.1) shows the Processing Elements (PEs) and connection weights for the network architecture. PEs are color coded and sized according to their value during training, and the connection weights are color coded according to values that enable the user to quickly see the state of the network. The user specifies the number of input, output and hidden PEs, selects the cost function, activation function, starting values for the learning rate and momentum. The user further decides whether on-line or batch learning is to be used and whether the training set should be randomized,

and selects how the input data scaling should be performed. The user can also set up a learn/recall schedule that allows the learning rate and momentum values for each layer to change over time. The data input and output is from and to an ASCII text file, which is not always as convenient as using Microsoft Excel.

Visual reinforcement of the training process is supported by a variety of graphical instruments, allowing a user to quickly monitor progress in training. For example, as seen in Figure 5.1, the root mean square error (RMS) graph shows the changes in the RMS error as training progresses. A number of other graphical instruments are used with specific network paradigms, which can be attached to any node or layer of nodes to allow monitoring of the intermediate results. The numeric values that produce the graphs can also be saved to ASCII format files for use with other software packages, allowing, for example, the error values to be input to a spreadsheet for further analysis.

5.2 Study Area

As mentioned earlier and as shown in Figure 5.2, a supervised neural network was trained to predict sea ice concentrations at a selected location in the Gulf of St. Lawrence. Canadian Ice Service provided us with grid-point ice conditions for the regional ice charts of the East Coast of Canada. Weekly data series of 200 points within of the Gulf of St. Lawrence were used to validate the ANN models. The data series consisted of the weekly ice concentration throughout 11 years (1987-1998). The total size of the available dataset was 603 records for each data series. The study area was divided into seven sub-

regions (Figure 5.3). The results of the first sub-region are shown and discussed in this chapter; the results of other sub-regions are recorded in Appendix II.

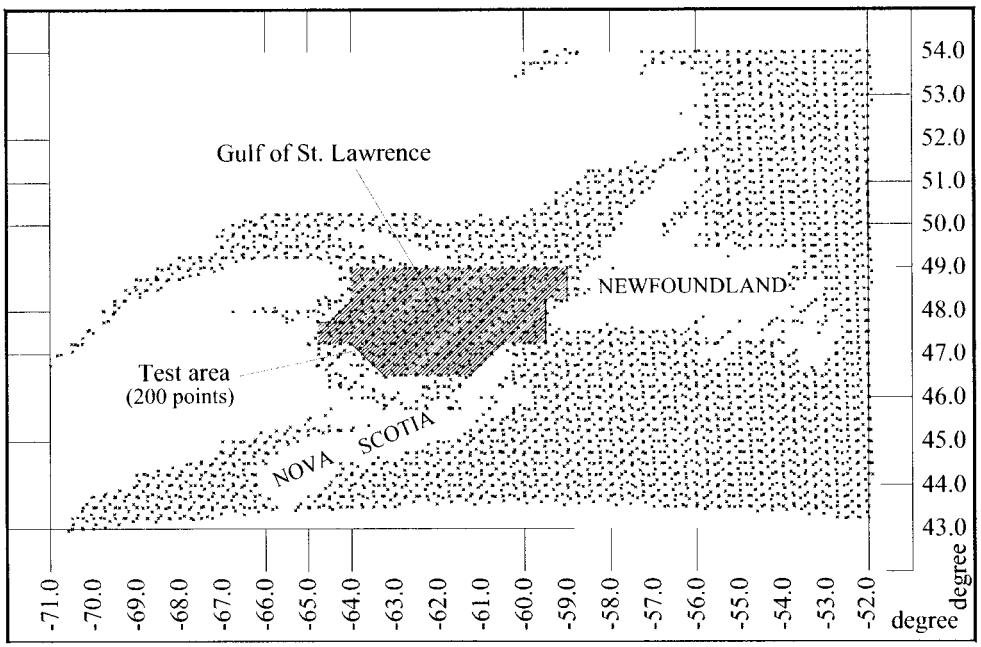

Figure 5.2 Study area (200 points).

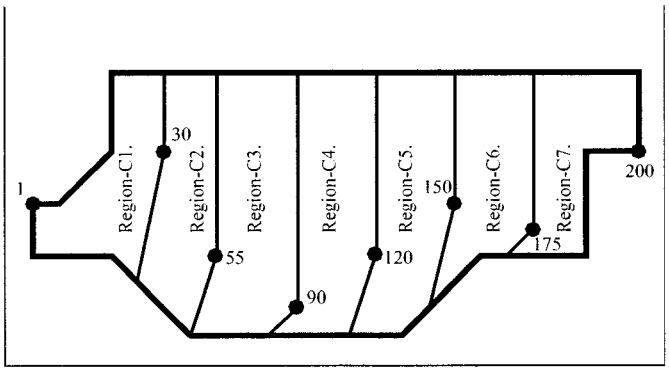

Figure 5.3 Regions locations.

5.3 Modeling Strategies of Total Ice Concentration

In this work neural networks were developed for modeling and predicting of ice concentration. In developing an efficient neural-network model, it is essential to determine what the neural network is expected to do; for the model to improve prediction performance, I need to perform extensive data analysis and preparation prior to training the neural network. Two approaches were considered for ice concentration modeling: the batch method and the sequential method. Figure 5.4 illustrates the strategies used for developing a neural network model based on the two proposed methods.

Initially the batch method was tested, in which the time (year and week numbers) is the only input to the network, as suggested by El-Rabbany et al. (2002). Then the sequential method, which was suggested by El-Diasty et al. (2002) and El-Rabbany and El-Diasty (2003), was used. In this approach, the immediate past values of the ice concentration are used as input to the network, while future values of the ice concentration are used as the desired (i.e., actual) output. Both Feedforward Neural Network (FFNN) and Modular Neural Network (MNN) structures were tested, using the same datasets, for both models. Finally, the best ANN model was selected based on the lowest root mean square (RMS) and highest correlation coefficient (CORR), discussed in a previous chapter.

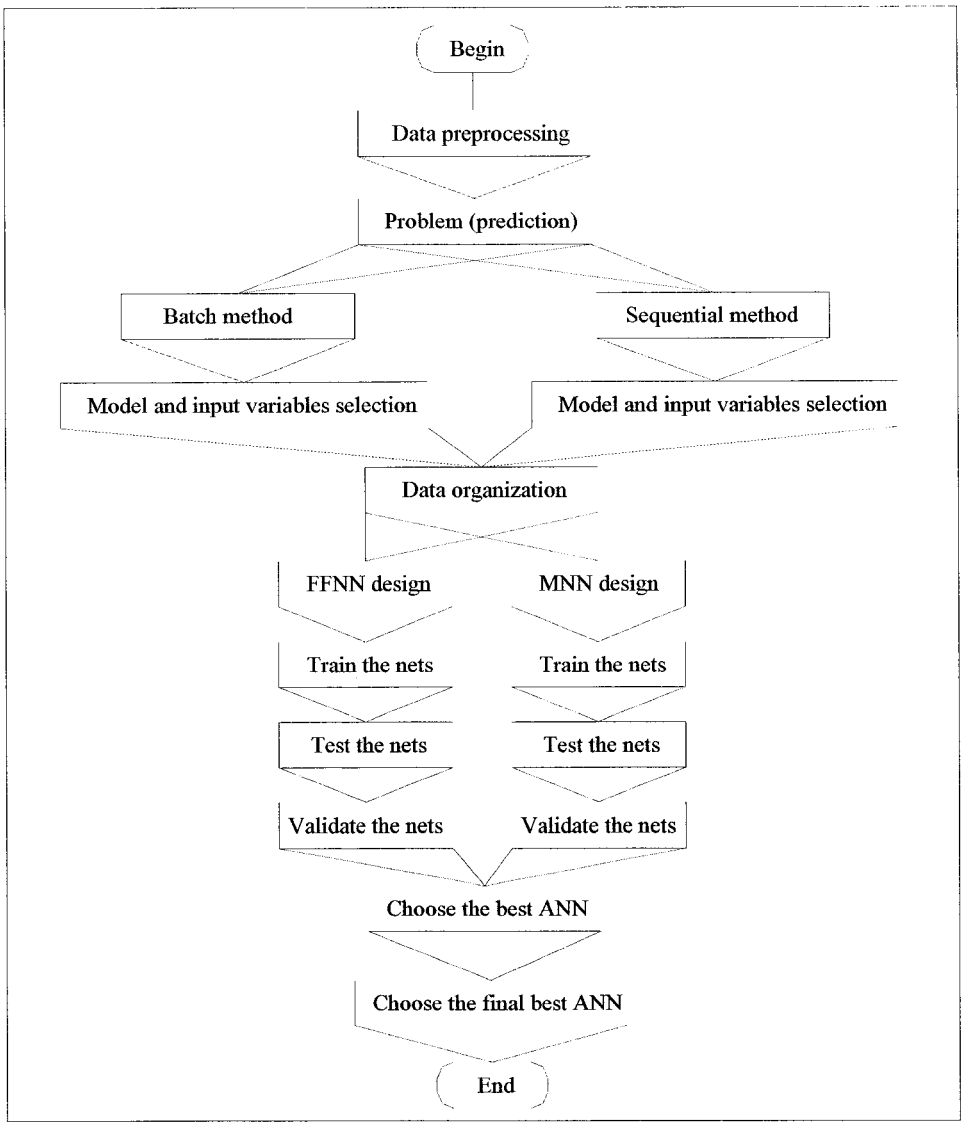

Figure 5.4 Strategies for selecting the best ANN.

5.4 Results and Discussion of Batch Method

The batch method was suggested by El-Rabbany et al. (2002). In this approach, the time variables are used as the only input to the network, and the ice concentration is assigned

as the desired output. In other words, the input layer consists of two neurons – the year and week number – and the output layer consists of only one neuron.

As seen in Figure 5.5, for each test point in the Gulf of St. Lawrence the size of the available dataset a total of 603 different patterns were created. In the pre-processing stage, the dataset was divided into three subsets: testing, training, and validation (Figure 5.5). The first 50 patterns were assigned to the testing subset and the last 50 patterns were assigned to the validation subset. The training subset was selected to represent the middle portion of the dataset, i.e., 503 patterns. The training was stopped based on testing the "generalization" performance of the neural network using the testing subset. After training and testing the network, the model was generalized to predict the last 50 patterns of the dataset and compared the results with the actual values of the ice concentration.

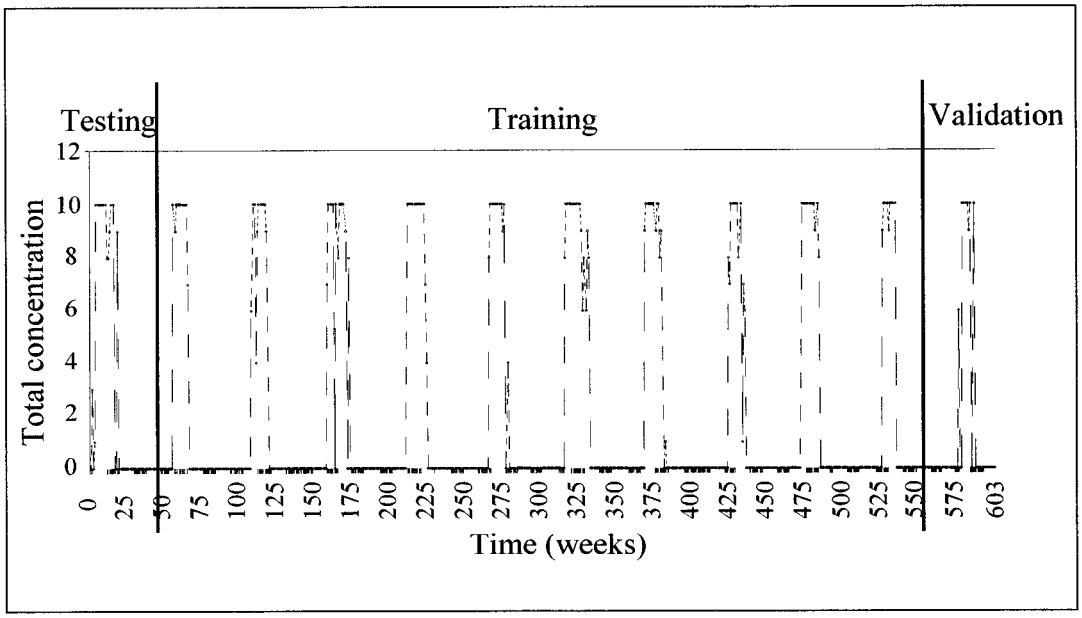

Figure 5.5 Selection of testing, training and validation data subsets.

Two artificial neural network structures, FFNN and MNN, were constructed using NeuralWorks. The networks are similar in design, the main difference between them being the network structure. In Figure 5.6, the FFNN structure [2-s-1] consists of "2" input neurons (time variables), "s" hidden neurons (unknown variables), and "1" output neuron (predicted ice concentration). Figure 5.7 shows the MNN structure [2-s-q-1]; it represents "2" source neurons, "s" hidden neurons for both the local experts and the gating network (unknown variable), "q" gating output neurons (unknown variable), and "1" network output neurons.

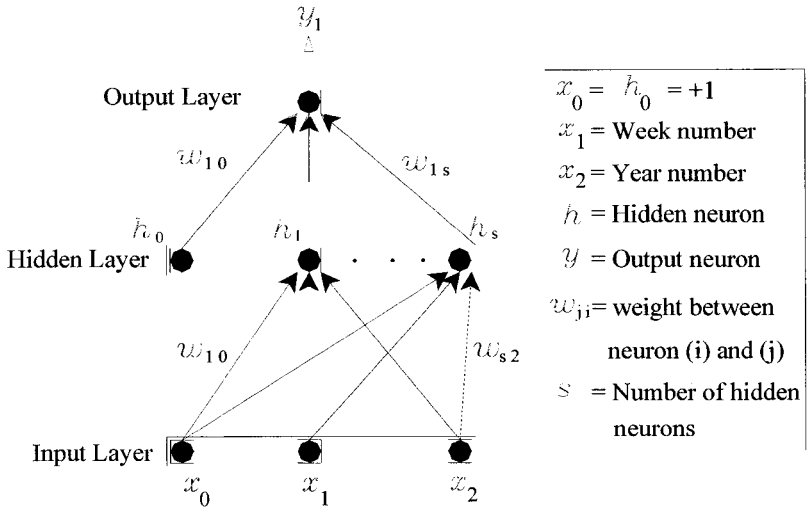

Figure 5.6 FFNN structure of batch model [2-s-1].

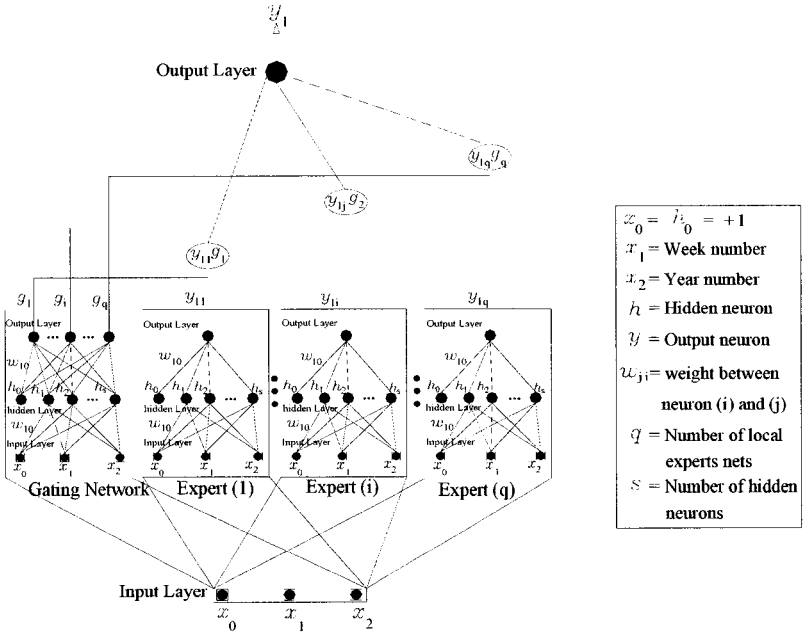

Figure 5.7 MNN structure of batch model [2-s-q-1].

Consider the prediction network for a single point without abrupt changes in the values of the ice concentration over a short time period. In the processing stage of both FFNN and MNN, I used the backpropagation learning algorithm, the Extended-Delta-Bar-Delta (EDBD) learning rule, the hyperbolic tangent transfer function, a learning rate of 0.3, and a momentum coefficient of 0.4. Based on the size of the available dataset, a total 603 different patterns were created.

Several tests were conducted to optimize the structure of the neural network. As specified in Table 5.1, it was concluded that the optimal structure of feedforward neural network was [2-8-1], and of the modular neural network was [2-8-5-1]; meaning it has the lowest root-mean-square (RMS) error. Table 5.1 and

Figure 5.8 illustrate the batch model network results for both FFNN and MNN. The results show that the MNN network performs better than the FFNN, a conclusion that agrees with that of El-Rabbany et al. (2002) concluded.

Table 5.1 Results of batch model for a single point (without abrupt changes).

Sympols	Without abrupt changes	
	FFNN	MNN
N (Total set)	603	603
N_S (Testing set)	50	50
N_T (Training set)	503	503
N_V (Validation set)	50	50
Strucure	[2-8-1]	[2-8-5-1]
RMS (Testing)	0.1530	0.2410
RMS (Training)	0.2318	0.2204
RMS (Validation)	0.2744	02118
CORR (Testing)	0.9696	0.9323
CORR (Training)	0.9307	0.9377
CORR (Validation)	0.8983	0.9438

Several tests were conducted to optimize the structure of the neural network. As specified in Table 5.1, it was concluded that the optimal structure of feedforward neural network was [2-8-1], and of the modular neural network was [2-8-5-1]; meaning it has the lowest root-mean-square (RMS) error. Table 5.1 and

Figure 5.8 illustrate the batch model network results for both FFNN and MNN. The results show that the MNN network performs better than the FFNN, a conclusion that agrees with that of El-Rabbany et al. (2002) concluded.

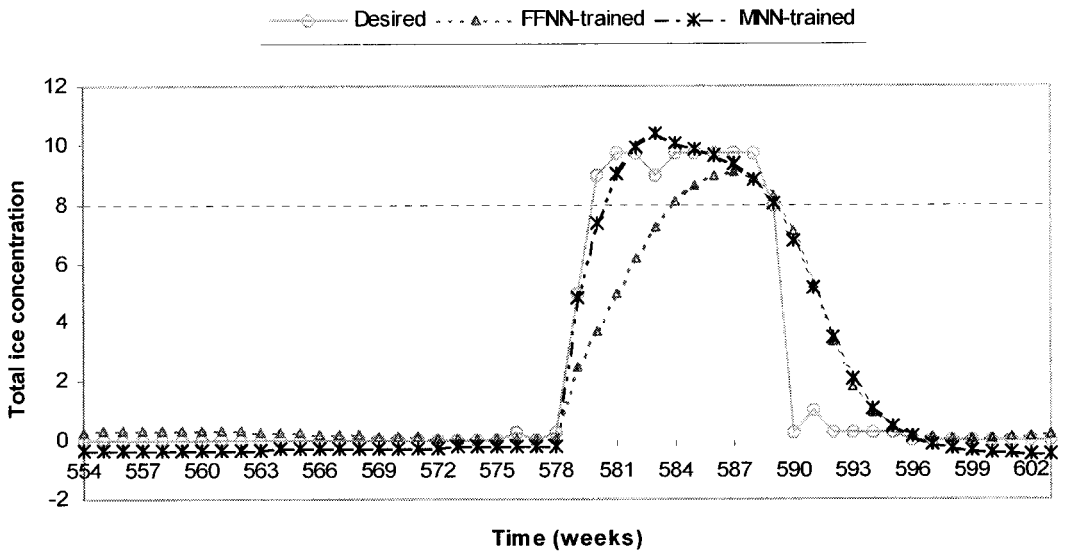

Figure 5.8 Actual versus predicted ice concentration values of batch model for the year 1998 – a single point (without abrupt change).

Table 5.2 Results of batch model for a single point (with abrupt changes).

Sympols	With abrupt changes	
	FFNN	MNN
N (Total set)	603	603
N_S (Testing set)	50	50
N_T (Training set)	503	503
N_V (Validation set)	50	50
Strucure	[2-10-1]	[2-8-5-1]
RMS (Testing)	0.2735	0.2750
RMS (Training)	0.2762	0.2550
RMS (Validation)	0.2827	0.2640
CORR (Testing)	0.9088	0.9079
CORR (Training)	0.9007	0.9158
CORR (Validation)	0.8880	0.9058

Consider the prediction network for a single point with abrupt changes in the values of the ice concentration over short time periods. In the processing stage of both FFNN and MNN, I used the same design aspects (mentioned above) as were used throughout the work. Several tests were conducted to optimize the structure of the neural network. It was concluded that the optimal structure of feedforward neural network was [2-10-1] and of the modular neural network was [2-8-5-1] as specified in Table 5.2.

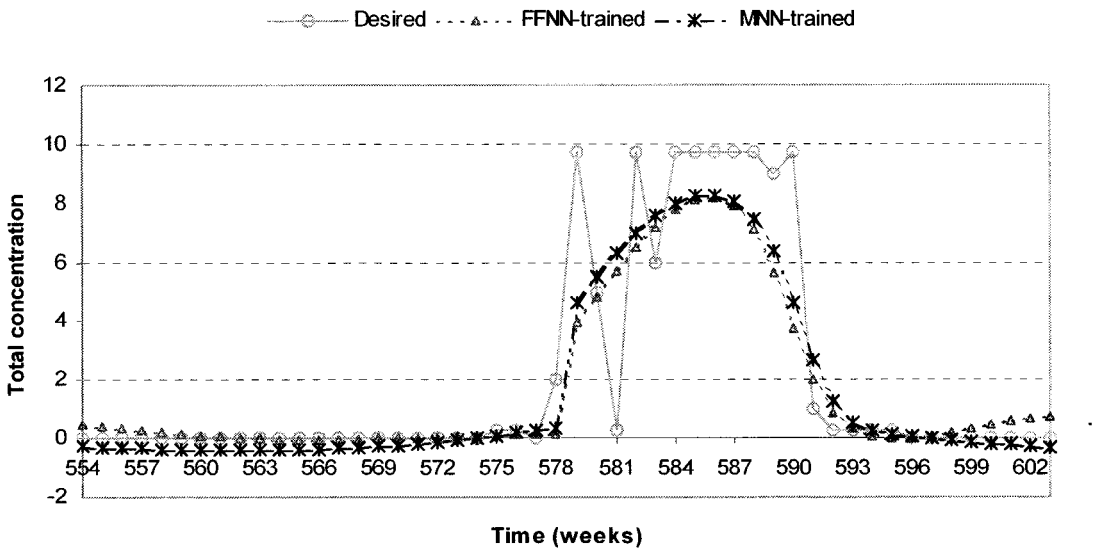

Figure 5.9 Actual versus predicted ice concentration values of batch model for the year 1998– a single point (with abrupt changes).

Table 5.2 and

Figure 5.9 illustrate the batch model network results for both FFNN and MNN, showing that the performances of both networks were almost the same. However, although the trained network represented the training dataset reasonably well, the network prediction was rather poor: The average value of the normalized RMS exceeded 0.25 because of the abrupt changes in the values of the ice concentration. I therefore followed another

approach – the sequential approach, proposed by El-Diasty et al. (2002) and El-Rabbany and El-Diasty (2003).

5.5 Results and Discussion of Sequential Method

In this approach, the immediate past values of the ice concentration are used as input to the network, while future values of the ice concentration are used as the desired (i.e., actual) output. In the subsequent epochs, the training patterns are time-shifted as shown in Figure 5.10. Based on the size of the available dataset, a total 599 different patterns were created.

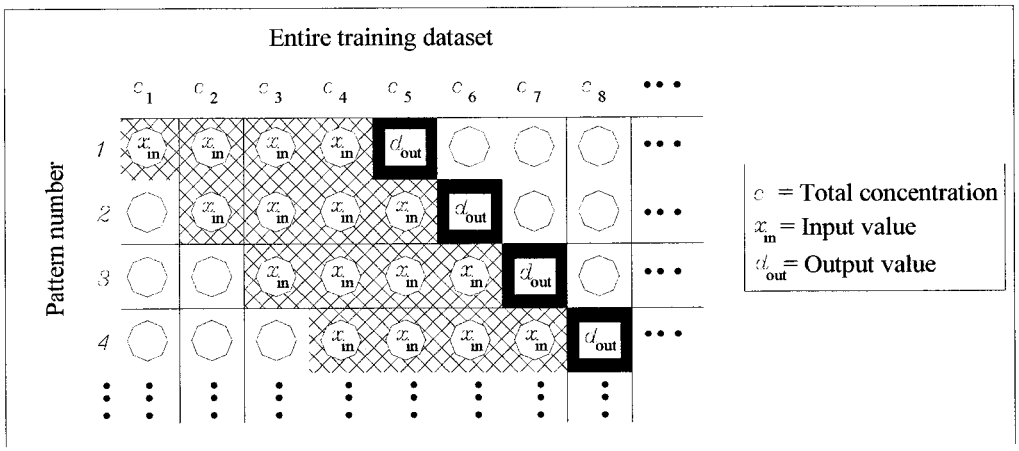

Figure 5.10 Training patterns used in the sequential approach.

The dataset was divided into three subsets: training, testing, and validation (Figure 5.11). The first 50 patterns were assigned to the testing subset, while the last 50 patterns were assigned to the validation subset. The training subset was selected to represent the middle portion of the dataset, i.e., 499 patterns. The training was stopped based on testing the generalization performance of the neural network using the testing subset. After training

and testing the network, the model was generalized to predict ahead the last 50 patterns of the dataset and compared the results with the actual values of the ice concentration. This was done in a sequential manner to emulate the real-time condition.

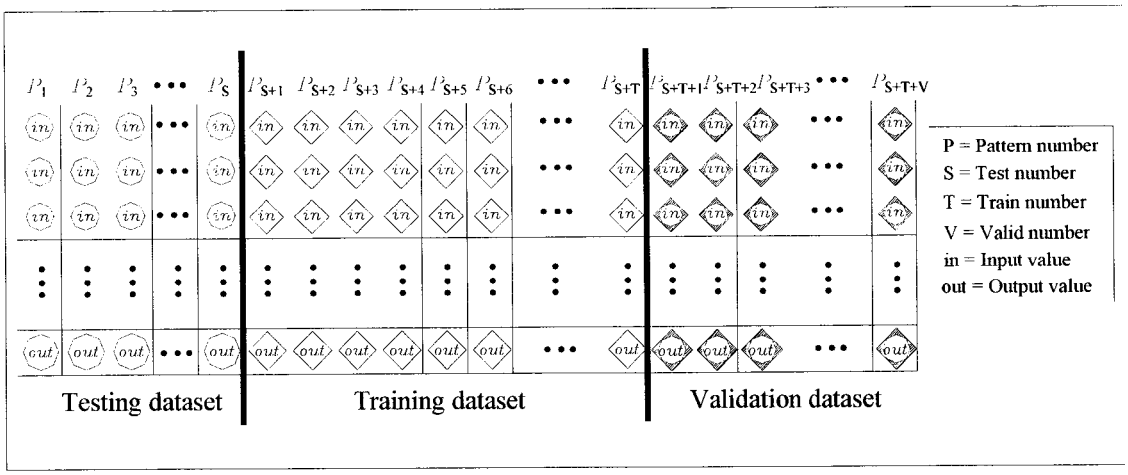

Figure 5.11 Selection of testing, training and validation data subsets.

This method was applied in two cases. The first case is a single-point modeling, in which the ANN was established based on the entire dataset for the records of one point only. The second case is regional modeling, in which the ANN was constructed based on the entire datasets for the records of a number of points in the Gulf of St. Lawrence.

5.5.1 Single-Point Modeling in Sequential Method

The two artificial neural network structures, FFNN and MNN, were built using NeuralWorks. As shown in Figure 5.12, the FFNN structure [4-s-1] consists of "4" input neurons (past values of ice concentration), "s" hidden neurons (unknown variable), and "1" output neuron (predicted ice concentration). Figure 5.13 shows the MNN structure

[4-s-q-1]. This structure represents "4" source neurons, "s" hidden neurons for both the local experts and the gating network (unknown variable), "q" gating output neurons (unknown variable), and "1" network output neurons.

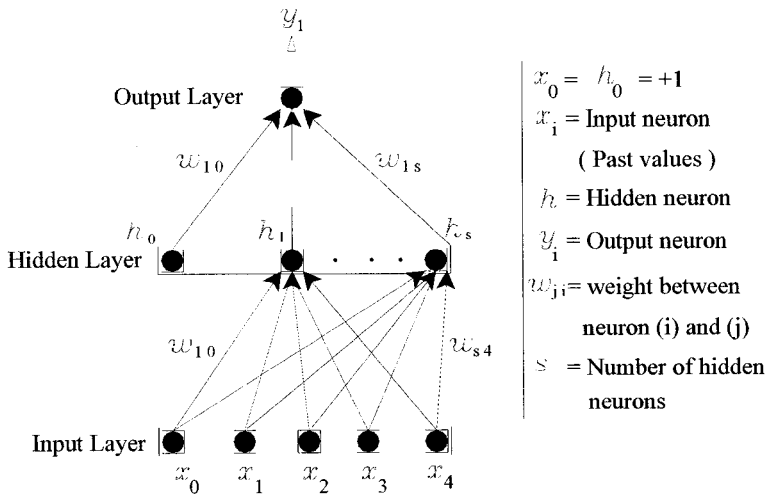

Figure 5.12 FFNN structure of sequential mode [4-s-1] – single-point modeling.

Consider the prediction network for a single point without abrupt changes in the values of the ice concentration over a short time period. In the processing stage of both FFNN and MNN, I used the same design aspects as mentioned above in section 5.4. Several tests were conducted to optimize the structure of the neural network. It was concluded that the optimal structure of the feedforward neural network was [4-15-1] and of the modular neural network was [4-20-5-1], as specified in Table 5.3.

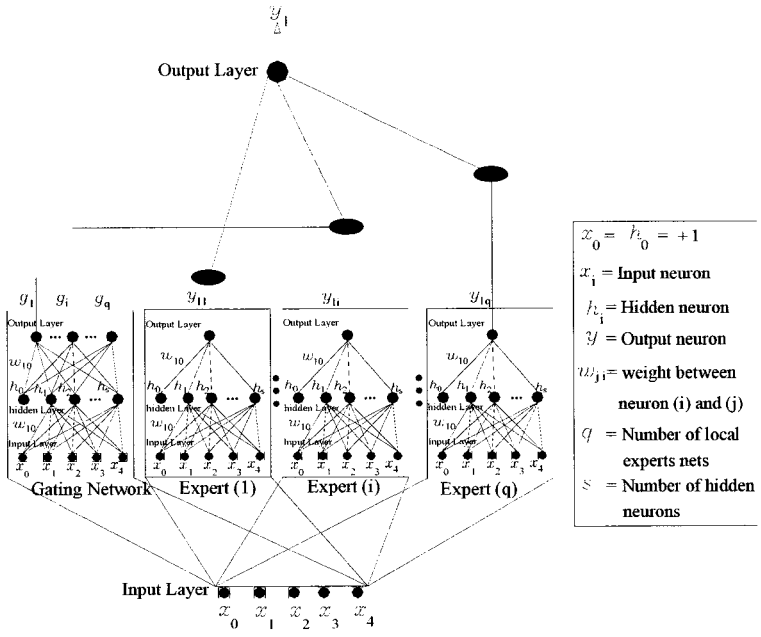

Figure 5.13 MNN structure of sequential mode [4-s-q-1] – single-point modeling.

Table 5.3 Results of sequential model for a single point (without abrupt changes).

Sympols	Without abrupt changes	
	FFNN	MNN
N (Total set)	599	599
N_S (Testing set)	50	50
N_T (Training set)	499	499
N_V (Validation set)	50	50
Strucure	[4-15-1]	[4-20-5-1]
RMS (Testing)	0.2256	0.1971
RMS (Training)	0.2715	0.2644
RMS (Validation)	0.2154	0.2164
CORR (Testing)	0.9324	0.9487
CORR (Training)	0.9041	0.9094
CORR (Validation)	0.9384	0.9378

Table 5.3 and Figure 5.14 illustrate the sequential model network results for both FFNN and MNN. The results show that the performances of FFNN and MNN networks were almost the same.

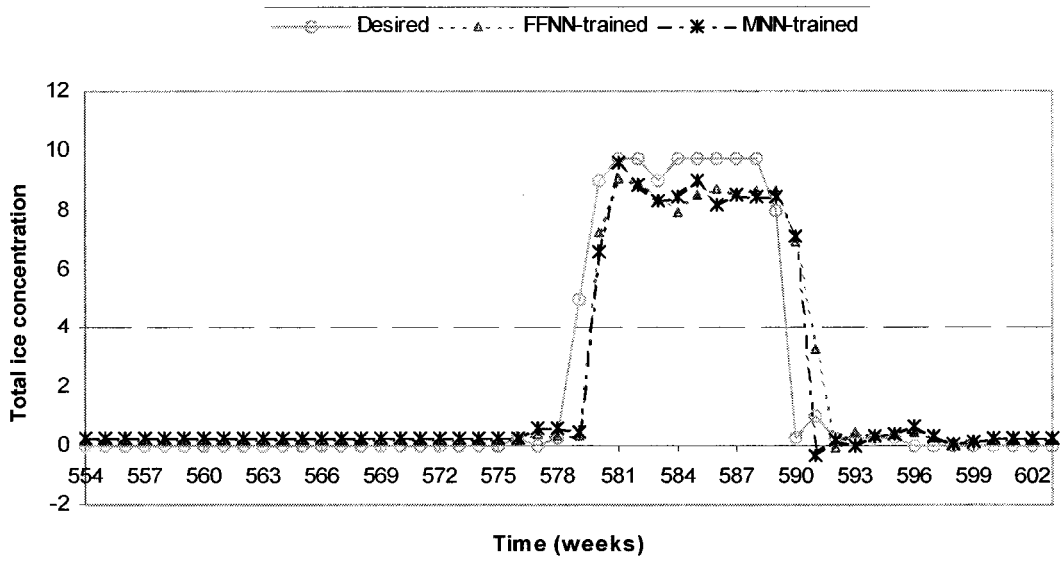

Figure 5.14 Actual versus predicted ice concentration values of sequential model for the year 1998 – a single point (without abrupt changes).

Consider the prediction network for a single point with abrupt changes in the values of ice concentration over a short time period. In the processing stage of both FFNN and MNN, I used the same design aspects as mentioned above in section 5.4. Several tests were conducted to optimize the structure of the neural network. It was concluded that the optimal structure of feedforward neural network was [4-15-1] and of the modular neural network was [4-15-5-1], as specified in Table 5.4.

Table 5.4 and

Figure 5.15 illustrate the sequential model network results for both FFNN and MNN. The results show that the MNN network performs slightly better than the FFNN. However, although the trained network represented the training dataset reasonably well, the network prediction was still rather poor: The value of the normalized RMS exceeded 0.25 due to the abrupt changes in the values of the ice concentration over a short time period. This conclusion agrees with what El-Diasty et al. (2002) and El-Diasty and El-Rabbany (2003a; 2003b) concluded. Therefore, I followed the regional mode of the sequential model, which was proposed by El-Diasty and El-Rabbany (2003a; 2003b).

Table 5.4 Results of sequential model for a single point (with abrupt changes).

Sympols	With abrupt changes	
	FFNN	MNN
N (Total set)	599	599
N_S (Testing set)	50	50
N_T (Training set)	499	499
N_V (Validation set)	50	50
Strucure	[4-15-1]	[4-15-5-1]
RMS (Testing)	0.2033	0.2173
RMS (Training)	0.2963	0.2740
RMS (Validation)	0.3268	0.2677
CORR (Testing)	0.9545	0.9453
CORR (Training)	0.8852	0.9019
CORR (Validation)	0.8488	0.9028

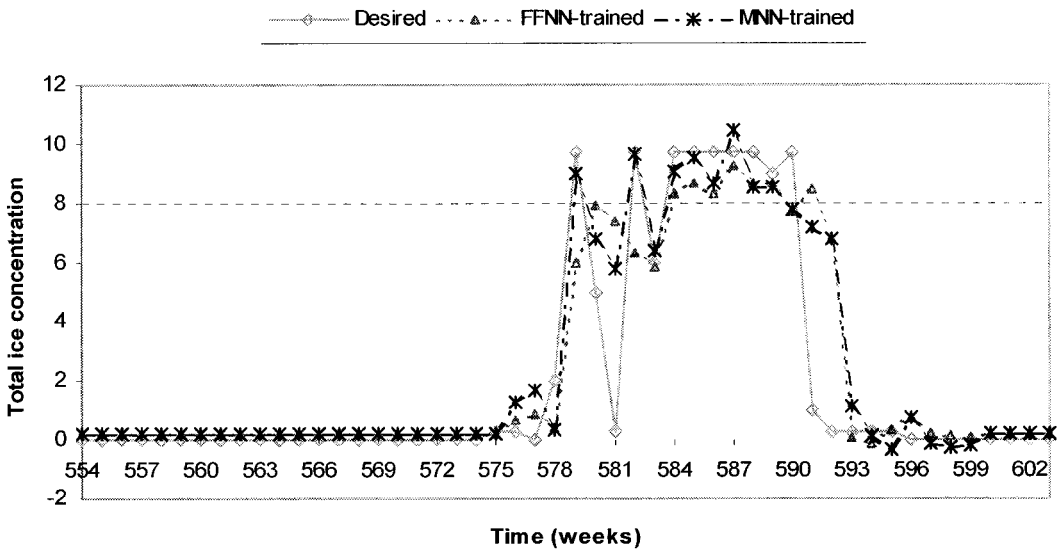

Figure 5.15 Actual versus predicted ice concentration values of sequential model for the year 1998– a single point (with abrupt changes).

5.5.2 Regional Modeling in Sequential Method

In this section I tried to model 200 points in one structure. The two artificial neural network structures, FFNN and MNN, were built using NeuralWorks. As shown in Figure 5.16, the FFNN structure [m-s-c] consists of "m" input neurons (past values of ice concentration, which equal four times the number of points included in the tested region), "s" hidden neurons (unknown variable), and "c" output neuron (predicted ice concentration, which equals the number of points). Figure 5.17 shows the MNN structure [m-s-q-c]; it represents "m" source neurons, "s" hidden neurons for the local experts and the gating network (unknown variable), "q" gating output neurons, and "c" network output neurons.

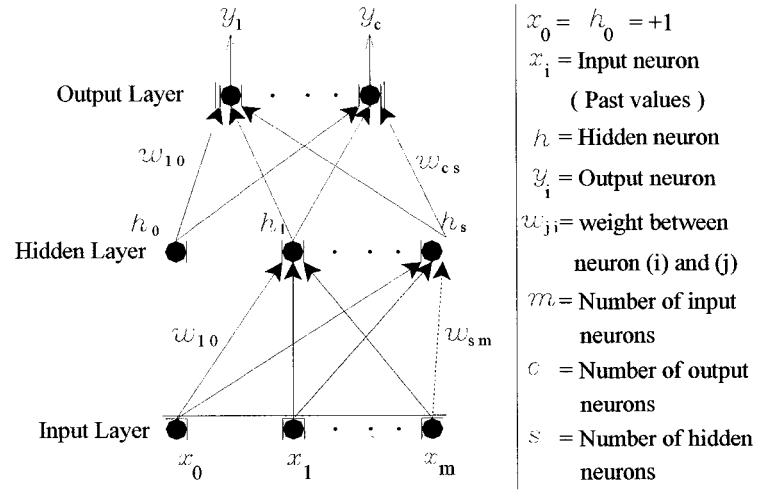

Figure 5.16 FFNN structure of sequential mode [m-s-c] – regional modeling.

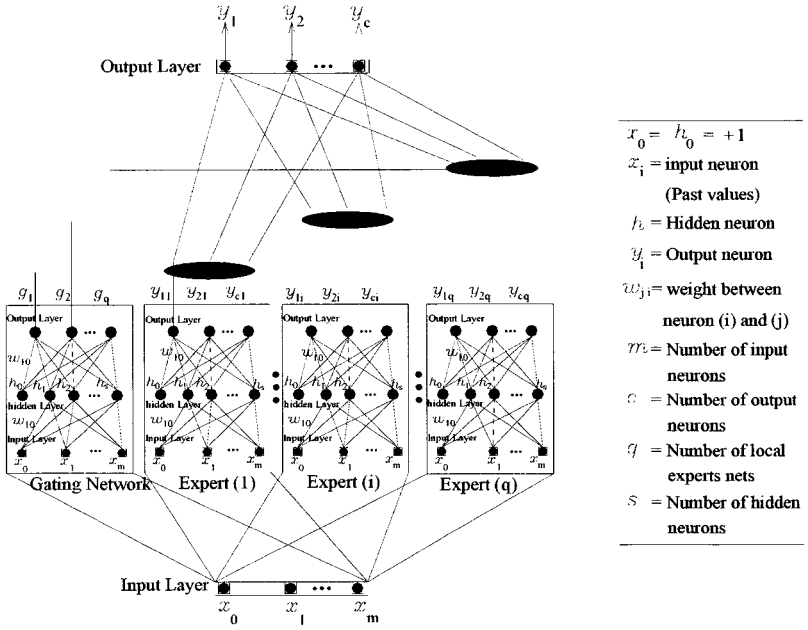

Figure 5.17 MNN structure of sequential mode [m-s-q-c] – regional modeling.

Consider the prediction network for a selected region, which includes data with abrupt changes in the values of ice concentration. In the processing stage of both FFNN and

MNN, I used the same design aspects mentioned above in section 5.4. Several tests were conducted to optimize the optimal number of points included in the tested region and the optimal structure of the neural network. It was concluded that the optimal method to model 200 points was to divide the study area into sub-regions. The optimal number of points and the optimal structure of feedforward neural network and modular of seven regions are specified in Table 5.5.

In this section the results of the first sub-region, namely Region-C.1, are illustrated in Table 5.6, and results of other sub-regions from Region-C.2 to Region-C.7 are recorded in Appendix II. It was concluded that the optimal number of points for Region-C.1 equals 30 points, the optimal structure of feedforward neural network is [120-180-30], and of the modular neural network is [120-60-5-30].

Figure 5.18 and Figure 5.19 illustrate the sequential model network results for both FFNN and MNN, respectively. It is shown for a randomly selected point without abrupt changes with in Region-C.1 that the MNN network performs significantly better than the FFNN.

Figure 5.20 and Figure 5.21 illustrate the sequential model network results for both FFNN and MNN, respectively, when a point with abrupt changes is considered. The results show that the MNN network performs significantly better than the FFNN.

Table 5.5 Summary results of sequential model for all sub-regions.

Sub-regions	Optimal number	FFNN structure	MNN structure
Region-C.1	30	[120-180-30]	[120-60-5-30]
Region-C.2	25	[100-150-25]	[100-150-5-25]
Region-C.3	35	[140-210-35]	[140-280-5-35]
Region-C.4	30	[120-120-30]	[120-120-5-30]
Region-C.5	30	[120-270-30]	[120-270-5-30]
Region-C.6	25	[100-150-25]	[100-100-5-25]
Region-C.7	25	[100-150-25]	[100-100-5-25]

Table 5.6 Results of sequential model for the Region-C.1.

Sympols	Region-C.1 (30 points) FFNN	MNN
N (Total set)	599	599
N_S (Testing set)	50	50
N_T (Training set)	499	499
N_V (Validation set)	50	50
Strucure	[120-180-30]	[120-60-5-30]
RMS (Testing)	0.124	0.089
RMS (Training)	0.143	0.095
RMS (Validation)	0.163	0.144
CORR (Testing)	0.978	0.989
CORR (Training)	0.965	0.982
CORR (Validation)	0.958	0.967

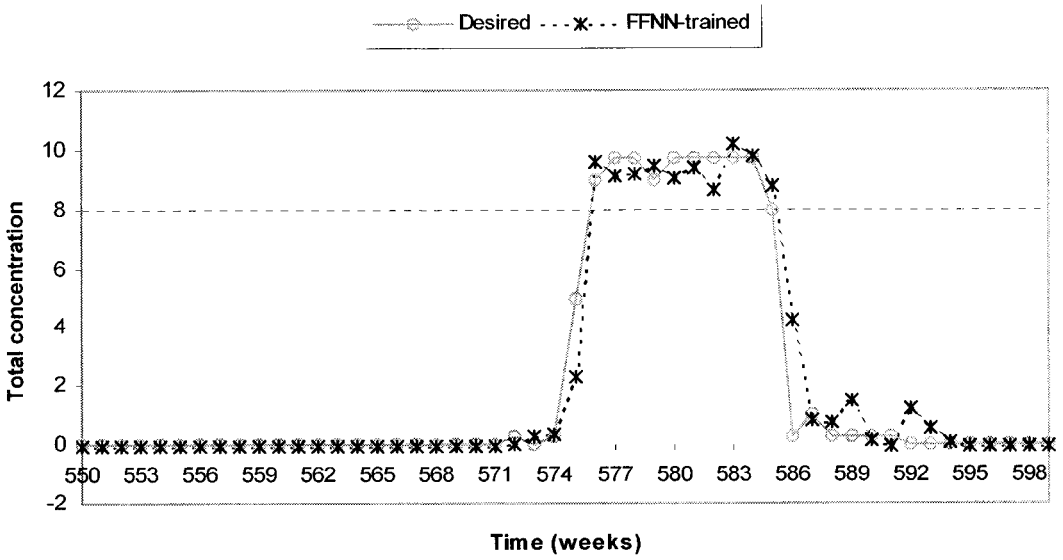

Figure 5.18 Actual versus predicted ice concentration values from FFNN sequential model for the year 1998 (regional modeling of Region-C.1) – without abrupt changes.

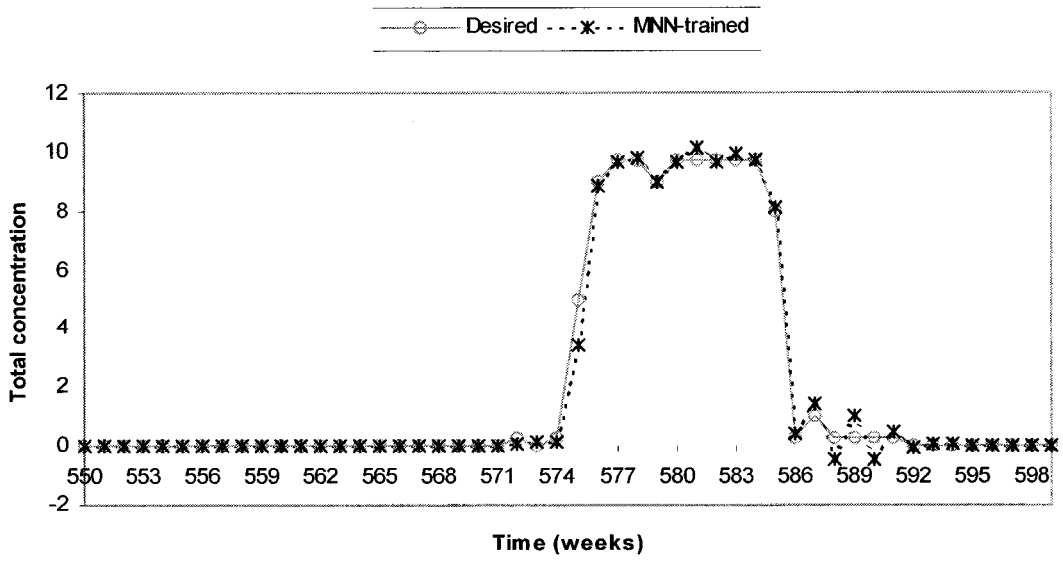

Figure 5.19 Actual versus predicted ice concentration values from MNN sequential model for the year 1998 (regional modeling of Region-C.1)– without abrupt changes.

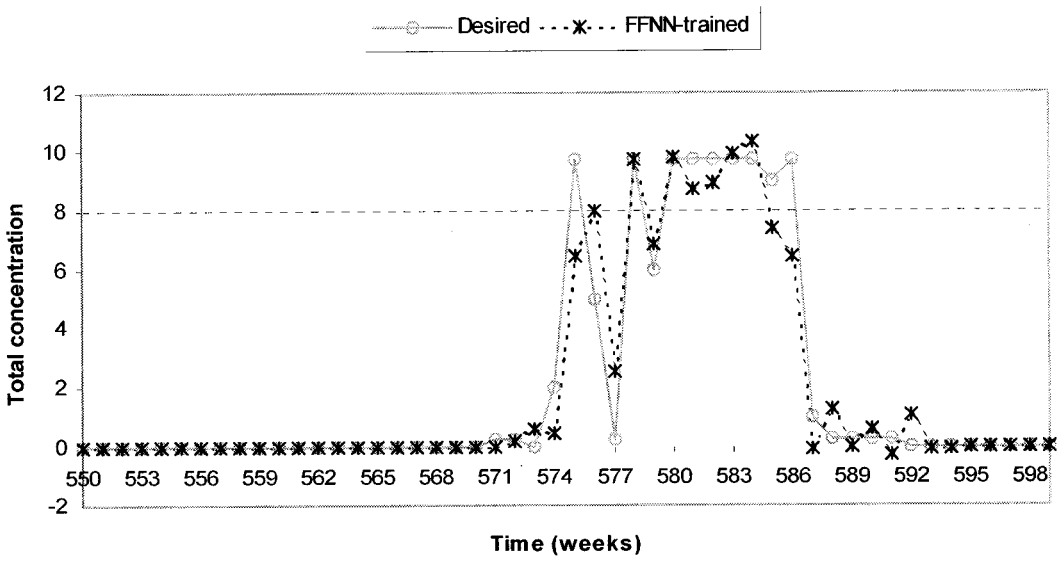

Figure 5.20 Actual versus predicted ice concentration values from FFNN sequential model for the year 1998 (regional modeling of Region-C.1) – with abrupt changes.

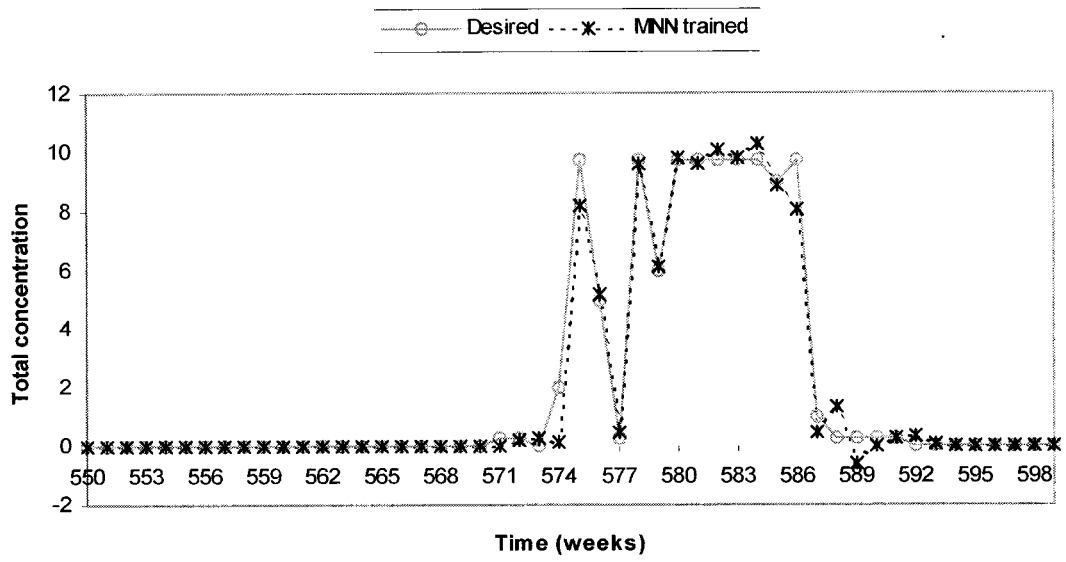

Figure 5.21 Actual versus predicted ice concentration values from MNN sequential model for the year 1998 (regional modeling of Region-C1) – with abrupt changes.

5.6 Performance of the Best ANN Model

Two approaches were considered in predicting ice concentration in this investigation, namely the batch and sequential methods. It has been shown that both approaches are capable of modeling sea ice concentrations. However, a sequential model that uses the modular neural network structure to model the ice concentrations over a region gave the best performance results – the average value of the normalized RMS was 0.098.

Table 5.7 The performance of the best ANN model for all sub-regions (sequential method).

Sub-regions	Optimal number	MNN structure	Average performance (%)	Training period (hh:mm:ss)
Region-C.1	30	[120-60-5-30]	0.911	(00:56:23)
Region-C.2	25	[100-150-5-25]	0.902	(01:22:11)
Region-C.3	35	[140-280-5-35]	0.908	(02:30:41)
Region-C.4	30	[120-120-5-30]	0.900	(01:51:35)
Region-C.5	30	[120-270-5-30]	0.886	(02:26:45)
Region-C.6	25	[100-100-5-25]	0.929	(01:01:01)
Region-C.7	25	[100-100-5-25]	0.902	(01:01:01)
Overall	- - -		0.905	- - -

The performance of the network was measured based on the percentage of correct prediction – the ratio of the correct network output values and the actual values at the various points in the test area. The network solutions show that the prediction performance of the neural network varied between 84% (42 out of 50 were correct) and

98% (49 out of 50 were correct). Table 5.7 summarizes the average overall performance of the network over the entire test area (200 points) was 90.5%.

5.7 Comparison of ANN Model with Coupled Ice-Ocean Model

A performance comparison was made between the developed neural network model and coupled ice-ocean model for ice concentration prediction. For that purpose, the accuracy of a model simulation throughout 1997-98 was checked against available data on ice concentration. It was shown in this study that, despite the absence of the environmental data, the average overall performance of the network over the entire test area (200 points) was 90.5%, while Saucier et al., (2000) concluded that the average performance of the coupled ice-ocean model was undervalued by 20% (80% accuracy). This result shows that with regional modeling, the developed neural network model has the capability to predict the ice concentration values more accurately; even when environmental data are not available.

6 CONCLUSIONS AND RECOMMENDATIONS

6.1 Conclusions

A batch and a sequential neural network-based model for ice concentration prediction were developed in this research. In batch model, comparison of feedforward neural network against modular network was done. It is shown that, batch modular neural network structure gave the best performance (i.e., the minimum RMS), and therefore was used in comparison with sequential approach. In Sequential modeling, single-point and regional modeling were investigated. In both cases, comparison of feedforward neural network against modular network was done. It has been shown that both approaches are capable of modeling sea ice concentrations. However, a sequential model that uses the modular neural network structure to model the ice concentrations over a region gave the best performance results – the average value of the normalized RMS was 0.098.

The neural network results on batch and sequential models showed that the regional sequential is significantly better than the batch model. The regional sequential modular neural network structure gave the best performance results and therefore was used in predicting the ice concentration values at a selected test area within the Gulf of St. Lawrence. It is shown that, despite the absence of the environmental data, the prediction performance of the neural network varied between 84% and 98%. The average overall performance of the network over the entire test area of the 200 points was 90.5%.

The best performed neural network-based model for regional modeling and prediction of sea ice concentration was a model that uses: (1) initial number of points of 25; (2) the sequential method for input variables with initial window size of 4; (3) modular neural network structure with an architecture consisting of half of input nodes in hidden layer and 5 expert networks; (4) a hyperbolic tangent transfer function; and (5) initial values of 0.3 and 0.4 for the learning rate and the momentum, respectively.

A performance comparison was made between the developed neural network model and the coupled ice-ocean model for ice concentration prediction. The accuracy of a model simulation for 1997-98 was checked against available data on ice concentration for that purpose. It is shown that, despite the absence of the environmental data, the average overall performance of the network over the entire test area (200 points) was 90.5%, while Saucier et al. (2000) concluded that the average performance of the coupled ice-ocean model was 80%. This finding shows that the developed neural network model has the capability to precisely predict the ice concentration values in a sequential manner, even when environmental data are not available.

6.2 Recommended Future Works

As illustrated in third chapter, changes in environmental conditions such as temperature and salinity are of major importance as they directly influence the ice formulation. To further enhance the prediction capability, a future version of the model should include environmental data and other ice parameters, e.g., the partial ice concentrations and the stages of development of the ice types.

A hybrid model, which integrates artificial neural network and wavelet method, should be tested for predicting total ice concentration.

REFERENCES

Asmus, K. W., A. Koonar, S. MacDonald (1996). "Ice-Vu: an Integrated Data Communications and Image Analysis System." Satellite Systems for Mobile Communications and Navigation, Fifth International Conference, 13-15 May, pp. 191-194.

Attema, E. P. W., G. Duchossois, G. Kohlhammer (1998). "ERS-1/2 SAR Land Applications: Overview and Main Results." International IEEE, Geoscience and Remote Sensing Symposium Proceedings, IGARSS '98, 6-10 July, Vol. 4, pp. 1796-1798.

Backhaus, J. O. (1983). "A Semi-implicit Scheme for the Shallow Water Equations for Application to Shelf Sea Modeling." Continental Shelf Research, Vol. 2, pp. 234-254.

Backhaus, J. O. (1985). "A Three-dimensional Model for the Simulation of Shelf-sea Dynamics." Deutsche Hydrographische Zeitschrift, Vol. 38, pp. 165-187.

Bertoia, C., and M. Manore (2001). "SAR in Ice Operations: the NIC and CIS Experience". Presentation at U.S. Government SAR Users Symposium, Canadian Embassy, Washington DC, March 28-29.

Bishop, C. M. (1995). *Neural Networks for Pattern Recognition.* Oxford University Press.

Canadian Centre for Remote Sensing (2003). "Satellites Received at CCRS", http://www.ccrs.nrcan.gc.ca/ccrs/data/satsens/sats/satlist_e.html, Accessed August 2, 2003.

Canadian Ice Service (2002). *MANICE: Manual of Standard Procedures for Observing and Reporting Ice Conditions.* Environment Canada, Ottawa, Canada.

Canadian Meteorological Centre (2003). "Canadian Meteorological Service of Canada", http://weatheroffice.ec.gc.ca/canada_e.html, Accessed August 2, 2003.

Côté, J., S. Gravel, A. Méthot, A. Patoine, M. Roch, and A. Staniforth. (1997a). "The operational CMC/MRB Global Environmental Multiscale (GEM) model: Part I - Design considerations and formulation." Monthly Weather Review, Vol. 126, pp. 1373-1395.

Côté, J., S. Gravel, A. Méthot, A. Patoine, M. Roch, and A. Staniforth. (1997b). "The Operational CMC/MRB Global Environmental Multiscale (GEM) model: Part II – Results." Monthly Weather Review, Vol. 126, pp. 1397-1418.

Desnos, Y. L., C. Buck, J. Guijarro, G. Levrini, J.L. Suchail, R. Torres, H. Laur, J. Closa, B. Rosich (2000). "The ENVISAT Advanced Synthetic Aperture Radar System." International IEEE, Geoscience and Remote Sensing Symposium, IGARSS 2000, Vol. 3, pp. 1171-1173.

El-Diasty, M., and A. El-Rabbany, G. Auda (2002). "Predicting Sea Ice Conditions for Marine Operations in Ice-Covered Waters." Proceedings of the Oceans 2002 MTS/IEEE Conference, Biloxi, Mississippi, USA, October 29-31, pp. 1234-1243. CD-ROM.

El-Diasty, M., and A. El-Rabbany (2003a). "Sequential Sea Ice Concentration Prediction for Marine Operations in Ice-Infested Waters." International Hydrographic Review, Vol. 4, No. 2, pp. 82-87.

El-Diasty, M., and A. El-Rabbany (2003b). "Performance Evaluation of Two Neural Network-Based Models for Predicting Sea Ice Concentration." Proceedings of the 37th CMOS Congress Conference, Ottawa, ON, Canada, June 2-5, Oral PowerPoint Presentation.

El-Rabbany, A. (2000). "Integrated Navigation Chart System." Invited presentation at the "Ice in ECDIS" Workshop, St. John's, Newfoundland, 5-6 June.

El-Rabbany, A., G. Auda, and S. Abdelazim (2002). "Predicting Sea Ice Conditions Using Neural Networks." Journal of Navigation, Vol. 55, pp. 137-143.

El-Rabbany, A. and M. El-Diasty (2003). "A New Approach to Tidal Prediction." Journal of Navigation, Vol. 56, pp. 305-314.

Flato, G. M., and W. D. Hibler. (1992). "Modeling Pack Ice as a Cavitating Fluid." Journal of Physical Oceanography, Vol. 22, pp. 626-650.

Flato, G. M. (1993). "A Particle-In-Cell Sea-ice Model." Atmosphere Ocean Vol. 31, (3), pp. 339-358.

Flato, G. M. (1994). "McPIC: Documentation for the Multi-category Particle-In-Cell Sea Ice Model." Canadian Technical Report of Hydrography and Ocean Sciences, No. 158, Institute of Ocean Sciences, Sidney, BC, 74 pp.

Flett, D. G., M. J. Manore, B. R. Ramsay, J. C. Falkingham (2001). "Preparing for Operational Use of RADARSAT-2 Data at the Canadian Ice Service." International IEEE, Geoscience and Remote Sensing Symposium, IGARSS '01, Vol. 1, pp. 493-495.

Flett, D. G. (2002). "Marine Remote Sensing Applications Development at the Canadian Ice Service." Presentation at Twelfth Annual Meeting of the Participants of the International Arctic Buoy Programme (IABP), Marine Environmental Data Service (MEDS), Ottawa, June10-12.

Global Hydrology Research Center (2003). "Dataset Guide Documents: GHRC Guide Documents", http://microwave.nsstc.nasa.gov/ghrc.html, Accessed August 2, 2003.

Gunter's Space Page (2003). "DMSP-5D3 F15, 16, 17, 18, 19, 20 ", http://www.skyrocket.de/space/doc_sdat/dmsp-5d3.htm, Accessed August 2, 2003.

Haapala, J. (2002). *UNDERSTANDING THE GLOBAL SYSTEM: Numerical investigations of sea-ice variability in the Arctic Ocean.* Finnish Global Change Research Programme FIGARE, Painosalama, Turku.

Hakkinen, S., and G.L. Mellor (1992). "Modeling the Seasonal Variability of a Coupled Arctic Ice-ocean System." Journal of Geophysical Research, Vol. 97, pp. 20,285-20,304.

Haykin, S., E. O. Lewis, R.K. Raney and J.R. Rossiter (1994). *Remote Sensing of Sea Ice and Icebergs*, John Wiley & Sons, Inc.

Haykin, S. (1999). *Neural Networks: A Comprehensive Foundation.* Second Edition. Prentice Hall.

Hibler, W. D. (1979). "A Dynamical Thermodynamic Sea Ice Model." Journal of Physical Oceanography, Vol. 9, pp. 815-846.

Hibler, W. D., and K. Bryan (1984). "Oceanic circulation: Its effect on seasonal sea ice simulations." Science, pp. 489-492.

Jacobs, R. A. (1988). "Increased rates of convergence through learning rate adaptation." Neural Networks, Vol. 1, pp. 295--307.

Jacobs, R. A., M. I. Jordan, S. J. Nowlan, and G.E. Hinton (1991). "Adaptive Mixtures of Local Experts." Neural Computation, Vol. 3, pp. 79-87.

Kamruzzaman, J., and S. M. Aziz (2002). "A Note on Activation Function in Multilayer Feedforward Learning." Neural Networks, IJCNN '02. Proceedings of the 2002 International Joint Conference, 12-17 May, Vol. 1, pp. 519-523.

Mailhot, J., R. Sarrazin, B. Bilodeau, N. Brunet, and G. Pellerin (1997). "Developement of the 35-km version of the operational regional forecast system." Atmosphere-Ocean, Vol. 35, pp. 1-28.

Mancini, P., J. L. Suchail, Y.L. Desnos, R. Torres, J. Guijarro, G. Graf (1996). "The Development of the ENVISAT-1 Advanced Synthetic Aperture Radar." International IEEE, Geoscience and Remote Sensing Symposium 1996, IGARSS '96, 'Remote Sensing for a Sustainable Future.', 27-31 May, Vol. 2 , pp. 1355-1357.

Mauritzen, C., and S. Hakkinen (1997). "Influence of Sea Ice on the Meridional Overturning Cell in the North Atlantic." ACCP Notes, Vol. IV, No. 2, 6-10

Maykut, G. A., and N. Untersteiner (1971). "Some Results from a Time Dependent Thermodynamic Model of Sea Ice." Journal of Geophysical Research Vol. 76, pp. 1550-1575.

Minai, A. A., Williams, R. D. (1990). "Back-propagation heuristics: a study of the extended delta-bar-delta algorithm." Proceedings of 1990 International Joint Conference on Neural Networks, Vol.1, 595 –600.

NASA's Goddard Space Flight Center (2003). "NASA Facts: NOAA-M Continues Polar-Orbiting Operational Environmental Satellite Series." http://www.gsfc.nasa.gov/gsfc/service/gallery/fact_sheets/earthsci/noaam-fs.pdf, Accessed August 2, 2003.

Nazarenko, D. M., D. Martenson, S. Rossignol, G. Staples (1995). "RADARSAT Image Characteristics and Application Requirements." Record of the International IEEE, Radar Conference, 8-11 May, pp.351-355

NeuralWare (2001a). *Neural Computing: A Technology Handbook for NeuralWorks Professional II/PLUS.* PA, USA.

NeuralWare (2001b). *NeuralWorks Professional II/Plus Reference Guide.* PA, USA.

NOAA Satellites and Information (2003a). "Polar Operational Environmental Satellite", http://www.oso.noaa.gov/poes/, Accessed August 2, 2003.

NOAA Satellites and Information (2003b). "Defense Meteorological Satellite Program", http://dmsp.ngdc.noaa.gov/dmsp.html, Accessed August 2, 2003.

Parashar, S. (1994). "RADARSAT program" International IEEE, Geoscience and Remote Sensing Symposium, IGARSS '94, 'Surface and Atmospheric Remote Sensing: Technologies, Data Analysis and Interpretation', 8-12 Aug, Vol.3, pp.1709 - 1713

Parkinson, C. L., and W. M. Washington (1979). "A Large-scale Numerical Model of Sea Ice." Journal of Geophysical Research, Vol. 84, pp. 311-337.

Ramsay, B. (2000). "Canadian Ice Service." Presentation at the "Ice in ECDIS" Workshop, St. John's, Newfoundland, 5-6 June.

Ramsay, B., M. Manore, L. Weir, K. Wilson and D. Bradley (1998). "Utilization of RADARSAT Data in the Canadian Ice Service." Application Development and Research Opportunity (ADRO) Symposium, Montreal, October.

Ramsay, B., D. Flett, M. Manore, R. De Abreu (2001). " Radarsat-1 for Sea Ice Monitoring in Canada-an Operational Success Story." International IEEE, Geoscience and Remote Sensing Symposium, IGARSS '01, Vol. 1, pp. 477 – 479.

Randell, C., M. Rokonuzzaman, J. Youden and R. Khan (1998). "Evaluation of RADARSAT for Detection, Classification and Discrimination of Icebergs." Application Development and Research Opportunity (ADRO) Symposium, Montreal, October.

Rumelhart, D. E., G. E. Hinton, and R. J. Williams. (1986). "Learning Representations by Back-Propagating errors." Nature Vol. 323, pp. 533-536.

Saucier, F. J., F. Roy, D. Gilbert, P. Pellerin and H. Ritchie (2000). "The Formation and Circulation Processes of Water Masses and Sea Ice in the Gulf of St. Lawrence." Submmited to Journal of Geophysical Research.

Schuh, H., M. Ulrich, D. Egger, J. Muller, W. Schwegmann (2002). "Prediction of Earth Orientation Parameters by Artificial Neural Networks." Journal of Geodesy, Vol. 76, pp. 247-258.

Semtner, A. J. Jr. (1976a). "A Model for the Thermodynamic Growth of Sea Ice in Numerical Investigations of Climate." Journal of Physical Oceanography, Vol. 6, pp. 379-389.

Semtner, A. J. Jr. (1976b). "Numerical Simulation of the Arctic Ocean Circulation." Journal of Physical Oceanography, Vol. 6, pp. 379-389.

Semtner, A. J. Jr. (1987). "A Numerical Study of Sea Ice and Ocean Circulation in the Arctic." Journal of Physical Oceanography, Vol. 11, pp. 309-323.

Sidani, A. and T. Sidani (1994). "A Comprehensive Study of the Backpropagation Algorithm and Modifications." Southcon/94. Conference, March 29-31, pp. 80-84.

Stronach, J. A., J. O. Backhaus, and T. S. Murty. (1993). "An Update on the Numerical Simulation of Oceanographic Processes in the Waters Between Vancouver Island and the Mainland: the GF8 model." Oceanography and Marine Biology, An Annual Review, Vol. 31, pp. 1-86.

Yao, T., C. L. Tang, and I. K. Peterson (2000). "Modeling the Seasonal Variation of Sea Ice in the Labrador Sea with a Coupled Multicategory is Model and the Princeton Ocean Model." Journal of Geophysical Research, Vol. 105, pp. 1153-1165.

Zhang, Z. (2000). "On Modelling Ice Dynamics of Semi-Enclosed Seasonally Ice-Covered Seas." Academic Dissertation, University of Helsinki, Department of Geophysics, Faculty of Science, Report Series in Geophysics, No.43.

APPENDIX I: COUPLED ICE-OCEAN PARAMETERS

Parameters	Values
1) Sea water density	$\rho_0 = 10^3 kg\ m^{-3}$
2) Air density	$\rho_A = 1.22\ kg\ m^{-3}$
3) Ice density	$\rho_I = 0.92 \times 10^3\ kg\ m^{-3}$
4) Bottom drag coefficient	$C_b = 2 \times 10^3$
5) Air-ocean drag coefficient	$C_{DAO} = 2.6 \times 10^{-3}$, when $0 < \lvert U_A \rvert < 11\ m\ s^{-1}$
6) Air-ocean drag coefficient	$C_{DAO} = (1.89 + 0.065) \times 10^{-3} \lvert U_A \rvert$, when $\lvert U_A \rvert \geq 11\ m\ s^{-1}$
7) Ice-ocean drag coefficient	$C_{DIO} = 1.52 \times 10^{-3}$
8) Air-ice drag coefficient	$C_{DAI} = C_{DAO}$
9) Specific heat of sea water	$C_{PO} = 3.99 \times 10^3\ J\ kg^{-1}\ K^{-1}$
10) Specific heat of air	$C_{PA} = 1.008 \times 10^3\ J\ kg^{-1}\ K^{-1}$
11) Air-ocean sensible heat transfer	$C_{SAO} = 3.5 \times 10^{-3}$, when $T_O > T_A$
12) Air-ocean sensible heat transfer	$C_{SAO} = 0.66 \times 10^{-3}$, when $T_A \geq T_O$,
13) Air-ice sensible heat coefficient	$C_{SAI} = 3.9 \times 10^{-3}$
14) Ice-ocean sensible heat coefficient	$C_{SIO} = 4 \times 10^{-3}$
15) Air-ocean latent heat transfer coefficient	$C_{LAO} = 1.15 \times 10^{-3}$
16) Air-ice latent heat transfer coefficient	$C_{LAI} = C_{LAO}$
17) Solar constant	$S_c^0 = 1353\ W\ m^{-2}$
18) Stefan Boltzmann,s constant	$\sigma_{SB} = 5.68 \times 10^{-8}\ W\ m^{-2}\ K^{-4}$

19) Emissivity of sea water, ice, and snow	$\varepsilon_O = \varepsilon_I = \varepsilon_S = 0.97$
20) Ice salinity	$S_I = 4$
21) Background viscosity coefficient	$K_{VM0} = 10^{-4}\ m^2 s^{-1}$
22) Background diffusion coefficient	$K_{V\sigma 0} = 10^{-6}\ m^2 s^{-1}$
23) Von Karman constant	$k = 0.4$
24) Gravitational acceleration	$g = 9.8\ ms^{-2}$
25) Albedo of ice	$\alpha_I = 0.64$
26) Albedo of sea water	$\alpha_O = 0.10$
27) Albedo of Snow	$\alpha_S = 0.75$
28) Latent heat of vaporization of sea water	$L_V = 2.501 \times 10^6\ J\ kg^{-1}$
29) Latent heat of fusion of the sea water	$L_F = 3.347 \times 10^5 J\ kg^{-1}$
30) Latent heat of ice/snow sublimation	$L_S = 2.834 \times 10^6\ J\ kg^{-1}$
31) Snow thermal conductivity	$K_s = 0.31 W\ m^{-1} K^{-1}$
32) Ice thermal conductivity	$K_I = 2.17\ W\ m^{-1} K^{-1}$

APPENDIX II: SUPPLEMENTRY RESULTS

1. Results of Region-C.2.

Results of sequential model for the Region-C.2.

Sympols	Region-C.2 (25 points)	
	FFNN	MNN
N (Total set)	599	599
N_S (Testing set)	50	50
N_T (Training set)	499	499
N_V (Validation set)	50	50
Strucure	[100-150-25]	[100-150-5-25]
RMS (Testing)	0.1691	0.1261
RMS (Training)	0.14055	0.0856
RMS (Validation)	0.2219	0.2040
CORR (Testing)	0.9614	0.977
CORR (Training)	0.9750	0.9900
CORR (Validation)	0.929	0.9373

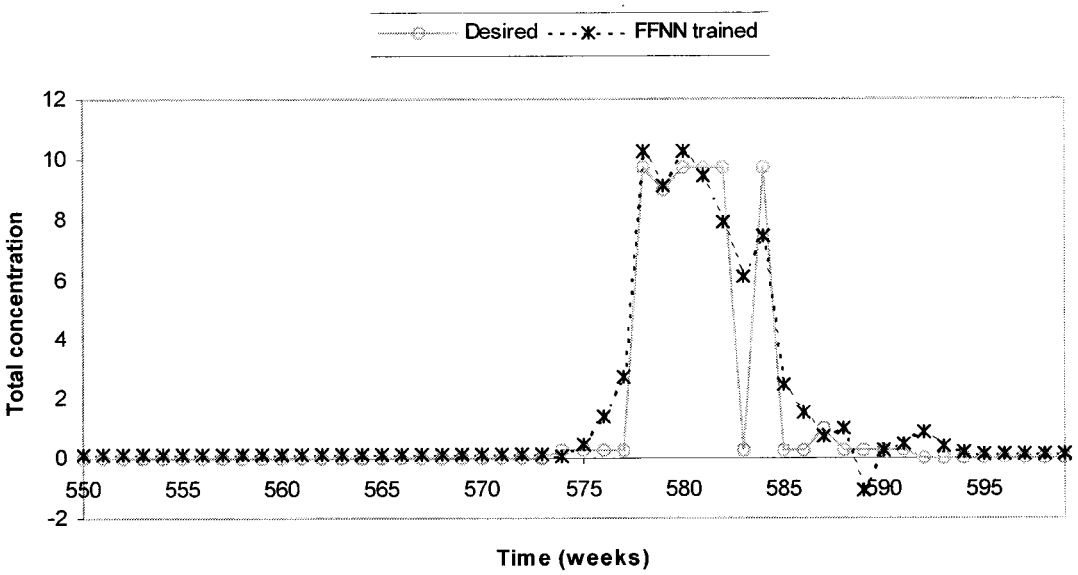

Actual versus predicted ice concentration values from FFNN sequential model for the year 1998 (regional modeling of Region-C.2).

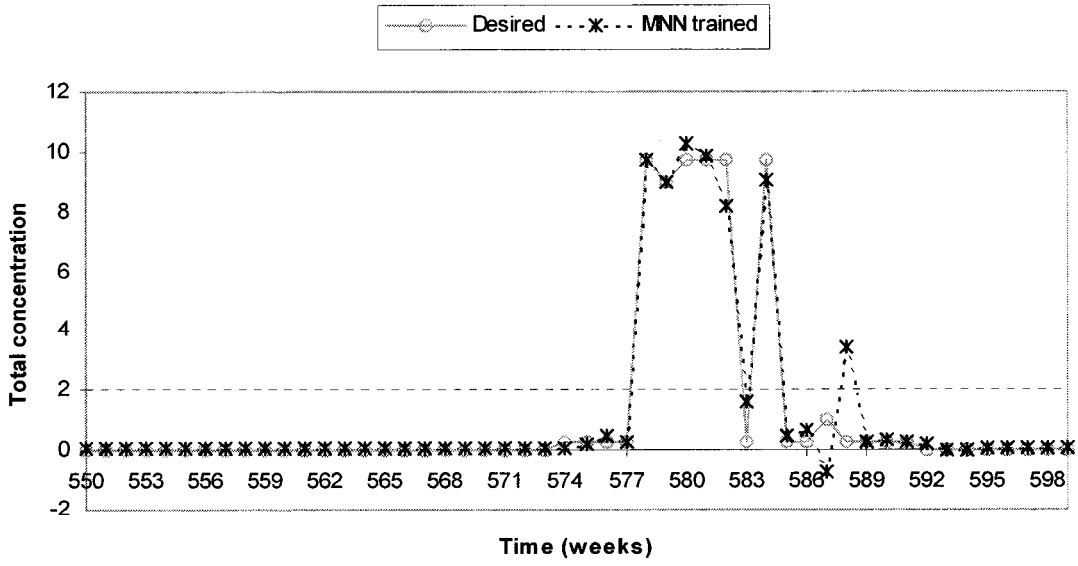

Actual versus predicted ice concentration values from MNN sequential model for the year 1998 (regional modeling of Region-C.2).

2. Results of Region-C.3.

Results of sequential model for the Region-C.3.

Sympols	Region-C.3 (35 points)	
	FFNN	MNN
N (Total set)	599	599
N_S (Testing set)	50	50
N_T (Training set)	499	499
N_V (Validation set)	50	50
Strucure	[140-210-35]	[140-280-5-35]
RMS (Testing)	0.1392	0.1084
RMS (Training)	0.1102	0.0810
RMS (Validation)	0.2040	0.1947
CORR (Testing)	0.973	0.986
CORR (Training)	0.980	0.989
CORR (Validation)	0.9353	0.943

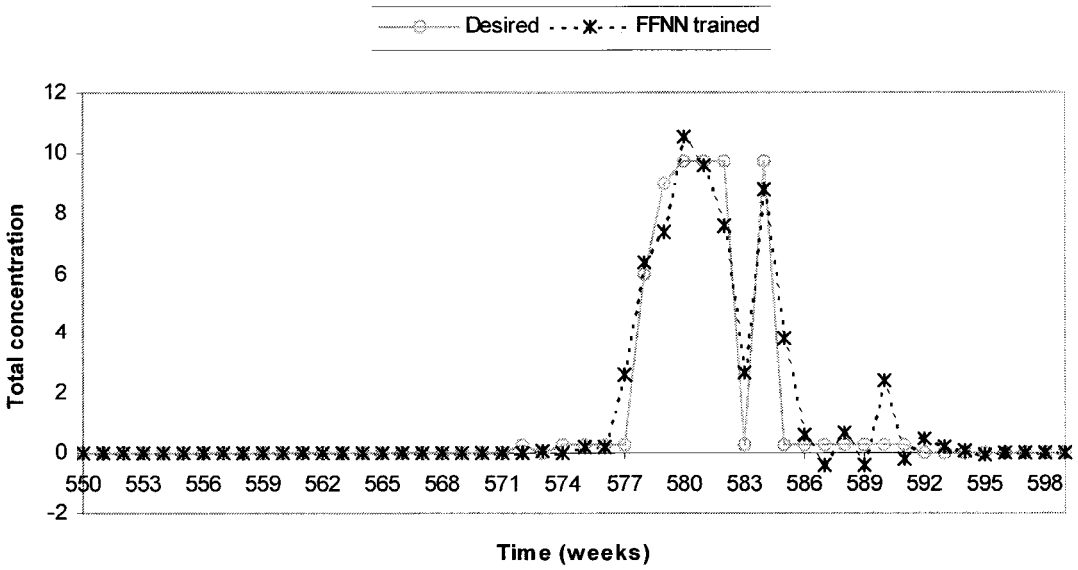

Actual versus predicted ice concentration values from FFNN sequential model for the year 1998 (regional modeling of Region-C.3).

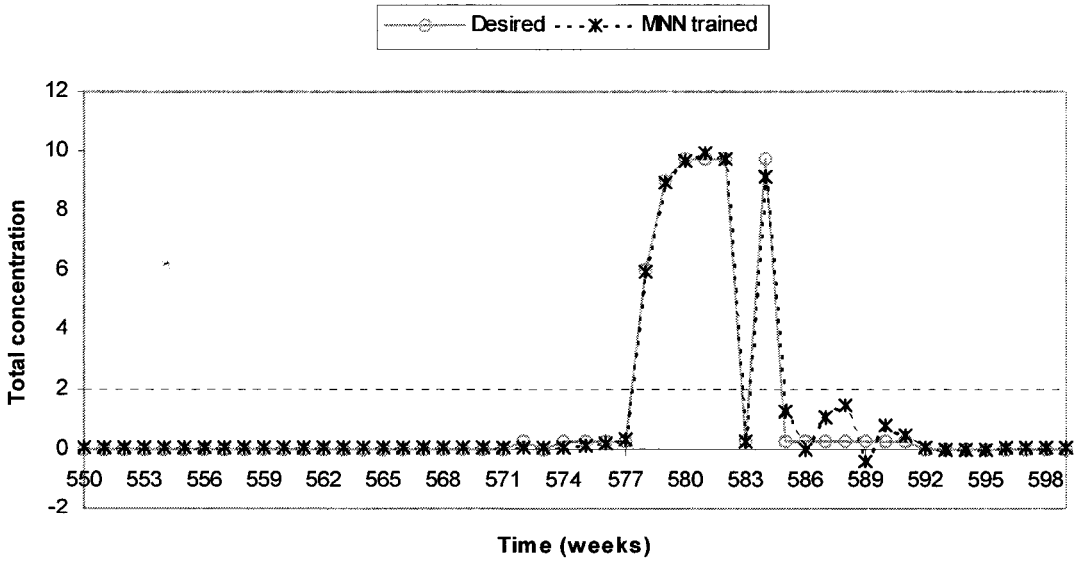

Actual versus predicted ice concentration values from MNN sequential model for the year 1998 (regional modeling of Region-C.3).

3. Results of Region-C.4.

Results of sequential model for the Region-C.4.

Sympols	Region-C.4 (30 points)	
	FFNN	MNN
N (Total set)	599	599
N_S (Testing set)	50	50
N_T (Training set)	499	499
N_V (Validation set)	50	50
Strucure	[120-120-30]	[120-120-5-30]
RMS (Testing)	0.1635	0.157
RMS (Training)	0.1146	0.071
RMS (Validation)	0.2814	0.235
CORR (Testing)	0.964	0.970
CORR (Training)	0.981	0.992
CORR (Validation)	0.882	0.924

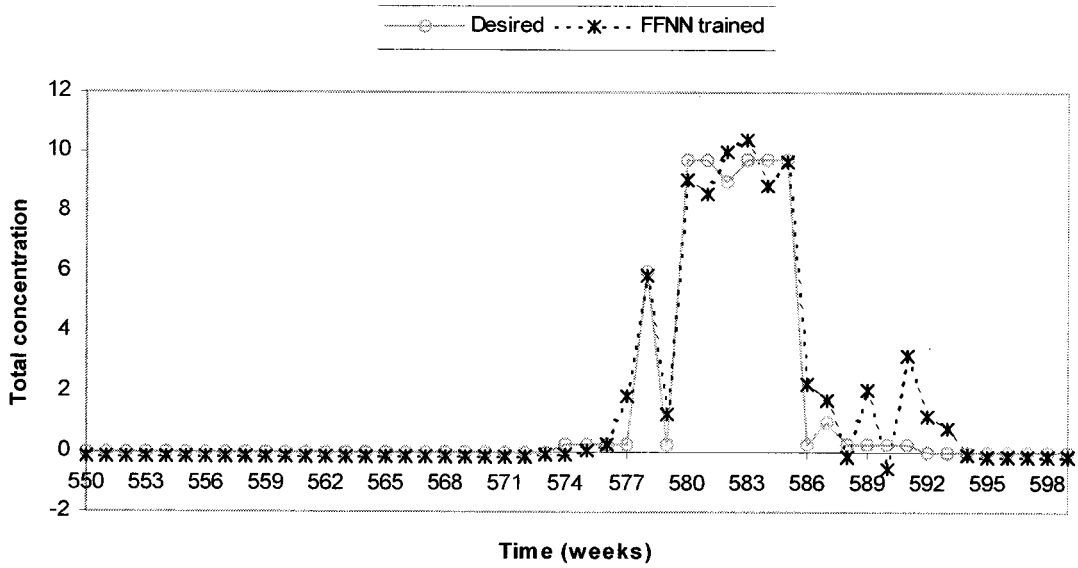

Actual versus predicted ice concentration values from FFNN sequential model for the year 1998 (regional modeling of Region-C.4).

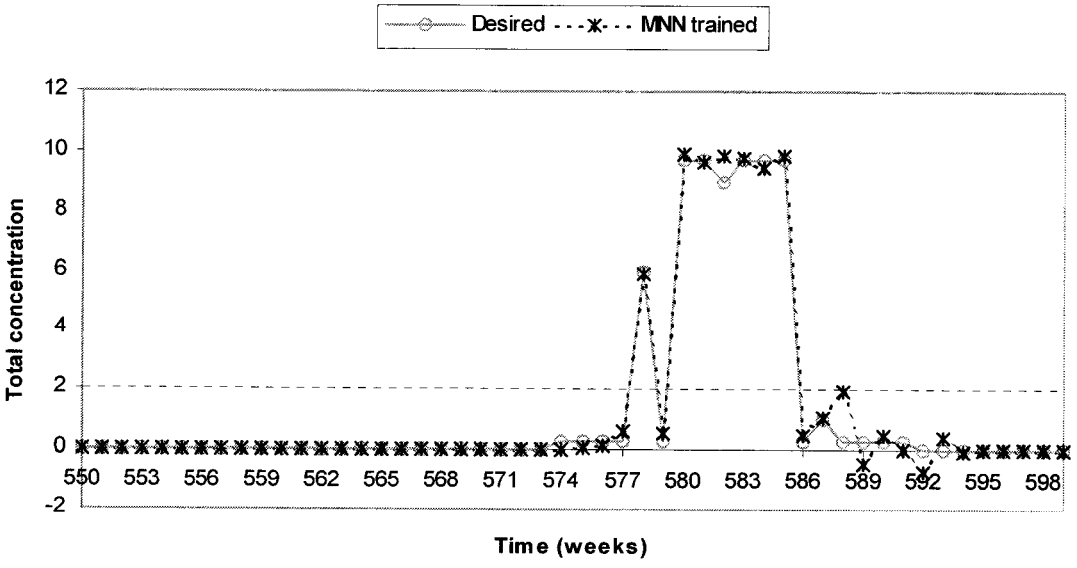

Actual versus predicted ice concentration values from MNN sequential model for the year 1998 (regional modeling of Region-C.2).

4. Results of Region-C.5.

Results of sequential model for the Region-C.5.

Sympols	Region-C.5 (30 points)	
	FFNN	MNN
N (Total set)	599	599
N_S (Testing set)	50	50
N_T (Training set)	499	499
N_V (Validation set)	50	50
Strucure	[120-270-30]	[120-270-5-30]
RMS (Testing)	0.193	0.1563
RMS (Training)	0.160	0.1222
RMS (Validation)	0.267	0.2679
CORR (Testing)	0.947	0.955
CORR (Training)	0.963	0.978
CORR (Validation)	0.878	0.878

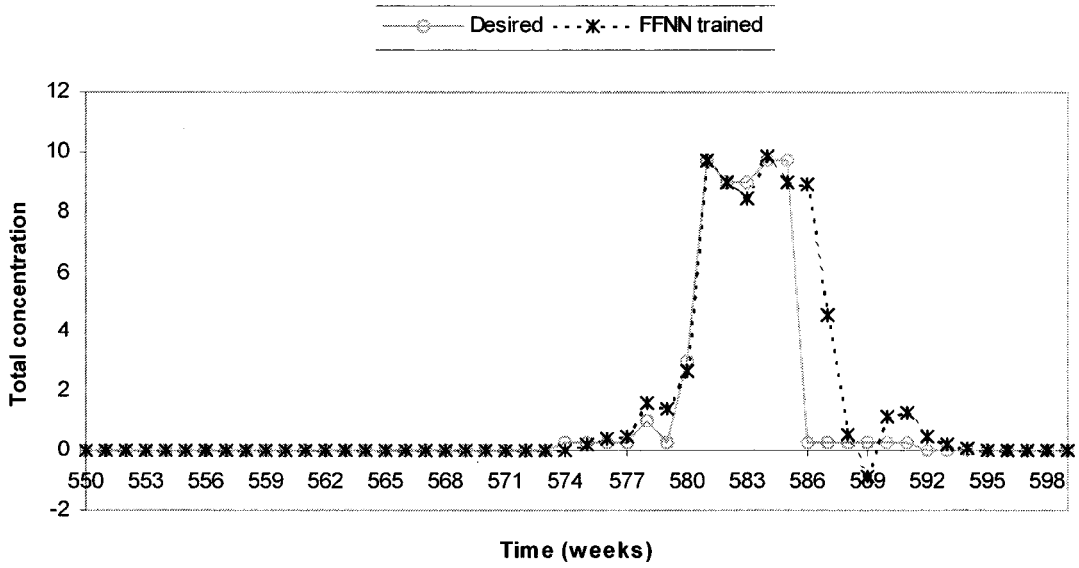

Actual versus predicted ice concentration values from FFNN sequential model for the year 1998 (regional modeling of Region-C.5).

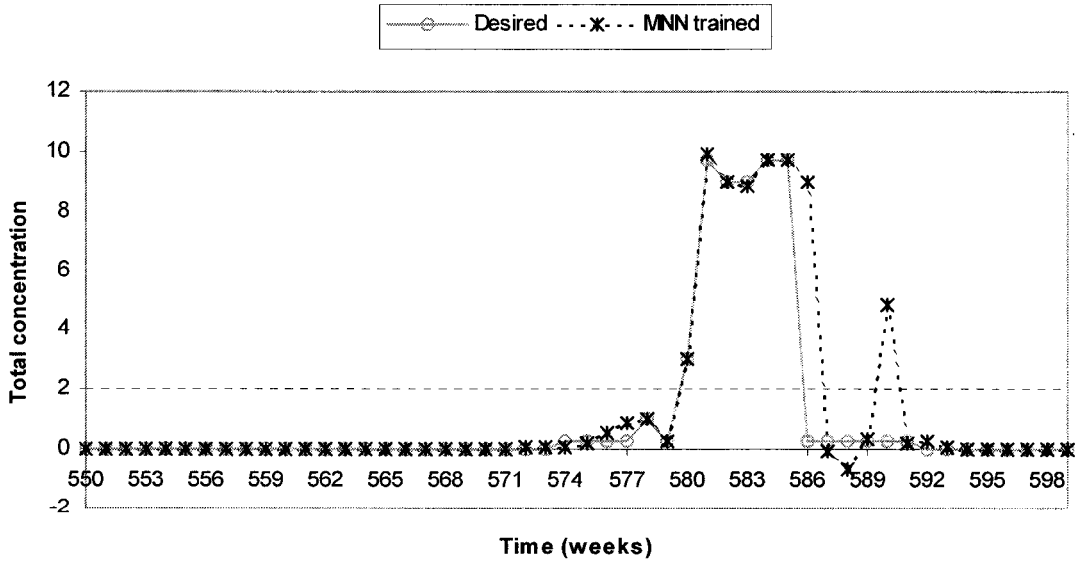

Actual versus predicted ice concentration values from MNN sequential model for the year 1998 (regional modeling of Region-C.5).

5. Results of Region-C.6.

FFNN results of sequential mode for the Region-C.6.

Sympols	Region-C.6 (25 points)	
	FFNN	MNN
N (Total set)	599	599
N_S (Testing set)	50	50
N_T (Training set)	499	499
N_V (Validation set)	50	50
Strucure	[100-150-25]	[100-100-5-25]
RMS (Testing)	0.157	0.0958
RMS (Training)	0.139	0.089
RMS (Validation)	0.237	0.219
CORR (Testing)	0.957	0.985
CORR (Training)	0.972	0.987
CORR (Validation)	0.864	0.885

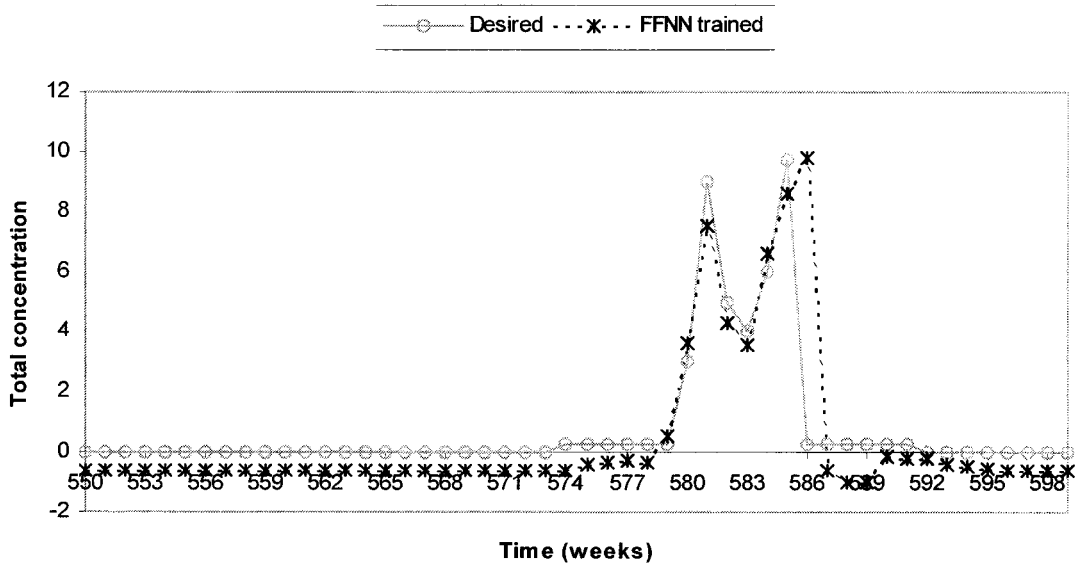

Actual versus predicted ice concentration values from FFNN sequential model for the year 1998 (regional modeling of Region-C.6).

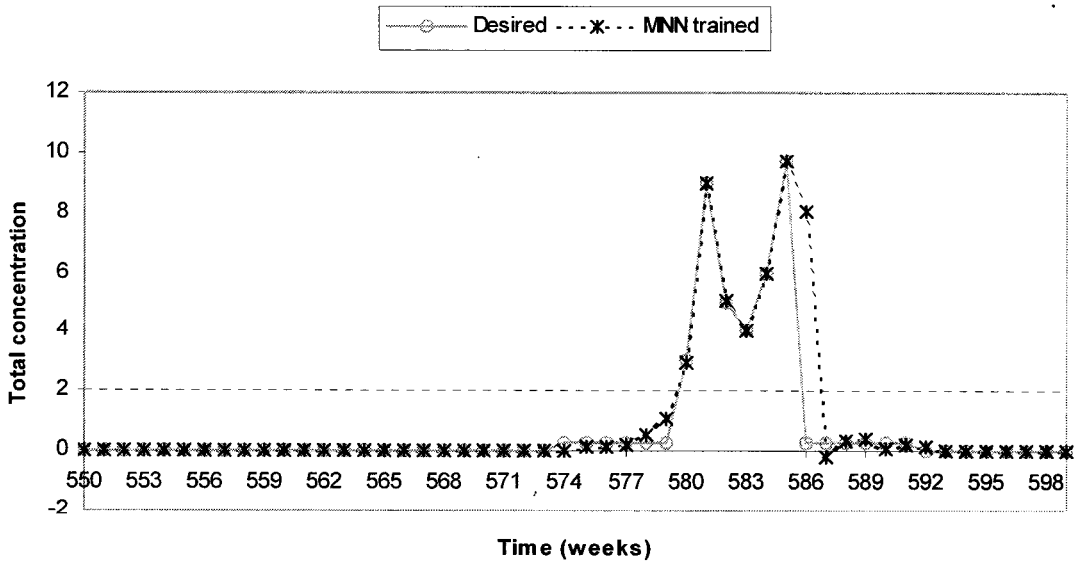

Actual versus predicted ice concentration values from MNN sequential model for the year 1998 (regional modeling of Region-C.6).

6. Results of Region-C.7.

Results of sequential model for the Region-C.7.

Sympols	Region-C.7 (25 points)	
	FFNN	MNN
N (Total set)	599	599
N_S (Testing set)	50	50
N_T (Training set)	499	499
N_V (Validation set)	50	50
Strucure	[100-150-25]	[100-100-5-25]
RMS (Testing)	0.0908	0.063
RMS (Training)	0.1069	0.082
RMS (Validation)	0.2081	0.205
CORR (Testing)	0.981	0.993
CORR (Training)	0.976	0.985
CORR (Validation)	0.7730	0.786

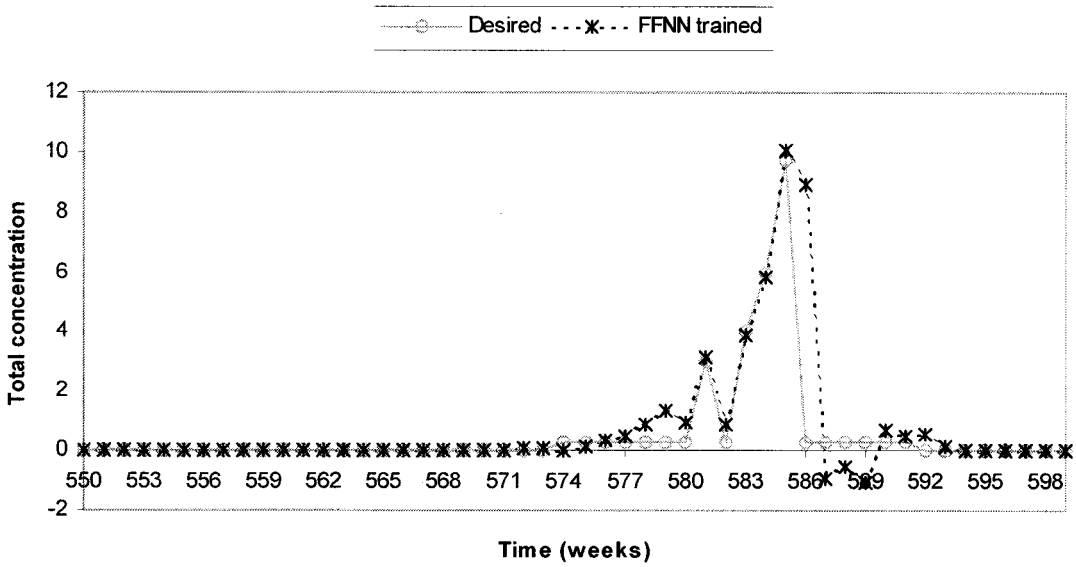

Actual versus predicted ice concentration values from FFNN sequential model for the year 1998 (regional modeling of Region-C.7).

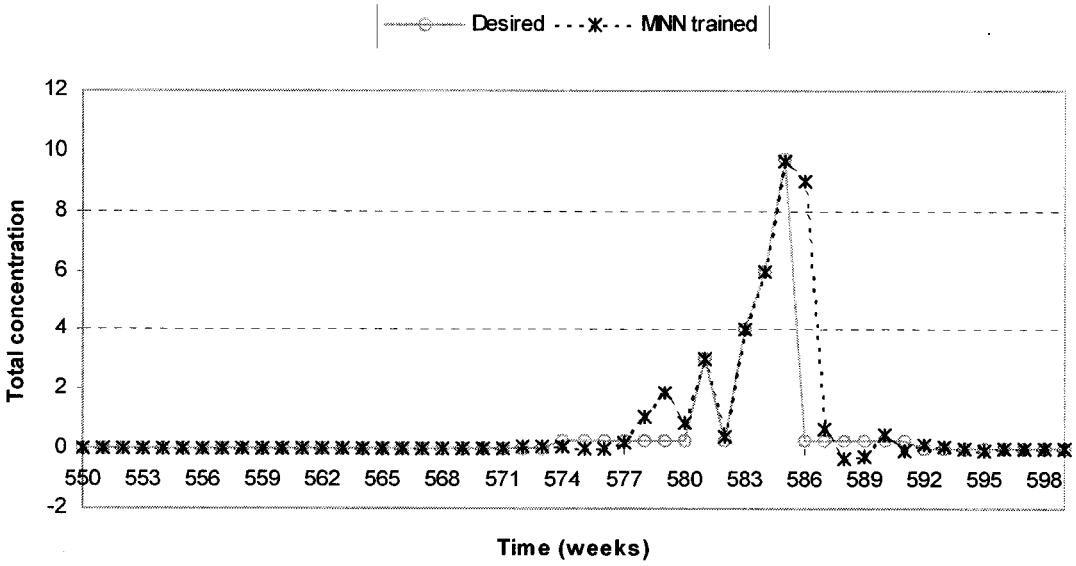

Actual versus predicted ice concentration values from MNN sequential model for the year 1998 (regional modeling of Region-C.7.

VITA

Mohammed K. El-Diasty was born in Egypt, on January 05, 1974. After graduating from Mansoura University, Egypt, in June 1997 with a Bachelor of Engineering in Civil Engineering, he is worked as a lecturer assistant at the Civil Engineering Department at Mansoura University, Egypt from July 1999. In January 2002, he enrolled as a MASc. student in the Department of Civil Engineering at Ryerson University, Canada. Upon receiving his master degree, he will continuously work as a lecturer assistant at the Civil Engineering Department at Mansoura University, Egypt.

Publications

El-Diasty, M., and A. El-Rabbany (2003). "Sequential Sea Ice Concentration Prediction for Marine Operations in Ice-Infested Waters." *International Hydrographic Review*, Vol. 4, No. 2, pp. 82-87.

El-Rabbany, A. and **M. El-Diasty** (2003). "A New Approach to Sequential Tidal Prediction." *The Journal of Navigation*, Vol. 56, No. 2, pp. 305-314.

El-Rabbany, A. and **M. El-Diasty** (2003). "Assessment of Three De-noising Models for MEMS-Based Inertial Sensors." Paper accepted for oral presentation at the 11th IAIN World Congress, Berlin, Germany, 21-24 October.

El-Diasty, M. and A. El-Rabbany, (2003). "Adaptive De-noising Model for MEMS-Based Inertial Data." Proceedings of the Canadian Aeronautics and Space Institute 14th Symposium on Navigation, Montréal, Québec, Canada, 28-30 April. CD-ROM.

El-Diasty, M. and A. El-Rabbany (2003). "Sequential Tidal Prediction Using Artificial Neural Networks." Proceedings of the U.S. Hydro 2003 Conference, Biloxi, Mississippi, USA, 24-27 March. CD-ROM.

El-Diasty, M. and A. El-Rabbany (2003). "Adaptive Noise Reduction Model for MEMS-Based Inertial Sensors." Proceedings of the Institute of Navigation National Technical Meeting, ION NTM 2003, Anaheim, California, USA, 22-24 January. CD-ROM.

El-Diasty, M., A. El-Rabbany, G. Auda (2002). "Predicting Sea Ice Conditions for Marine Operations in Ice-Covered Waters." Proceedings of the Oceans 2002 MTS/IEEE Conference, Biloxi, Mississippi, USA, October 29-31, pp. 1234-1243. CD-ROM.

El-Diasty, M. and A. El-Rabbany (2003). "Performance Evaluation of Two Neural Network-Based Models for Predicting Sea Ice Concentration." Presented at the CMOS Congress 2003, Ottawa, Ontario, Canada, 2-5 June.

El-Diasty, M. and A. El-Rabbany (2002). "An Integrated Navigational Chart System for Ice Navigation: New Developments." Poster presented at the annual CRESTech workshop, Toronto, Ontario, Canada, 1 October.